Laser Induced Plasma in Liquid/Solid-Liquid Interface and Implication on Nucleation of Nanoparticles

by
ARPITA NATH

DEPARTMENT OF PHYSICS
INDIAN INSTITUTE OF TECHNOLOGY GUWAHATI
GUWAHATI-781039, INDIA
JULY 2011

Laser Induced Plasma in Liquid/Solid-Liquid Interface and Implication on Nucleation of Nanoparticles

A Thesis Submitted in Partial Fulfillment of the Requirements for the

Award of the Degree

of

DOCTOR OF PHILOSOPHY

by
ARPITA NATH

DEPARTMENT OF PHYSICS
INDIAN INSTITUTE OF TECHNOLOGY GUWAHATI
GUWAHATI-781039, INDIA
JULY 2011

উসর্গ আমার বাবা এবং মা জন্য !

Dedicated to My Parents!

Arpita Nath
Registration No. 06612108
Department of Physics
Indian Institute of Technology Guwahati
Guwahati 781039, India

STATEMENT

I hereby declare that the research work presented in this thesis is carried out by me under the supervision of Prof. Alika Khare, Department of Physics, Indian Institute of Technology Guwahati. The thesis is submitted in partial fulfillment of the requirements for the award of degree of Doctor of Philosophy to the Department of Physics, Indian Institute of Technology Guwahati, India. This thesis has not been submitted to any other institute, university or elsewhere for the award of degree.

Date: **ARPITA NATH**

भारतीय प्रौद्योगिकी संस्थान गुवाहाटी
Indian Institute of Technology Guwahati
Department of Physics
Guwahati-781039, Assam State, INDIA
Phone: +91 361 2582705, 2582701, 2690321 to 328 (extn. 2705),
Fax: +91 361 2582749
Dr. Alika Khare
Professor
E-mail: alika@iitg.ernet.in, k_alika@yahoo.com

Date:

Certificate

This is to certify that work contained in the thesis entitled '**Laser induced plasma in liquid/solid-liquid interface and implication on nucleation of nanoparticles**' by **Ms Arpita Nath** (Roll no. 06612108), a student of Department of Physics, Indian Institute of Technology Guwahati, for the award of degree of Doctor of Philosophy, has been carried out under my supervision and that the same has not been submitted elsewhere for a degree.

(Alika Khare)

ACKNOWLEDGEMENT

I would like to express my deep and sincere gratitude to my supervisor, Prof. Alika Khare for giving me the opportunity to pursue my research work under her supervision. Her optimism, persistent support and encouragement assisted me in overcoming the barriers encountered at different stages of research work in the past five years. Under her guidance, I appreciate the unconditional liberation to cultivate our own ideas for implementation and advancement of the thesis work plan.

I am highly benefitted from the timely and invaluable suggestions, critical assessments offered by my doctoral committee members; Dr. M K Nandy, Dr. A K Sharma, Dr. A Singh and Dr. S. K. Joshi. I am indebted to Dr. L Rangan and her student Archana of Department of Biotechnology, Indian Institute of Technology Guwahati for providing the facilities to carry out the antibacterial studies. I am thankful to Dr. G Krishnamoorty and her student Anusaya for providing the freedom of using the Fluorescence Set-up in Central Instruments Facility. I am thankful to Dr.P Agarwal for lending the UV source lamp to carry out the photocatalytic studies.

I offer my gratitude to the HOD and all the other faculty members of the Department of Physics, Indian Institute of Technology Guwahati for their direct or indirect support which has a significant contribution in the completion of my thesis. My special thanks to the staff of Department of Physics, Dr. Sidananda Sarma, Mr. Basab Purkhastya, Mr. Atul Chandra Deka , Mr. Lokesh Chakraborty and Mr. Bimal Kumar Sarma for their support and timely assistance.

I am gratified to the Central Instruments Facility and especially to Mr. Chandan Burgohain, Mr. Madhurjay Borah and Mr. Kula Senapati for helping me with the TEM, SEM, UV-Vis and Laser Raman measurements. My special thanks to

Mr. Chandan Burgohain for acquainting me with the minutest details related to TEM sample preparation, operation of Oven, Ultra Sonicator and Centrifuge Machine etc.

I am highly indebted to Gaurav Shukla as he kindly acquainted me in dealing with all the equipments available in the lab. My special thanks to Dr. Archana and my loving juniors in the lab, Abu, Satchi, Indrajeet and Partha, for their unconditional support and obligingness.

My batch mates Biswanath Samantaray, Biswanath Dutta and Aneesh are fabulous. My special thanks to Sunita for bearing me for the past 4 years with my nonstop outburst of frustration, disappointment and excitement. I am thankful to my hostel mates Prangya, Rojalin and Archana for making my stay in Hostel Subansiri enjoyable.

Last but not the least my special thanks to my Baba, Ma, Guddi and Tushar for their love, support, encouragement and critical opinion to keep me on track for all these years.

ABSTRACT

The present work focuses on transient evolution of pulsed laser induced breakdown process in liquid and solid-liquid interface. The focusing of high power laser inside a liquid media leads to plasma formation and shockwave emission. When the same process takes place at a solid-liquid interface, the plasma from the solid target interacts with the surrounding liquid and under suitable condition results into formation of nanoparticulates. On a larger time scale, plasma is replaced by cavitation vapor bubbles which expands and collapses in order to maintain the pressure gradient with the surrounding liquid. In the present work, the complete dynamics of laser induced breakdown in water and metal-water interface is studied. For this various diagnostics; beam deflection set-up, shadowgraphic technique, electric probes and plasma spectroscopy were devloped. Beam deflection was employed to study the spatial and temporal evolution of shockwave velocity and cavitation bubble dynamics at the breakdown region. The shockwave velocity and cavitation bubble expansion velocity at the breakdown region were found to be in the range of 10^4 m/s and 10^2 m/s respectively. The multiple bubble hydrodynamics was studied via shadowgraphic technique to unleash the bubble evolution and bubble-bubble interaction. The electric probe was used to record the transient conduction and corresponding thermal diffusivity of laser produced water plasma. The plasma spectroscopy was performed to detect the Hydrogen bonded OH, O_2 and HO_2* produced during laser induced breakdown of water.

Laser induced breakdown at metal-water interface is used to synthesize Titanium oxide and Copper oxide nanoparticles and the effects of plasma dynamics onto the synthesized nanoparticulates are implicated. The laser focusing conditions during the

breakdown is altered to tailor the size and structural properties of the nanoparticles. The measurement of pressure and temperature using beam deflection set-up and plasma spectroscopy during laser induced breakdown at solid-liquid interface is used to estimate the nucleation time, growth velocity and size of nanoparticles and compared with experimentally observed size of nanoparticles. The nanoparticles are characterized using TEM, Raman, UV-Vis and Photo Luminescence spectra. The applicability of the synthesized titanium oxide nanoparticles as photocatalyst and copper oxide nanoparticles as antibacterial agent are also reported.

Table of Contents

List of Figures

List of Tables

Abbreviations

LIB	Laser Induced Breakdown
HPHT	High Pressure High Temperature
PLA	Pulsed Laser Ablation
BDS	Beam Deflection Set-up
SG	ShadowGraphy
EEP	External Electric Probe
LIBS	Laser Induced Breakdown Spectroscopy

Symbols

I	Intensity
k	No. of Photons
ns	Nanosecond
fs	Femtosecond
$\bar{u}$	Vector velocity
φ	Velocity potential
p	Pressure
ρ	Density of water
c_∞	Sonic velocity
h_b	Enthalpy
u	Velocity
R	Bubble radius
C	Sonic velocity
U	Bubble wall velocity
H	Enthalpy at bubble wall
R_{max}	Maximum bubble radius
p_v	Vapor pressure of water
T_c	Time of collapse
P_0	Hydrostatic pressure
Q	Pressure inside the bubble at maximum radius R_{max}
P_m	Ambient pressure
$\dot{R}$	Bubble wall velocity (U)

$\ddot{R}$	Bubble wall acceleration
γ	Ratio of specific heat
R_{min}	Minimum Bubble Radius
P_{max}	Maximum gas pressure inside bubble
n_e	Electron density
T	Temperature
I_{dif}	Diffusion current
χ	Thermal diffusivity
P_s	Shockwave pressure
U_s	Shockwave velocity
u_p	Particle velocity
I_{OH}	Diatomic molecular spectrum intensity of OH band
w	Wavenumber
A_s	Oscillator strength
k_B	Boltzmann constant
T_{rot}	Rotational Temperature
E_r	Rotational Energy
J'	Lower state
J''	Upper state
h	Planck's constant
B_v	Rotational Constant
c_s	Speed of light
I_{O2}	Diatomic molecular spectrum intensity of O_2 band

S	Höln-London factors
λ	wavelength
ΔG	Total free energy
Δg	volumetric driving force
γ_s	energy due to surface tension
n^{nuc}	no. of molecules in nucleus
Ω	Volume of each molecule
ΔG^{nuc}	Total free energy of a nucleus containing n^{nuc} molecules
r*	Size of critical nucleus
τ	Nucleation time
Z	Zeldovich factor
β*	Rate of molecules added to nucleus
$p_{sat}(T)$	Saturated vapor pressure titanium plasma
m	Mass of TiO_2
V_m	Molar volume of TiO_2
N_A	Avogadro's no.
ΔV	Molar volume difference
Δμ	Chemical potential difference
d	Size of nanoparticles
V	Growth velocity
τ_d	Laser pulse duration
J_{LN}	number of clusters entering the nucleus per unit time
J_{NL}	number of clusters entering the liquid per unit time

E_a	Activation energy
$\Delta\Phi$	Free energy difference
ς	Lattice constant
υ_{vib}	Thermal vibration frequency

Chapter1

1. Introduction

The advent of high power lasers unleashed a new era of laser-induced material processing in solid, liquid and gaseous medium[1-3]. The pioneer work in laser-solid interaction was carried out by Smith and Turner in 1965 who prepared the vacuum deposited thin films using a Ruby laser [4]. The study on laser induced breakdown (LIB) in liquids was instigated immediately afterwards by Bell et al. and Barnes et al. [5, 6]. However it took two decades to uncover the prospects of laser ablation at target-liquid interface [7]. The LIB at liquid/solid-liquid interface leads to transient plasma alongwith exuberant mechanical effects in the form of shockwaves and cavitation bubbles. The basic difference between laser ablation of solids in vacuum or gases and at solid liquid interface is the plasma confinement by the surrounding liquids which generates a localized region of high pressure of the order of GPa [8]. This situation mesmerizes the thermodynamic and kinetic aspects of plasma and, under suitable condition, leads to the formation of various nanocrystals [9].

1.1 Laser Induced Breakdown in Liquids

High power laser irradiation inside a liquid medium leads to plasma formation. The basic mechanism of laser–induced plasma is highly complex and non-linear. Figure 1.1 depicts the various processes occurring in laser induced breakdown in liquid. The irradiation I ($I \geq 10^7$ W/cm^2) by a high power ns laser inside the liquid medium generates the starting seed electrons via multiphoton ionization, figure 1.2 [10]. For impure media, free electrons also arise from the easily ionizable impurities which act

as shallow donors [10]. The seed electrons in this case are generated via local heating or absorption of one or two photons which also contributes in lowering the threshold breakdown.

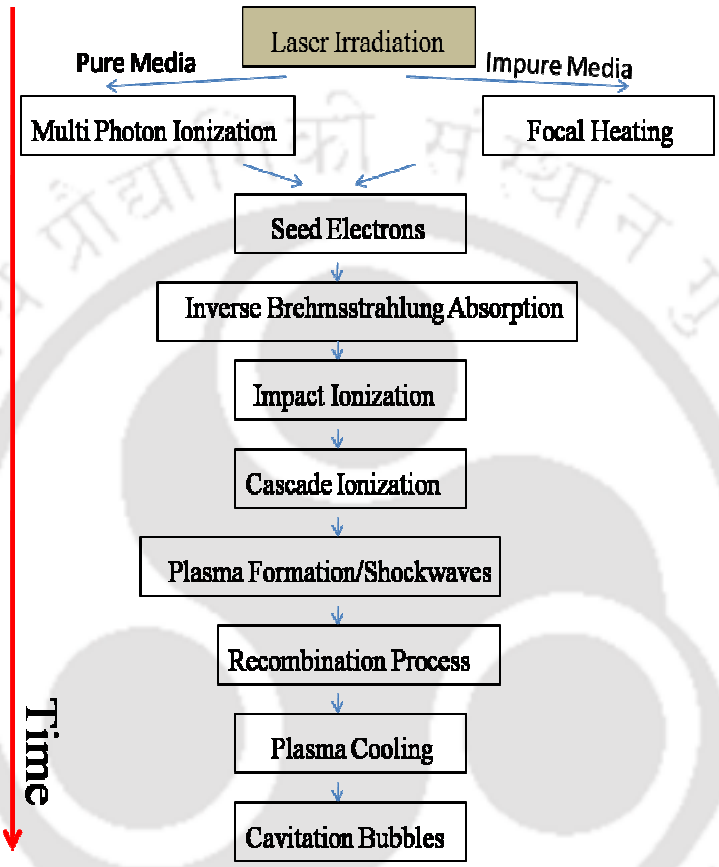

Figure 1.1 *The transient evolution of physical processes in laser induced breakdown in liquids*

Once a free electron is created, it absorbs a photon via inverse bremmstrahlung during collision with heavier species. With each collision it gains kinetic energy. After bremmstrahlung absorption of several photons, the electron achieves sufficient kinetic energy to create another free electron via impact ionization. This eventually results into avalanche ionization which causes rapid excitation and ionization of the liquid medium in the focal volume leading to plasma formation. For ultrashort pulses (< 40

fs) growth of free electrons occurs mainly via multiphoton ionization . In case of ns laser pulses, multiphoton ionization (which varies as $\propto I^k$, I is the intensity, k represents the number of photons) is necessary for initiation of breakdown process however cascade ionization($\propto I$) is responsible for growth of free electrons and plasma formation [11]. Another intriguing feature observed in the LIB of liquids in concurrence with the transient plasma is the exuberant high speed shockwaves. This violent mechanical effect originates from the confinement of the surrounding liquid. When the hot plasma is formed the surrounding liquid confines the plasma expansion. As a result its expansion gets delayed and primary shockwaves travelling at supersonic velocities emanates [12].

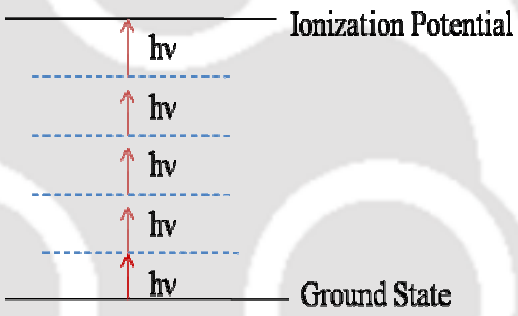

Figure 1.2 *Multiphoton Ionization*

For ns laser–induced breakdown, the plasma formation takes place within the leading edge of the laser pulse. The onset of LIB is registered by visible appearance of tiny spark with the cracking sound. Once the hot plasma is formed, the transient plasma absorbs and scatters the trailing edge of the laser pulse and this leads to laser-plasma interaction. This phenomenon of laser absorption by the transient plasma is known as "plasma shielding" which plays a dominant role in the LIB process at high irradiance ($\geq 10^9$ W/cm^2) as shown in figure 1.3 [13] . For irradiance (I_1, Case A) which is higher than threshold, breakdown occurs at the focus (region x_1) before the laser pulse acquires its maximum intensity as shown in figure 1.3. The further

increase in the laser intensity towards its peak intensity I_2 followed by I_3 creates breakdown at larger distances (x_2 and x_3; Case B and Case C) from the focus where criteria for threshold breakdown are fulfilled. Hence, there is transient development of plasma along the direction of propagation of laser from region x_1 to x_3 within the laser pulse duration.

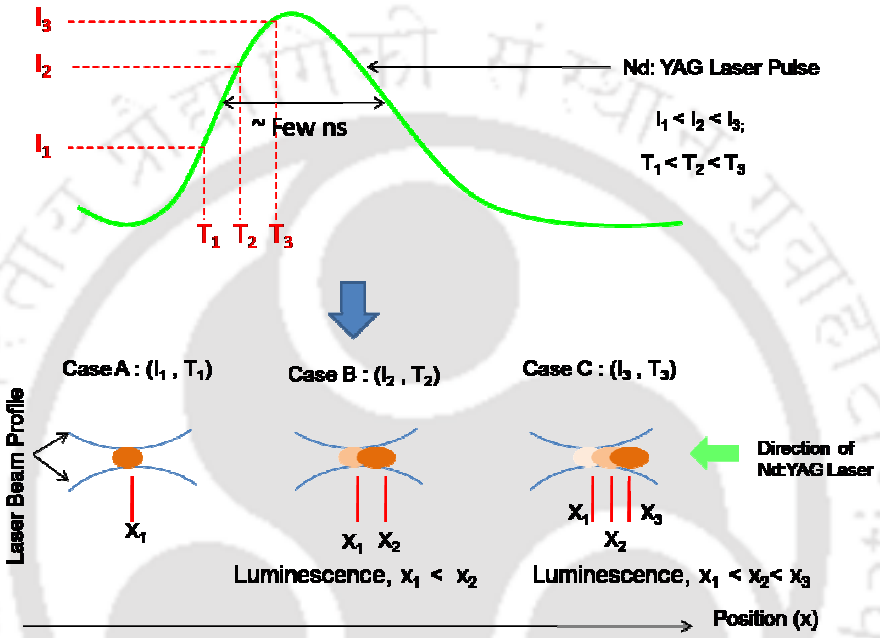

Figure 1.3 *Distributed Shielding at Higher Irradiance*

The absorption and scattering of laser energy by the upstream plasma (x_2 and x_3, regions towards the direction of laser) hinders the breakdown and shields the luminescence at the laser focus (x_1). This is known as "distributed shielding". This leads to filamentous growth of laser induced plasma in the liquids within the Rayleigh length or beyond depending upon the intensity. For ns laser–induced breakdown once the electron density ρ reaches a certain critical electron density ρ_c, electrons are lost via recombination processes [11]. During the recombination process, the excited ionic (or neutrals) species in the breakdown region emits the plasma radiation which is the fingerprint of characteristic atoms, ions and molecules under study. The other major

loss mechanisms occurring during LIB are heat conduction and diffusion to the surrounding liquid medium.

After the laser pulse is over, the plasma cooling occurs and the hot plasma is replaced by vaporized fluid which constitutes cavitation vapor bubbles. The inertia of the vaporized fluid mass leads to cavitation bubble expansion and it reaches a state where the pressure inside the bubble becomes less than the ambient hydrostatic pressure of the surrounding liquid. To maintain the hydrostatic pressure, the bubble implodes and reaches a state where the pressure inside it becomes more than the hydrostatic pressure. The bubble rebounds and emits the excess of energy as a secondary shockwave. The process continues to oscillate till all the energy is dissipated into the surrounding liquid. Several studies on laser-produced cavitation bubbles are reported in the literature [14-18]. For laser induced cavitation, there is also scope of formation of multiple bubbles extending to the Rayleigh length or beyond for the LIB in liquids at higher irradiance due to filamentous growth of plasma, figure 1.3 [19]. The multiple bubble interaction results in bubble coalesce which on itself is a highly complex and asymmetric process [20].

1.2 Laser Induced Breakdown at Solid-Liquid Interface

The schematic of various processes occurring during LIB at solid-liquid interface is depicted in figure 1.4. Laser–induced breakdown (LIB) at solid–liquid interface involves focusing of high power laser onto a solid target immersed in liquid. Deposition of laser energy onto the focal spot results in ablation and plasma formation of the target material. According to Berthe and co-workers once the plasma is formed the surrounding liquid layer confines the plasma [12]. As a result, the plasma expansion gets delayed and a shockwave emanates. The absorption of later part of the

laser pulse and supply of vaporized/ionized species from the target and the neighboring liquid result in further induction of extra pressure to the shockwave which is termed as plasma–induced pressure. As a result, the plasma achieves high pressure and high temperature (HPHT) and becomes highly unstable and induces various chemical reactions depending upon choice of target and its chemical affinity with the surrounding liquid. The various possible routes to chemical reactions induced by this unstable transient plasma is shown in figure 1.5 [8].

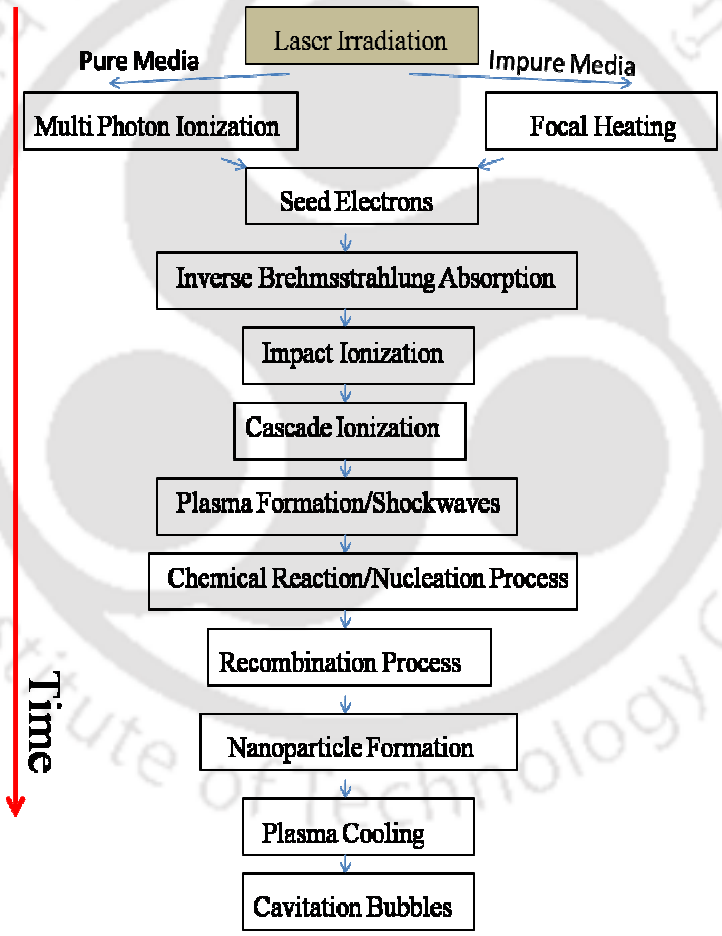

Figure 1.4 *The transient evolution of physical processes in laser induced breakdown at solid-liquid interface*

The first reaction is the direct clustering and nucleation of target plasma into high temperature phases inside the laser–induced plasma. This condition favors formation of high temperature metastable phases, process 1 (figure 1.5). Wang et al. and Yang et al. reported formation of a metastable hexagonal phase of diamond due to direct aggregation of graphite plasma in liquid under HPHT conditions [21, 22].

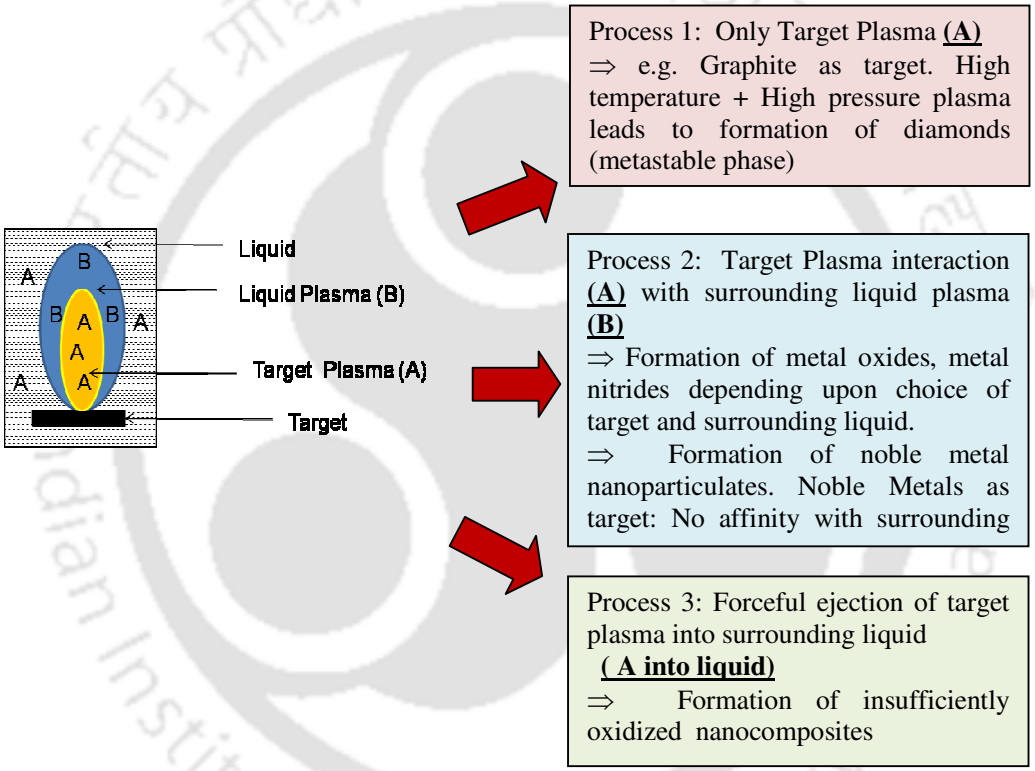

Figure 1.5 *The schematic of chemical processes occurring in laser induced breakdown at target-liquid interface*

The HPHT plasma also favors excitation, ionization and dissociation of the surrounding liquid molecules not only at target-liquid interface but also at plasma–liquid interface. The infusion of liquid plasma into target plasma activates non equilibrium chemical bonding between the target and liquid molecules. This incites

formation of nanoparticles of composites of target materials (e.g. metal oxides in water etc., Process 2) during LIB at target-liquid interface [23, 24]. In addition, the direct chemical bonding at the plasma-liquid interface is possible for very HPHT plasma. This makes formation of high temperature oxide phase feasible [25].

The formation of various noble metal nanoparticles of Au, Ag, has been reported via laser ablation in liquids [26, 27]. The formation of stable nanophase of pure noble materials can be understood from their inertness to the surrounding liquid medium.

The other type of interaction is the forceful impingement of target species due to its extreme pressure into the surrounding liquid. These reactions may result in formation of nanoparticles of various stoichiometries, Process 3. Thus the type of nanoparticles generated depends onto the target plasma and its affinity to the surrounding liquid/liquid plasma and as well as the HPHT conditions prevailing in the region of breakdown.

1.3 Significance and Current status of LIB at liquid/solid-liquid interface

Pulsed laser–induced breakdown in liquids and at target–liquid interface has significant implementation in the field of medical sciences, micromachining, lithography, laser–induced isotope separation, laser–induced breakdown spectroscopy and nanoparticle synthesis [28-39]. In the field of medicine, the laser–induced plasma and the emitted shockwaves assist in dissection of cellular organelles, cytoskeletal filaments and cellular organelles. LIB is also useful in intraocular surgery and fragmentation of kidney stones. The cavitation bubbles formed at later stage during LIB of liquid are the main driving source of laser–assisted tissue cutting, removal of thrombus from obstructed arteries, expulsion of bile duct stones via fragmentation and

lithotripsy [40-43]. However, the expanded shockwaves and onset of cavitation bubbles are not always desirable as they may result in dilation and collateral damage of adjacent tissues. Vogel et al. showed that focusing the laser on the surfaces of tissues at low energy reduces the damaging effects [44]. To minimize the cavitation effect, two pulses, pre-pulse of lower energy and ablative pulse of higher energy are used. This helps in lowering the dilatation by choosing the suitable energy ratios between pre-pulse and ablative pulses [45]. Further formation of multiple bubbles during LIB leads to bubble coalescence which may severely damage the surrounding healthy tissues. Hence, there is a need to gain an insight onto the dynamics of emitted shockwaves and to control the damaging effects of shockwaves and thus minimize the cavitation effects for clinical applications.

Another powerful implication of the laser–induced breakdown process is the study of the emitted spectrum of laser–induced plasma commonly termed as laser–induced breakdown spectroscopy (LIBS) [46]. The emitted spectrum in laser–induced plasma is the finger print of the ionic, atomic and molecular species of the medium under consideration. In LIBS technique, radiation emitted from the plasma can be imaged onto a spectrometer/monochromator to record the characteristic emitted spectra. Therefore LIBS acts as a powerful chemical sensor for the detection of trace elements in water and submerged targets, sediments and rocks under ocean, environmental pollutants and corrosion extent in nuclear power plants, leakages in industrial plants, in studies of microbiological activities, etc. [46-53]. However for LIBS in liquids, there are certain issues such as poor SNR (signal-to-noise-ratio), low sensitivity and detection limit for which the technique needs further development and upgradation to make it user friendly for commercial use [54].

Laser induced breakdown at target-liquid interface has been suitably employed for material processing where the underwater laser–induced shock processing is used to change the material structure and stress state [55]. Shockwave propagation in material creates dislocation and plastic deformation. High density dislocation helps in higher surface hardness and corrosion resistance whereas plastic deformation induces enhanced fatigue strength to the sample under study [56-61]. In laser-assisted steam cleaning of contaminated surfaces, a liquid film is deposited onto the contaminated surface, e.g. chips used in semiconductor industry. Irradiation of laser then results in forceful evaporation of the liquid film alongwith the contaminated particles within a depth of few nm which otherwise is difficult to remove by conventional techniques due to strong adhesion of smaller particles [61, 62]. Laser–induced lithography is another application of LIB to generate the nanopatterns [63-65]. Recently several studies on liquid immersion lithography with nanopatterns down to 32 nm have been reported [66-67]. The advantage of liquid immersed lithography is the shorter effective wavelength (due to the refractive index of the liquid immersed between the last optics and the sample) which enables higher resolution and increase in depth of focus which makes the displacements of photoresist (sample) less critical.

In the recent years, most of the studies on LIB at solid-liquid interface were focused on synthesis of various nanoparticles depending upon the choice of target and its chemical affinity to the surrounding liquid [8]. It was found that the liquid medium plays a crucial role in LIB at solid–liquid interface. The surrounding liquid not only leads to confinement of plasma but its physical property such as polarity, and temperature decides the morphology, stability and growth of the synthesized nanoparticles [68-69]. The effect of liquid temperature onto the growth of nanoparticles was investigated. It was reported that the shape of nanoparticles can be

suitably tuned from irregular to rod-like structures by varying the liquid temperature [68]. When the ablation were carried out in different liquid (ethanol, water and acetone) medium, it was found that ablation in ethanol media gives aggregated particles with a broad particle size distribution as compared to water and acetone. The possible reason for this observation was attributed to higher dipole moment of acetone (2.85 D) and water (1.85 D) which forms strong double layer compared to low polarity ethanol (1.69 D) [69]. In pulsed laser ablation, the nanoparticles are present in the colloidal form. The the overall colloidal solution is electrically neutral but the nanoparticles synthesized in liquids are surface charged. Hence any charged surface is always balanced by counter-ions of opposite signs present in the liquid. The choice of polar solvents as a liquid medium and its interaction with surface-charged nanoparticles results in an electrical double layer. During laser ablation, the strong double layer around nanoparticles obstructs plasma nanoparticle interaction and restricts the particle growth. Even after laser ablation, the overlapping of the double layer also averts nanoparticle–nanoparticle interaction and avoids particle aggregation. Since ethanol forms weak double layers, it results in unstable and large sized particles. Thus the appropriate choice of liquid can play an important role in controlling the size of the nanoparticles synthesized via LIB process.

The characteristic features of the nanoparticles can also be modulated via suitable selection of source laser parameters. The laser pulse duration, wavelength and fluence, plays a dominant role in the ablation mechanism and influences the particle size distribution. There are several reports on synthesis of nanoparticles using continuous wave (cw), long pulsed, nanosecond (ns) and femtosecond (fs) lasers [70-74]. Unlike ns pulses, the rapid quenching time for fs laser hinders interaction of plasma with the surrounding liquid and favours the formation of pure metal

nanoparticles irrespective of its affinity to the surrounding medium. Considering the effect of the pulse duration on the particle statistics, the average particle size for fs laser ablation is uniform and larger than those of the ns and long pulsed lasers for metal nanoparticles. This is because, once the nanoparticles are formed and dispersed into the surrounding liquid, further irradiation of the ns laser with incident wavelength, matching with the surface plasmon resonance range of metal nanoparticles heats its electrons. This is followed by the electron–phonon relaxation process which increases the nanoparticle internal kinetic energy and temperature which leads to melting and further fragmentation of the nanoparticles. This effect is not pronounced in the fs duration laser as electron-phonon relaxation process is longer (~ 100 ps) than fs laser pulse duration [72]. For long pulsed ablation, particle size also depends on power density. According to Sun and co-workers, long pulsed ablation at 1.2 ms results in low power density which generates low pressure and low temperature conditions, and thus results in smaller particles [73]. Tsuji and co-workers, Yeh and co-workers and Nichols and co-workers reported the dependence of the incident wavelength onto the size of nanoparticles[75-77]. Nd:YAG (ns) laser ablation at 532 nm and 355 nm resulted in smaller nanoparticles compared to the fundamental infrared wavelength at 1064 nm. During pulsed laser ablation, the nanoparticle synthesized from preceding pulse blocks and absorbs the succeeding pulse. For most of the nanoparticles the Plasmon band and molecular band (electronic transitions) lie in the visible and UV visible range respectively, hence the absorption of the incident wavelength during ablation at 532 nm and 355 nm is more pronounced compared to the IR wavelength. The self-absorption by nanoparticles for lower wavelength decreases the ablation efficiency, as the energy reaching the solid target decreases but results in heating and fragmentation of the nanoparticles and leads to a

smaller particle size distribution [75]. The laser fluence also plays an essential role in determining ablation efficiency and particle sizes. Large nanoparticle sizes are observed for higher fluence. This may be due to the combined effect of high plasma density and high impingement force on the target. Higher fluence at the target leads to formation of high density plasma which enables the increase in molecular interaction and hence particle sizes. The high fluence also induces high target impingement force which results in direct ejection of molten globules along with the vaporized/ionized target species and hence increases the size of the particulates.

Most of the analyses in LIB at solid-liquid interface are oriented towards the variation in laser parameters and properties of liquid medium to change the characteristic traits of the nanoparticles. However, very few reports were focused on the complete investigation of the nucleation mechanism of nanoparticles synthesized via laser induced breakdown at solid-liquid interface [9].

1.4 The present Work

In view of the above context and taking account the complexity of the LIB process, a comprehensive study is undertaken to investigate the transient evolution of laser induced breakdown in liquids. Further, the implication of complete hydrodynamics of LIB at target-liquid interface onto the nucleation mechanism of various nanoparticulates is elucidated. The earlier reports on nanoparticle generation via pulsed laser ablation at target–liquid interface were confined to synthesis and characterization except the recent studies of Wang et al. where the effect of plasma dynamics onto the growth of nanocrystalline diamonds was reported [78]. Park and co-workers, and Fabbro and co-workers have also studied transient evolution of temperature and pressure during laser ablation at solid liquid interface but the effect

of these conditions on the nucleation of metal oxide nanoparticulates has not been explored in detail so far [79,80]. Hence, it will be of significance to investigate the laser induced plasma in liquid/solid-liquid interface and elucidate the effect of plasma properties on nucleation of metal oxide nanoparticles for quality control and size-selective applications. In addition the applicability of the synthesized metal oxide nanoparticles as photocatalyst and antibacterial agent is also reported in the present thesis.

Chapter 2 explains the basic design and fabrication of the laser ablation set-up. The various diagnostics used to investigate the laser induced breakdown process in liquid/solid-liquid interface via beam deflection set-up, shadowgraphic techniques, external electric probe and laser induced breakdown spectroscopy are discussed. Further, the experimental details for testing the applicability of nanoparticles are also explained.

Chapter 3 involves extraction of the dynamics of various physical processes of LIB in liquid. The effect of laser energy onto shockwave velocities and cavitation bubble dynamics is reported. The multiple bubble hydrodynamics and bubble coalescence is studied. The constituent species formed during laser produced water plasma are identified. The influence of laser energy on thermal diffusion of plasma charge carriers is elaborately explained in this section.

Chapter 4 is mainly related to the implication of diagnostics discussed in chapter 2 at titanium-water interface. The estimation of physical conditions; pressure (using beam deflection set-up) and temperature (from laser induced breakdown spectroscopy) at the interfacial region is employed to unveil the nucleation mechanism of metal oxide nanoparticles. A theoretical estimate of nucleation time, growth velocity and size of nanoparticles are also constructed.

Chapter 5 describes the synthesis of titanium oxide and copper oxide nanoparticles via laser induced breakdown at titanium-water and copper-water interface respectively. In addition, chapter 5 correlates the estimated size of titanium oxide nanoparticles discussed in chapter 4 to that of experimentally observed size of titanium oxide nanoparticles. Further the laser focusing conditions during the breakdown process is also varied and its effect on tailoring the size, shape and structure of these metal oxide nanoparticles is reported.

Chapter 6 enlightens the applicability of the metal oxide nanoparticles as a photocatalyst and antibacterial agent. The entire thesis work is finally concluded with future scope in chapter 7.

Chapter 2

2. Experimental Details

In Laser Induced Breakdown (LIB) of liquids, a high power laser is focused inside a liquid medium as shown in figure 2.1. This results into excitation, ionization and dissociation of water molecules resulting in elongated water plasma. The time integrated image of water plasma is shown in figure 2.2. Figure 2.3 shows the LIB process at target-liquid interface. Laser irradiation onto a target immersed in liquid leads to target ablation and plasma formation. This eventually leads to formation of metal oxide nanoparticles under suitable conditions [24]. The time integrated plasma image at target-liquid interface is shown in figure 2.4.

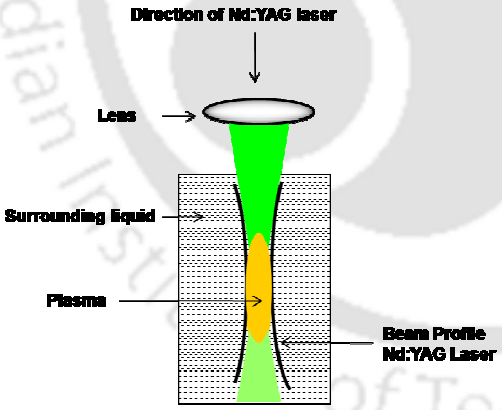

Figure 2.1 *LIB in liquids*

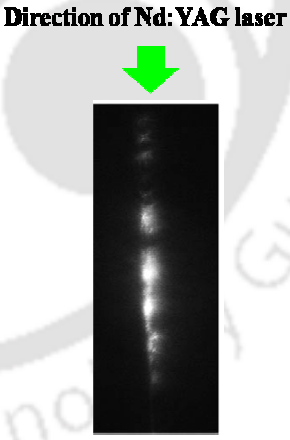

Figure 2.2 *Time integrated image of laser produced water plasma*

To investigate the laser induced breakdown process in liquid/solid-liquid interface, various diagnostics were employed in the present work. This includes Beam

Defelection Set-up (BDS), Shadowgraphy (SG), External Electric Probe (EEP) and Laser Induced Breakdown Spectroscopy (LIBS). The experimental details for all these diagnostics are elaborated in the subsequent sections. Further, LIB at titanium-water and copper-water interface was used to synthesize titanium oxide and copper oxide nanoparticles respectively. The focusing condition of the source Nd:YAG laser onto the target was varied to control the size and structural properties of these synthesized nanoparticles. The experimental set up for testing the applicability of these nanoparticles as antibacterial agent and photocatalyst are also discussed in the present chapter.

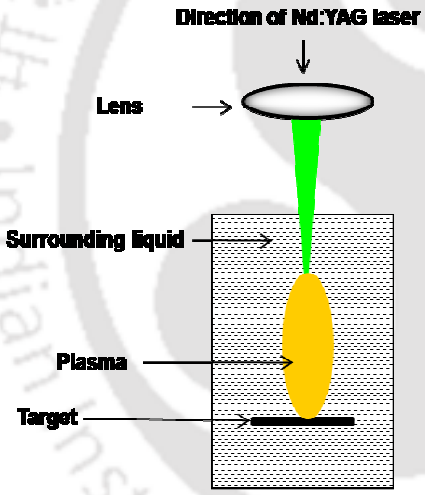

Figure 2.3 *LIB at target-liquid interface*

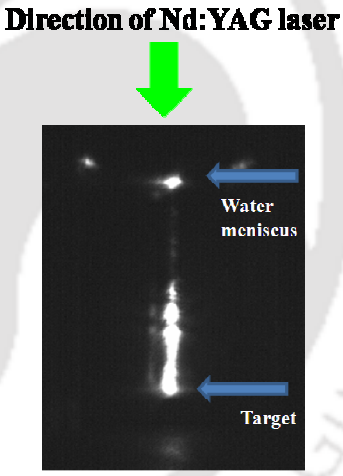

Figure 2.4 *Plasma image at target-liquid interface*

2.1 Laser Induced Breakdown In Liquids

To study the LIB at high laser energy in the range of 24-170 mJ, a symmetric 40 KF double cross made up of stainless steel was used as a liquid cell as shown in figure 2.5. The length of the double cross was 22 cm. The bottom port was terminated with 40 KF blank flange. The horizontal ports were appended with glass windows for

deployment of laser and other optical diagnostics. The top port was kept open for changing water and insertion of electrical probes. The cell was mounted on Perspex stand as shown in figure 2.5. The laser was focused with a 10 cm lens in the centre of the cell after steering the beam with 90˚ prism as shown in figure 2.6. The LIB at low energy of 10 mJ was not observed using a 10 cm focal length lens. Hence a 5 cm focal length lens was used and for compatibility the liquid cell made up of quartz cuvette of dimension $1 \times 1 \times 4.5$ cm^3 was chosen. The various diagnostics deployed and its basic principle is discussed in the following sections. The experimental conditions used for studying LIB in water are listed in Table 2.1

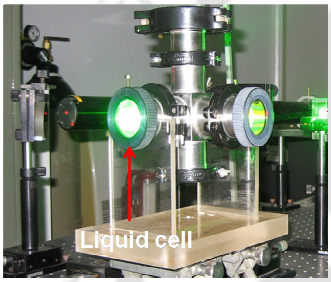

Figure 2.5 *Photograph of liquid cell*

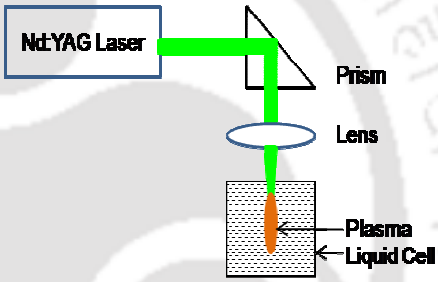

Figure 2.6 *Schematic of LIB in water*

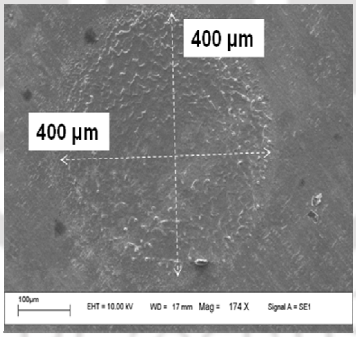

Figure 2.7 *Laser spot sizes onto a titanium target for laser energy of 0.2 mJ using a 5 cm focal length lens*

The laser fluence was estimated from the laser energy and the laser spot size. The laser energy was measured using an energy meter (Model No. 13 PEM 001). To measure the spot size, a single shot of laser was irradiated onto a titanium target and

the SEM (Model No. Leo 1430vp) image as illustrated in figure 2.7 was used to enumerate the spot size.

2.1.1 Beam Deflection Set-up (BDS)

To measure the velocities of shockwave, charged particle and cavitation bubbles, Beam Deflection Set-up (BDS) was assembled. For this, a cw He-Ne laser beam (Melles Griot, Model No. 05-LHR-991) was aligned transverse to the direction of Nd: YAG laser beam and was made to pass through the breakdown region as shown in figure 2.8. The transmitted He-Ne beam was detected by the photodiode (PD1), Model No. 13 DSI 001. The photodiode O/P was displayed onto Digitial Storage Oscilloscope (DSO), Tektronix Model No. TDS 2012 via 50 Ω terminator interfaced to computer. The PD1 detects a small fraction of He-Ne beam as the size of the He-Ne beam was 0.65 mm (beam diameter $1/e^2$) whereas the sensitive area of photodiode was 0.31 mm^2. The photodiode was initially aligned to detect the maximum signal corresponding to the centre of the Gaussian beam from the output of the He-Ne laser as shown in figure 2.9 (a). The formation of laser produced plasma/shockwaves and cavitation bubbles resulted in change in refractive index, which in turn deflected the He-Ne beam as illustrated in figure 2.9 (b). The deflection was registered in the form of a dip (modulation) in PD1 signal. When the transient plasma is over, the He-Ne beam comes back to its original path and the photodiode to its initial level (figure 2.9 (c)). The modulated BDS Trace is shown in figure 2.9 (i) where the region (a)-(c) is compared to the He-Ne location of figure 2.9 (a)-(c) respectively. The DSO was externally triggered with the Nd:YAG laser pulse for the reference signal.

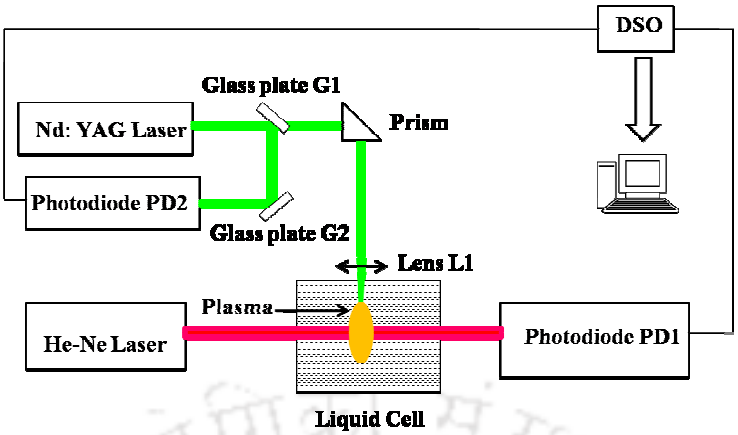

Figure 2.8 *The schematic of BDS set-up*

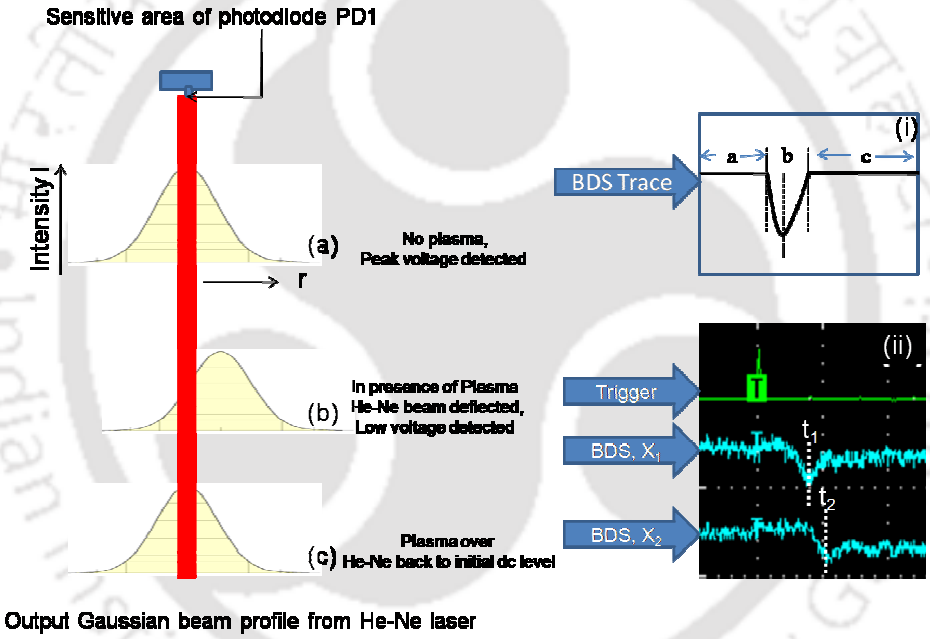

Figure 2.9 *Temporal evolution of signals from BDS*

The externally triggered signal was taken from 4% of 4% reflection of the Nd:YAG laser pulse from Glass Plates 1 and 2, figure 2.8 and fed onto the photodiode (PD2) and displayed onto the other channel of DSO.

To measure the deflection at different location w.r.t. the breakdown region, He-Ne laser and PD1 were moved simultaneously along the direction (source Nd:YAG laser) of expansion of plasma. Figure 2.9 (ii) shows the PD1 signal at two different locations

x_1 and x_2 .The time delay, t_1 and t_2 w.r.t the Nd:YAG laser pulse, for deflections incurred at distances x_1 and x_2 respectively is used to measure the velocities.

2.1.2 Shadowgraphy Technique

The laser induced plasma at later stage (after termination of source laser) leads to formation of cavitation bubbles as discussed in section 1.1. The detailed schematic of experimental set-up for imaging laser induced cavitation bubbles via shadowgraphy using a charge-coupled device (CCD) (PCO PixelFly scientific) camera is shown in Figure 2.10. For this, a Q-switched Nd:YAG laser (Model No. Minilite I, λ= 532 nm, pulse duration ~ 10 ns) was focused (from top) inside a quartz cuvette filled with distilled deionized water (conductivity<1$\mu\Omega^{-1}$) with a lens L1 of focal length 5 cm. The experiment was performed in single shot mode and was repeated for forty laser shots for each data point. Considering the complexity of the experimental set-up for ShadowGraphy (SG) technique, a simple quartz cuvette instead of stainless steel double cross was taken as a liquid cell. For shadowgraphic images, a probe He-Ne laser (Model No. 05-LHR-991, λ = 632.8 nm, 75 mW) was aligned perpendicular to the direction of the incident beam to record the bubble images. Since the water plasma followed by cavitation bubbles extends up to the Rayleigh length of source laser, the probe beam was expanded by the microscopic objective (10X) to illuminate the focal volume and hence the bubbles. The expanded He-Ne beam after passing through the bubbles was imaged onto the CCD by a lens L2 (focal length 15 cm) in 1:1 to record the images. The neutral density filter (optical density O.D 2.6) was placed in front of CCD to avoid the saturation.

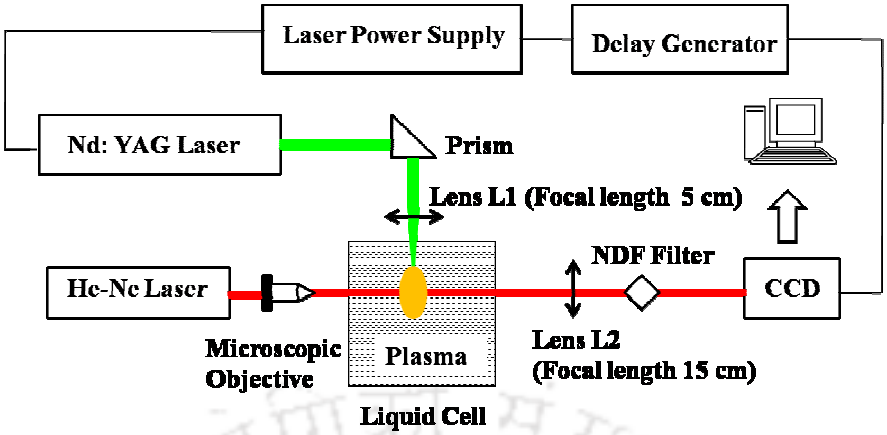

Figure 2.10 *The schematic of SG technique*

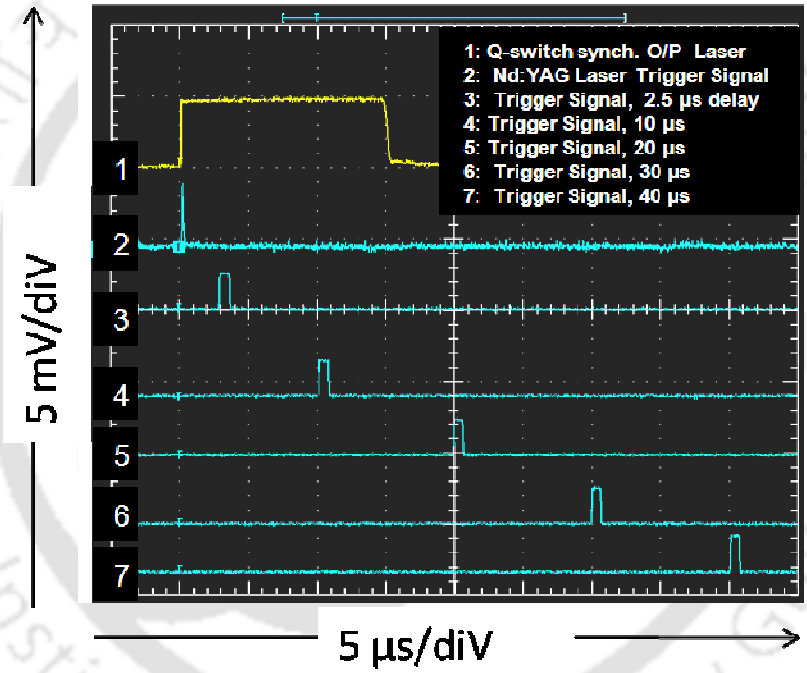

Figure 2.11 *The pulse sequence for externally triggering CCD*

To record the temporal evolution of bubbles, CCD was triggered externally at different intervals of time w.r.t. the Nd:YAG laser. For this, the synchronous output from the Q-switched Nd: YAG laser was fed to trigger a pulse delay generator (Philips, PM 5786 B). The delayed output pulse from the delay generator was used to trigger the CCD externally at a desired interval. The pulse sequences for external

triggering of the CCD are shown in figure 2.11. Trace 1 represents the synchronous output of the Nd:YAG laser. Trace 2 corresponds to the O/P of Nd:YAG laser pulse (section 2.1.1). The minimum exposure time of the CCD is 10 µs. Trace 3-7 depicts the externally triggered CCD signals after 2.5, 10, 20, 30 and 40 µs of the laser pulse. Thus the size of the bubble was measured at a regular interval of 10 µs from the corresponding bubble images captured by the CCD.

2.1.3 External Electric Probe (EEP)

To study the transient evolution of diffusion charge carriers in the LIB in water, External Electric Probe (EEP) was used. The schematic of experimental set-up for EEP is shown in figure 2.12. The second harmonic of Q-switched Nd: YAG laser (Model No. HYL -101, λ= 532 nm, pulse duration = 10 ns), was focused by a 10 cm focal length lens inside a liquid cell filled with normal tap water, which resulted in plasma formation. To collect the charge carriers, two disc shaped electrodes (electrodes A, B) made of metal plate of copper, thickness ~1 mm and diameter ~ 1.6 cm were immersed in the water. The electrodes were mounted using a double-sided tape onto a Teflon holder, having provision for adjusting the electrode spacing as shown in figure 2.13(a). The photograph of the liquid cell with the electrode assembly inserted inside is shown in figure 2.13(b). The separation between electrodes was adjusted to ~3 mm so as not to perturb the plasma plume (size ~ 500 µm at 170 mJ, figure 2.12). The laser was focused in between the two electrodes. A (0-25 V) DC power supply was used to apply the electric field across the electrodes. The transient currents recorded due to creation of LIB of water were measured by displaying the voltage drop across 100 Ω resistance connected towards the grounded electrode onto the DSO (Model No. TDS 2012). The DSO was externally triggered as discussed in

section 2.1.1 and is also shown in figure 2.12

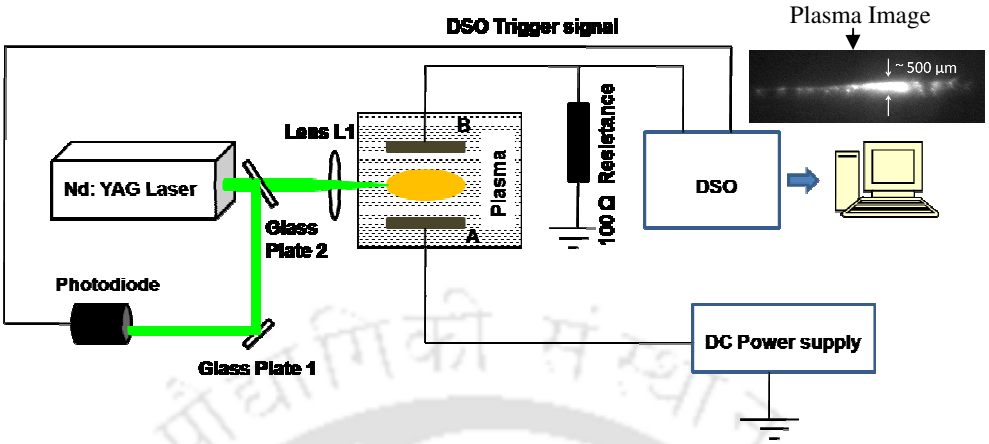

Figure 2.12 *The experimental set-up for collection of charge carriers*

Figure 2.13(a) *Electrode mounting on Teflon holder* ***(b)*** *Photograph of electrodes immersed inside liquid cell*

2.1.4 Laser Induced Breakdown Spectroscopy (LIBS)

Laser induced plasma emits the characteristic line and band spectra of its constituent species. This emission spectrum is used to study the chemical kinetics and to measure the temperature of the laser induced plasma. The schematic of the experimental set-up, used for recording LIB emitted spectra is shown in Figure 2.14(a). The focusing of laser in the liquid cell was similar to that of discussed in section 2.1. The radiation from the laser produced plasma was imaged by lens L2 (focal length 10 cm) onto the entrance slit of the monochromator (Model No. 750 M Spex), and detected by the PMT at the exit slit of the monochromator interfaced with the computer. The

monochromator was scanned in the spectral range of 190-850 nm to record the band spectra of OH, O_2 and H_2O. The ratio of emission intensities of molecular bands was used to deduce the rotational temperature.

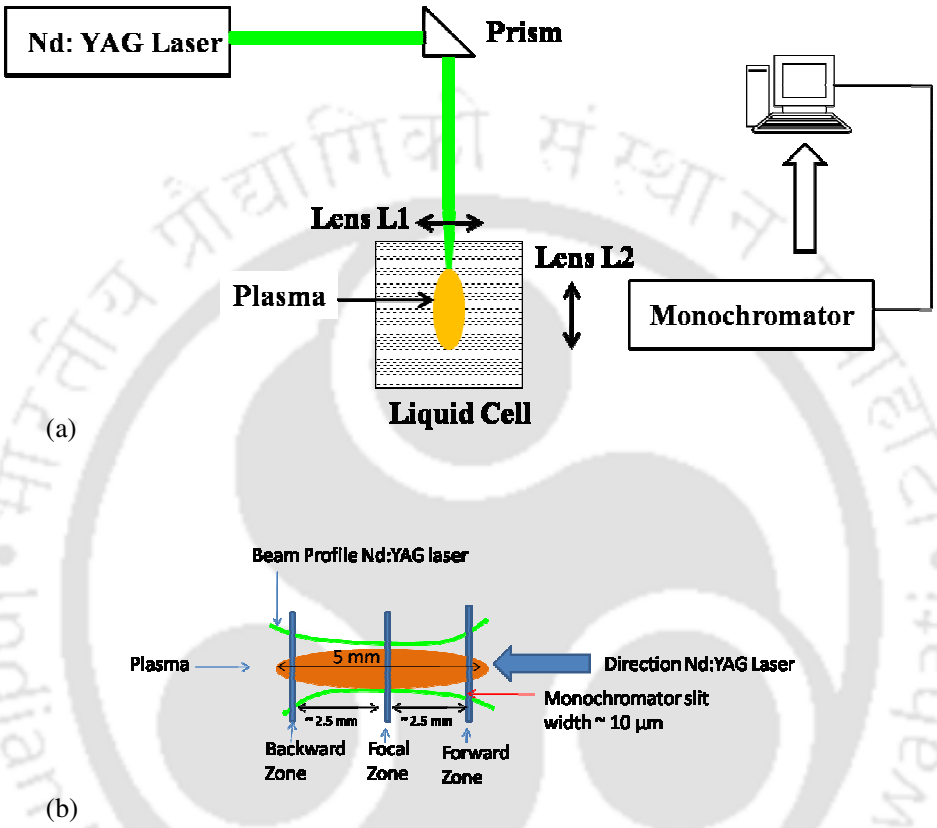

Figure 2.14(a) *The schematic of LIBS set-up* ***(b)*** *Schematic for recording spatial evolution of plasma kinetics*

The formation of water plasma is observed visually in the form of an elongated spark (size~5mm) as shown in figure 2.2. To study the variation in the chemical kinetics occurring at different regions of water plasma, the different sections of the water plasma was imaged separately onto the entrance slit of monochromator (size ~10µm) as shown in figure 2.14(b). The region towards the direction of laser is marked as forward zone, the central section of plasma is the focal zone and the rear end of plasma away from the direction of laser is the backward zone.

Table 2.1 *Experimental details of LIB in liquids*

Laser Induced Breakdown In Liquids				
Characterization	Lens Focal Length cm	Laser Energy mJ	Spot Size At Focus µm	Laser Fluence J/cm^2
BDS	10	24	130	180
		83	130	625
		170	130	1300
	5	4	80	80
SG	5	10	80	200
EEP	10	24	130	180
		83	130	625
		170	130	1300
LIBS	10	24	130	180

2.2 Laser Induced Breakdown at Target-liquid Interface

LIB at metal water interface is employed to synthesize various metal oxide nanoparticles [8]. To understand the nucleation mechanism of these nanoparticles, the physical conditions at the metal-water interface were investigated. LIBS and BDS techniques were used to get an estimate of plasma temperature and shockwave pressure respectively at the metal-water interface.

2.2.1 Laser Ablation at Titanium-water interface

The schematic of the experimental set-up to study the laser ablation at titanium-water interface is illustrated in figure 2.15. The second harmonic of high power Q-switched Nd:YAG laser (λ = 532 nm, Model No. Minilite I) steered with mirror M, is focused by a 5 c.m. focal length lens (Rayleigh length ~ 1.3 mm) onto a titanium target (purity 99.7%, dimension : 1x1x0.3 cm^3) placed inside a glass cuvette of dimension 10X10X10 cm^3 filled with distilled deionized (conductivity < $1\mu\Omega^{-1}$) water. The height of the liquid column from the target surface was kept around ~ 18 mm. The laser (pulse width = 5 ns) was operated at the repetition rate of 15 Hz with laser energy of 4 mJ per pulse.

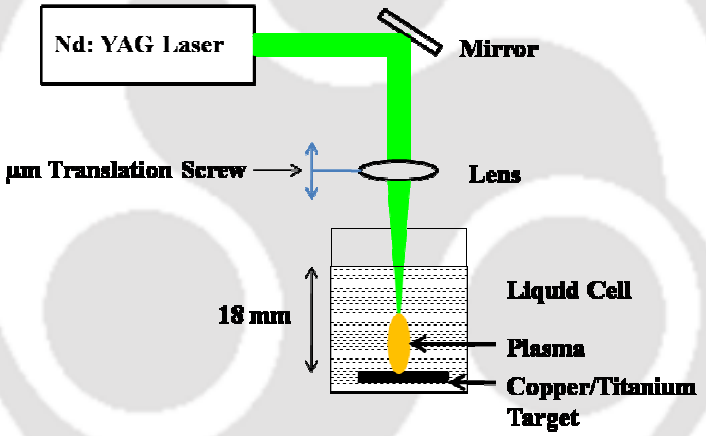

Figure 2.15 *Laser Ablation set-up at Target-.liquid Interface*

The experiment was performed for different focusing conditions on to the titanium target as illustrated in figure 2.16(a). For this, the lens was mounted onto a vertical translation stage attached with a micrometer (µm) screw as depicted in figure 2.15. The location of target w.r.t focal point is depicted in figure 2.16 (b). When the laser was tightly focused onto the target, the focusing condition is labeled as 0 mm. For above focus, the lens was moved 10 mm upward and for below focus it was moved 5 mm below the tightly focused region. The laser spot size at various focusing

condition is shown in figure 2.17 and listed in table 2.2.

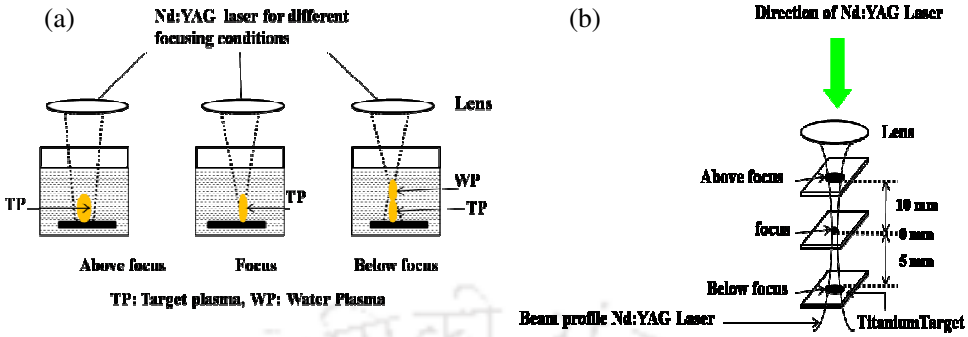

Figure 2.16(a) *The focusing conditions for Titanium target immersed in water* ***(b)****Location of target w.r.t focus*

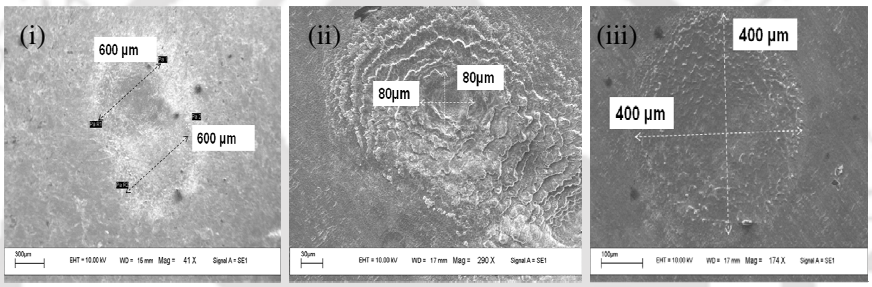

Figure 2.17 *The laser spot size onto Titanium target immersed in water (i) Above focus (ii) Focus (iii) Below focus.*

For below focus condition, there was breakdown of water at the focal region, above the target and hence the laser energy reaching at the target was less compared to that of the other two cases (focus and above focus). To measure the laser energy reaching the target for below focus condition (figure 2.16 (b), below focus condition), the experimental set-up shown in figure 2.18 was employed. The source laser beam after passing through the breakdown region was transmitted through the bottom glass surface of the liquid cell. The beam was reflected by a glass plate G (reflection of 4%) and made to fall onto the laser energy meter. The major part of the energy was consumed in the breakdown of water. The remaining laser energy (after the water breakdown) falling at the target beyond focus was measured to be 0.3 mJ (after accounting reflections from the surfaces). The laser fluence for all the focusing

conditions is listed in Table 2.2.

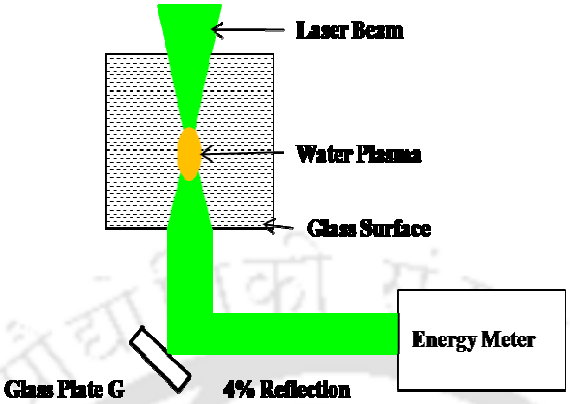

Figure 2.18 *Energy measurement for below focus condition.*

To study the LIB process at titanium-water interface, BDS and LIBS set up were employed. The experimental set-up for BDS and LIBS are shown in figure 2.19 and 2.20. These experimental set-ups are similar to that discussed in section 2.1.

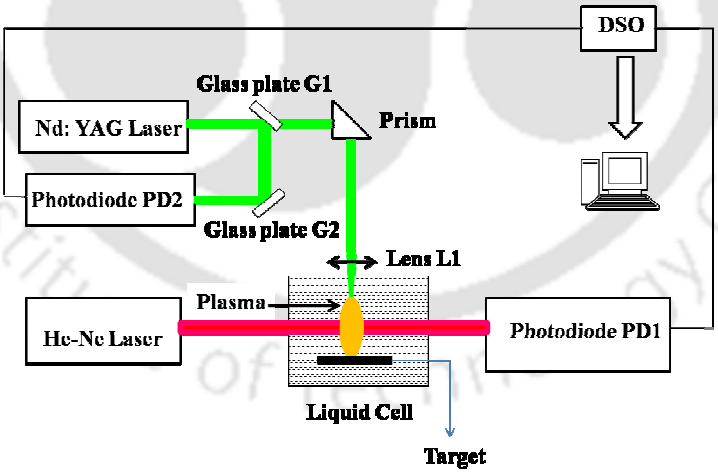

Figure 2.19 *The schematic of BDS at target-water interface*

The only difference is that a solid titanium target was placed at the bottom of liquid cell such that the laser is focused onto titanium-water interface. Further, BDS and

LIBS experiments were also performed for various focusing conditions shown in figure 2.16. The detailed experimental parameters are listed in Table 2.2.

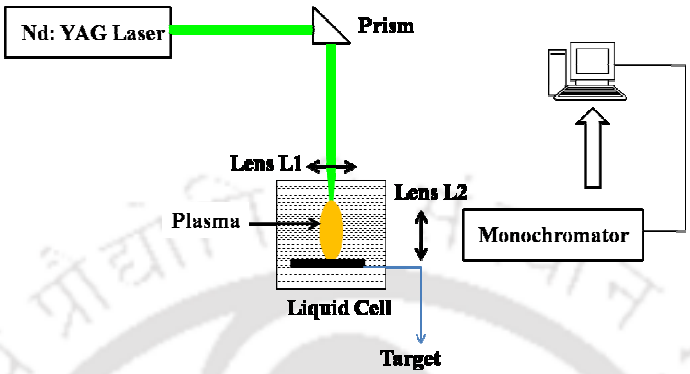

Figure 2.20 *The schematic of LIBS at target-water interface*

2.2.2 Synthesis and Characterization of Nanoparticles formed at Titanium/Copper-Water Interface

The photograph of experimental set-up for the synthesis of the nanoparticle of titanium oxide and copper oxide is shown in figure 2.21. The set-up was similar to that of discussed in section 2.2.1. The Ti/Cu target immersed in 10 ml glass beaker filled with water was exposed to Nd:YAG laser with a 5 cm focal length lens. The various focusing conditions for synthesis of titanium oxide have been discussed in section 2.2.1 and is shown in figure 2.16.

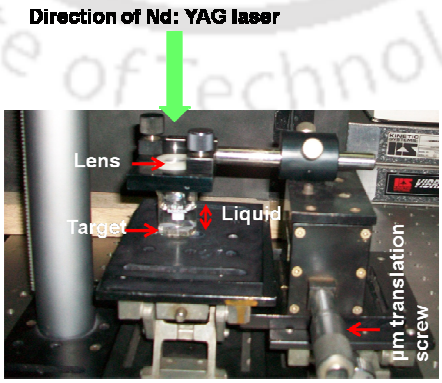

Figure 2.21 *Experimental setup for synthesis of nanoparticles via laser target liquid interaction*

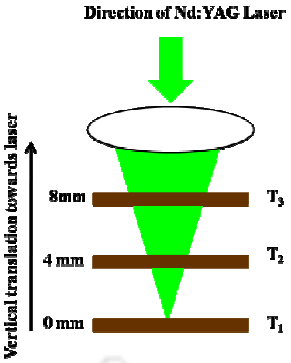

Figure 2.22(a) *The focusing conditions at copper-water interface*

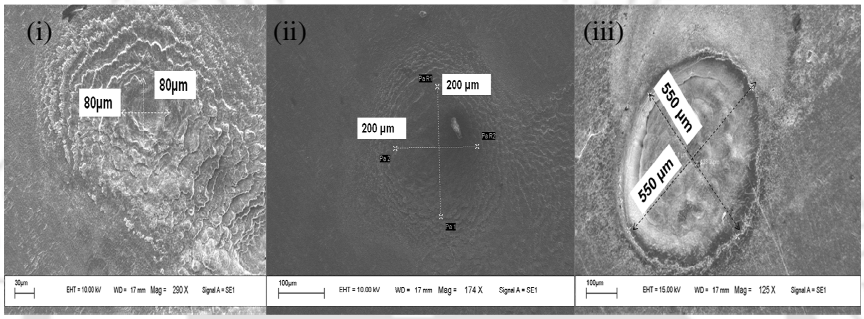

Figure 2.22(b) *The laser spot size onto Copper target immersed in water for (i) T_1 (ii)T_2 (iii) T_3*

The focusing condition for the synthesis of copper oxide is depicted in figure 2.22 (a). The target was ablated independently at three different laser focusing conditions ($T_{1,\ 2,\ 3}$). For this, the target was moved from laser focal spot (0 mm, position T_1) along the direction of incident laser with the help of an attached micrometer vertical translational screw as shown in figure 2.15. The other target positions for ablation are marked as T_2 and T_3 which are placed at 4 mm and 8 mm above the focal spot (T_1, 0 mm) of the laser. The laser spot size onto the target for all the focusing condition is shown in figure 2.22(b). The laser fluence at all these focusing conditions is listed in Table 2.2. The titanium-water interface was irradiated with Nd:YAG laser for 30 minutes (27,000 shots) whereas copper-water interface was irradiated for 15 minutes (9000 shots). After laser exposure a colloidal solution was formed which contained the synthesized copper/titanium oxide nanoparticles.

Table 2.2 *Experimental details for LIB at target-liquid interface*

Laser Induced Breakdown at Target –Liquid interface				
Characterization	Target	Laser Energy (mJ)	Spot Size On target μm	Laser Fluence J/cm^2
BDS	Titanium	4	600 (above focus)	1.4
		4	80 (focus)	80
		0.3	400 (below focus)	0.2
LIBS	Titanium	4	80 (focus)	80
Nanoparticle Synthesis	Copper	25	80 (T_1)	500
		25	200 (T_2)	80
		25	550 (T_3)	10
	Titanium	4	600 (above focus)	1.4
		4	80 (focus)	80
		0.3	400 (below focus)	0.2

To unfold the structural properties of the nanocolloids, TEM (JEOL JEM 2100) images and Raman (LabRam HR 8000.) spectra were acquired.To capture the TEM images, the colloidal solution were centrifuged and a drop of concentrated solution was dried onto carbon coated copper grid. For Raman measurements, the colloidal solution was dried onto Silicon/glass substrate and the baseline correction for the substrate was recorded before taking the Raman spectra of colloids. In addition, to

study the optical properties of the nanomaterials, *in-situ* prepared colloidal solutions were taken for recording the Photoluminescence (PL), (Model No. FSP920) and UV-VIS (Varian Cary 50 Bio) spectra

2.3 Application of Nanoparticles

In this section, the experimental details for testing the application of synthesized copper oxide and titanium oxide nanoparticles via laser target-liquid interaction is presented. The antibacterial activity of Copper oxide nanoparticles and photocatalytic activity of Titanium oxide nanoparticles are demonstrated. The experimental conditions are listed in Table 2.3.

2.3.1 Antibacterial Activity

To test the antibacterial activity, two gram negative bacteria *E. coli* and *S. paratyphi* and one gram positive bacteria – *Listeria* were choosen. These bacterial cultures were then exposed to copper oxide nanoparticles. The effect of copper oxide nanoparticles on the different bacteria cultures were diagnosed using Raman probe, UV-Vis spectra and Viability assay.

2.3.1.1 Raman probe

To record the Raman spectra, 12 hr grown subculture of bacterial cultures (*E. coli*) was mixed with nanoparticle suspension of copper oxide (concentration 1.32 mg/ml). The bacterial cultures after treatment were incubated at 28^{o}C and 180 rpm in orbital shaking incubator for 6 hrs. To prepare the samples for measuring the Raman spectra, the solution was centrifuged and a drop of concentrated precipitate was dried onto the Silicon wafer. The Raman spectra of this sample was recorded using He-Ne laser as excitation source at 632.8 nm.

2.3.1.2 UV-VIS Probe

To study the growth curve of bacteria, the bacterial cultures (*E. coli* and *S. paratyphi*) were grown in liquid NB media for 12 h. After two subcultures, 50 µl of 6 h grown fresh culture was inoculated in 2 ml fresh liquid nutrient broth (NB) and treated with Copper Oxide nanoparticles at concentrations of 0.84 and 1.32 mg /ml. Cultures were incubated at 28^{o}C and 180 rpm in orbital shaking incubator for 8 hrs. Optical density (OD) measurements were taken at 600 nm using a UV-Vis spectrophotometer (Varian Cary 50 Bio) to monitor the bacterial cultures.

2.3.1.3 Viability assay (Bactericidal effect)

To investigate the effect of nanoparticles on viability of the bacteria, the bacterial strain (*E. coli*, *S. paratyphi* and *Listeria*) were grown in liquid NB for 12 h. These were subcultured twice and 6 h grown fresh cultures were used for viability test. Aliquots of 100 µl of the cultures were subcultured in fresh NB media (2 ml) and treated with Copper Oxide nanoparticles at concentration of 1.3 mg /ml. Cultures were kept for incubation at 28 ^{o}C and 180 rpm in orbital shaking incubator for 3 hrs. After incubation, 100 µl of the growth mixtures (bacteria + nanoparticle + media) were inoculated on solid NB agar (2 %) plates and kept at 37 ^{o}C for 12 hrs. Control plate contained only inoculum without nanoparticles. Bacterial growth was observed and numbers of colonies were counted.

2.3.2 Photocatalytic Activity

For analysis of photocatalytic activity of TiO_2 nanoparticles , the derived nanocolloids were synthesized via laser ablation at target-liquid interface for two laser focusing conditions, as listed in Table 2.22. The nanocolloids (concentration 0.5 mg/ml and 0.2 mg/ml) were then mixed to Methylene blue (.03 M). The mixed solution was

irradiated with an UV source with the help of a cylindrical lens (focal length 30 cm) for various duration as shown in figure 2.23. Its photo degradation under UV exposure was measured via UV-VIS (UV PC 3101) spectrum.

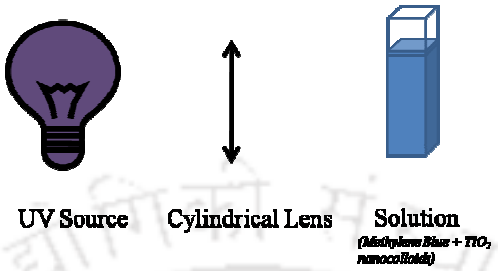

Figure 2.23 *UV irradiation on synthesized nanoparticles*

Table 2.3 *Experimental details for testing applicability of nanoparticles*

Application of Synthesized Nanoparticles				
Application	Target	Laser Energy mJ	Spot size on Target µm	Laser Fluence J/cm^2
Photocatalytic Activity	Titanium	4 (focus) 0.3 (below focus)	80 400	1.4 0.2
Antibacterial Activity	Copper	25	550	15

To conclude, in this chapter various diagnostics developed to study the laser induced breakdown in water and metal-water interface was described. LIB at metal-water interface was used to synthesize copper oxide and titanium oxide nanoparticles. Further for studying the photocatalytic activity and antibacterial properties of synthesized metal oxide nanoparticles the respective experimental set-ups were assimilated.

Chapter 3

3. Laser Induced Breakdown in Liquids

In the present chapter, the transient evolution of laser induced breakdown process in water is analyzed. The BDS technique discussed in chapter 2 is employed to study the transient evolution of the mechanical effects- shockwaves and cavitation bubbles produced during LIB in liquids. The shockwave and bubble velocities are also measured as a function of laser energy. In laser produced plasma there is a probability of formation of multiple bubbles. The multiple bubble interaction is studied via SG technique. The temporal evolution of laser produced charge carriers in water plasma is studied via EEP. In addition, the effect of laser energy on this transient conduction is also elucidated. The decay of transient conduction is attributed to heat transfer and the corresponding thermal diffusivities associated with it are estimated. The transient plasma emits its characteristic radiation. The spatial evolution of constituent species of laser induced water plasma is analyzed via LIBS.

3.1 Shockwave and Cavity Dynamics via Beam Deflection Set-up

Laser–induced plasma in liquid results in high pressure zone and emits shockwaves [12]. Following the laser pulse, plasma cooling results in the onset of cavitation bubbles [15]. All these physical phenomena result in the change in the local refractive index of the liquid. These mechanical effects can be studied using beam deflection set-up shown in figure 2.8 of section 2.1.1. The complete oscilloscope trace of the beam deflection signal for different laser energy is shown in figure 3.1. Possible candidates for the first negative narrow peak (inset a) could be high energetic plasma

electrons (in the vicinity of the focal spot) and shockwaves. On a larger time scale, plasma cooling results in cavitation bubbles containing water vapor, hydrogen and oxygen gas due to dissociation of water via LIB process [6, 81]. The cavitation bubbles undergo three stages: primary bubble collapse, rebound and higher order bubble formation.

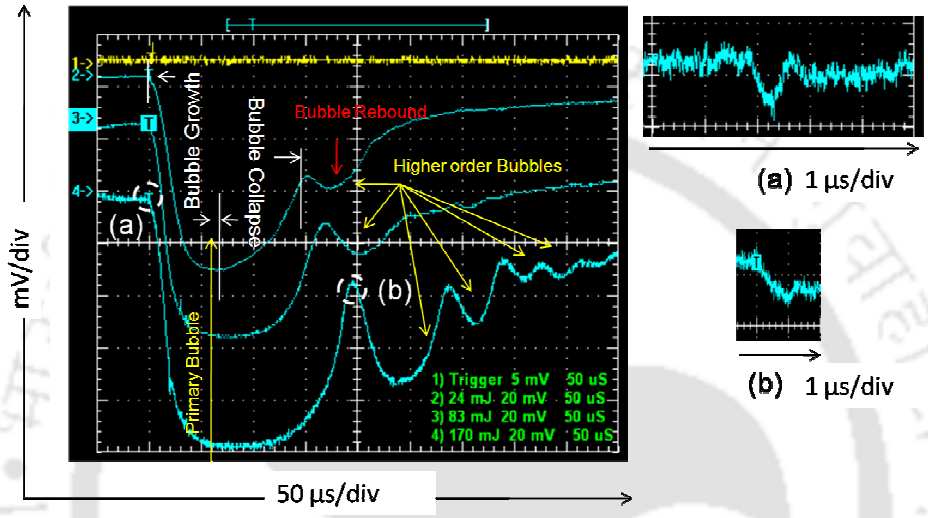

Figure 3.1 *Complete oscilloscope traces of the deflected He–Ne signal at -1 mm from the focal region at different laser energies. Inset: (a) charged particles and (b) shockwaves*

The first stage , first broad peak shown as primary bubble, figure 3.1, is the cavitation bubble growth phase in which the vaporized fluid mass inside the cavitation bubbles expands until all its kinetic energy is converted into potential energy to reach a state where the inside pressure becomes less than the hydrostatic pressure of the surrounding liquid. Due to the pressure gradient, the bubble collapses (e.g. Trace 2, figure 3.1) which leads to a state where pressure inside the bubble is more than the hydrostatic pressure. The increase in pressure inside the bubble than the surrounding liquid ascribes the second stage of bubble dynamics which leads to bubble rebound and formation of secondary bubbles. The process repeats and the bubble oscillates until all its energy is dissipated into the surrounding liquid. Each time the bubble

collapses, a shockwave is emitted which carries away the energy to the surrounding liquid. The emitted shockwave after the primary bubble collapse is shown on an expanded scale for the 170 mJ laser pulse energy in inset b of figure 3.1. The second broad dip at 170 mJ followed by the third and fourth dip is attributed to higher order cavitation bubble oscillations. Figures 3.2(a), 3.3(a), 3.4 (a) shows the spatial and temporal evolution of beam deflection signals (BDS) at 24 mJ, 83mJ and 170 mJ of laser energies respectively.

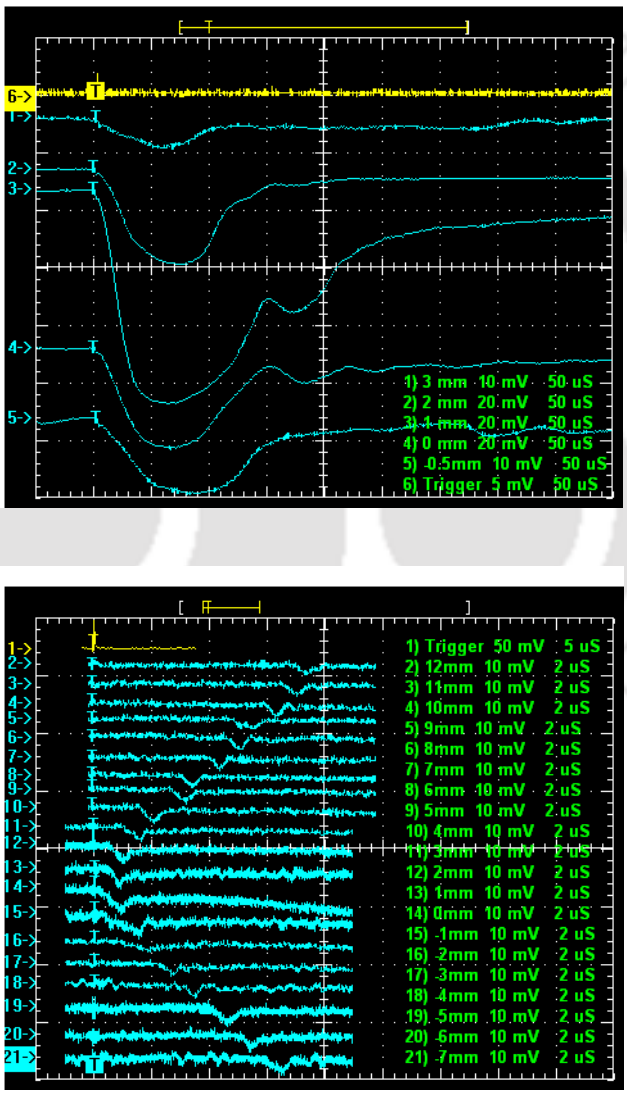

Figure 3.2 *Beam deflection traces of the probe He–Ne laser at 24 mJ for* ***(a)*** *cavitation bubbles* ***(b)*** *shockwaves*

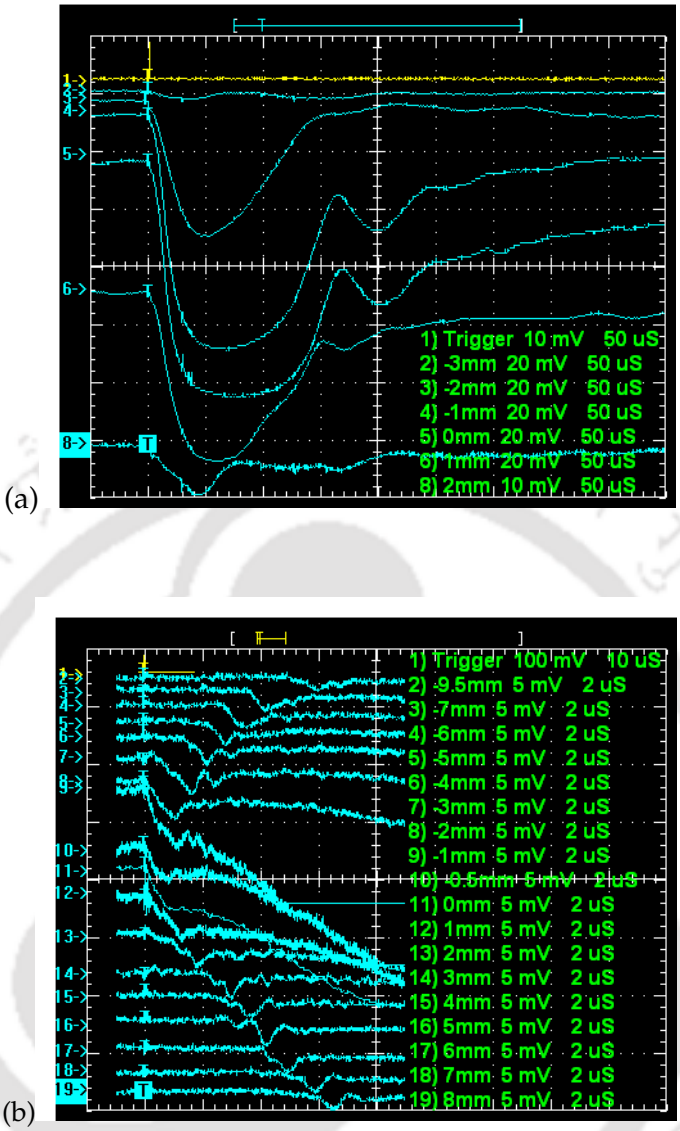

Figure 3.3 *Beam deflection traces of the probe He–Ne laser at 83 mJ for* ***(a)*** *cavitation bubbles* ***(b)*** *shockwaves*

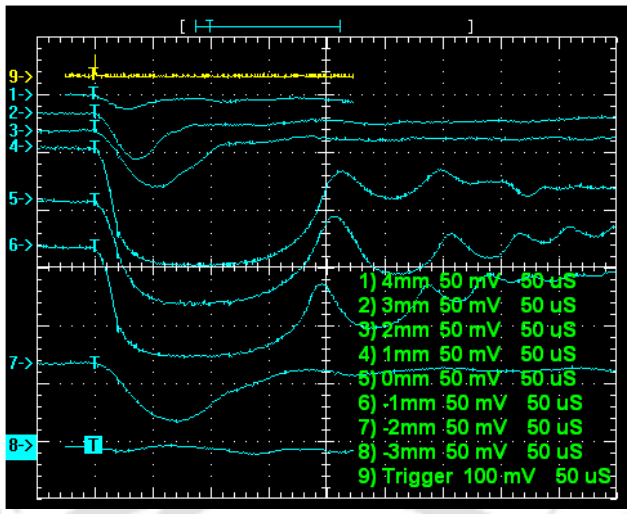

(a)

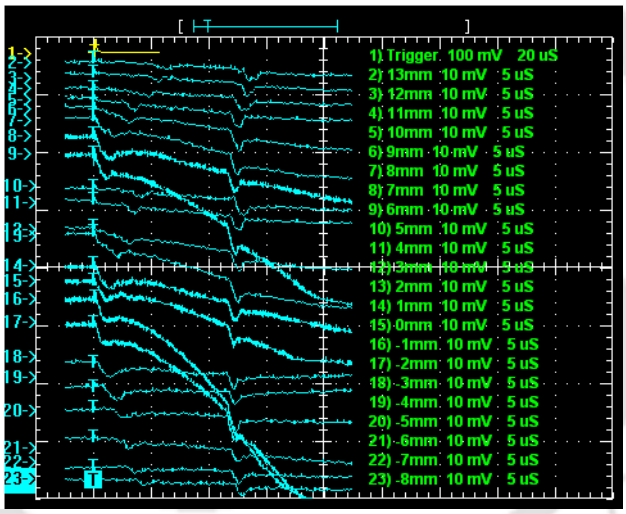

(b)

Figure 3.4 *Beam deflection traces of the probe He–Ne laser at170 mJ for* ***(a)*** *cavitation bubbles* ***(b)*** *shockwaves*

The duration of the first negative narrow peak in BDS is of the order of 1μs. Therefore the signals were recorded separately at the expanded scale as shown in figure 3.2 (b), 3.3(b), 3.4 (b) respectively. The laser energy plays a vital role in the shockwave and cavitation bubble dynamics. In the vicinity of the laser focal spot, the first negative deflection of the He Ne laser of figure 3.2(b), 3.3(b) and 3.4 (b) is

attributed to the combined effect of shockwaves and electrons/ions present in the plasma. The shock-compressed water may itself generate electrical conduction due to high pressure in the laser produced plasma at the vicinity of laser focus [82]. At larger distances, the charge particles are lost rapidly via loss mechanisms and the He–Ne beam is deflected primarily because of the shockwave which induces discontinuity in the refractive index of the water. At high energies (170 mJ), an interesting feature in the BDS signal was observed. In figure 3.4(b), the BDS traces show onset of a second narrow negative dip after the emission of shockwaves. This negative dip is ascribed to the acoustic emissions before the onset of cavitation bubbles [83]. The cavitation dynamics is vigorous at high energies and hence acoustic emissions due to cavitation are not observable at lower energies. The beam deflection traces were used to acquire the shockwave and cavitation bubble velocities as discussed in section 2.1.1. For cavitation bubbles, the bubble expansion velocities were recorded by measuring the relative delay (Δt) incurred in the dip of beam deflected signals by the bubble expansion at different distances in the region of breakdown as depicted in figure 3.5 (detail analysis given in figure 2.9).

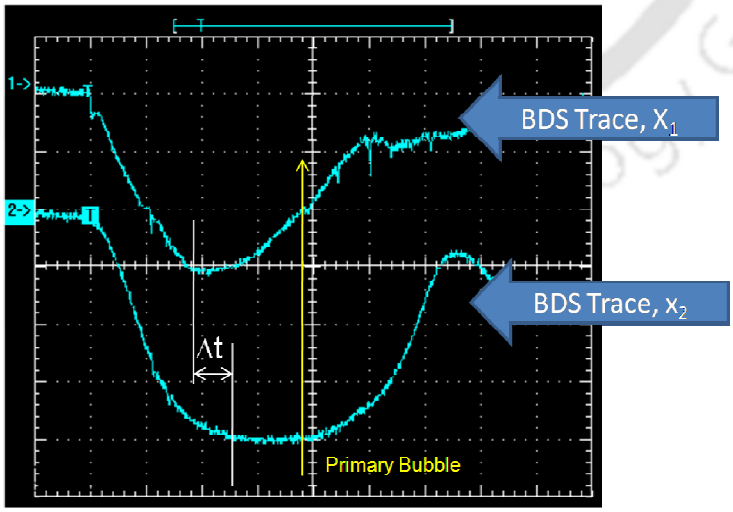

Figure 3.5 *Schematic for estimation of bubble expansion velocity*

The variation of shockwave velocity with distance is shown in figure 3.6. The maximum velocity of shockwaves near the focus was found to be 30 km/s for laser energy of 170 mJ. At a region away from the focus, electrons are lost due to recombination, diffusion and heat conduction. This results in cooling of plasma and a fluid dynamical process overtakes ionization, thereby reducing the velocities in the acoustic range of ~1.5 km/s beyond ~2 mm on either side of focus. The variation of the primary and secondary bubble expansion velocities as a function of the distance from the focus at different laser energies is shown in figure 3.7. For shockwaves and cavitation bubbles the backward velocity decays faster than the forward velocity because recoil momentum is more in the forward direction. The trend observed by cavitation bubbles is similar to that of the shockwaves, except that the velocities in this case are in the subsonic range. At the focus, the maximum primary and secondary cavitation bubble velocities were found to be ~ 900 m/s and ~600 m/s for laser energy of 170 mJ. The velocity for all the laser energies reduces on either side of the focus. As the energy carried away by the bubbles is smaller compared to that of shockwaves, its appearance is confined to a smaller extent on either side of the focus. The velocities of cavitation bubble for different values of laser energies are listed in table 3.1. As the laser-generated bubbles are not in equilibrium with the surrounding liquid, the bubble dissipates all its energy by undergoing large number of oscillations. With each oscillation the bubble attenuates by emitting vaporized material and a shockwave into the surrounding liquid. Subsequently higher order bubble velocities decrease. The velocities of cavitation bubbles increase with the increase in laser energy. Higher order cavitations bubble oscillations become more pronounced with higher energy, as third, fourth and even fifth–order bubble oscillations in the subsonic range were observed at 170 mJ , figure 3.1. This is because with the increase in the laser energy

the pressure gradient is high and the bubble becomes highly unstable. The oscillation of bubbles continues for longer duration in order to balance the pressure difference which becomes more rigorous in the case of higher energies.

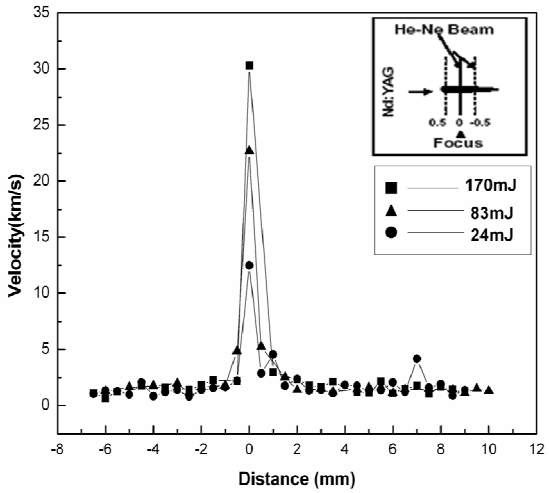

Figure 3.6 *Spatial variation of the shockwave velocity relative to the focal spot*

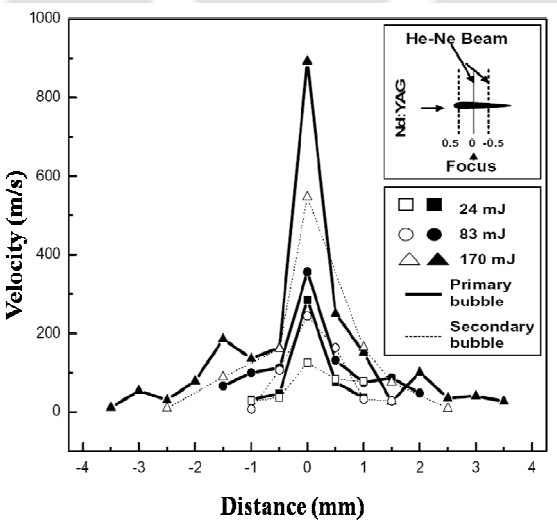

Figure 3.7 *Spatial variation of the cavitation bubble velocity relative to the focal spot*

Gilmore model was used to enumerate the cavitation bubble velocity fields, throughout the liquid for different laser energies where the conservation of

momentum and conservation of mass equation are given as follows [84]:

$$\frac{\partial}{\partial t}(-\nabla\varphi)+(\overline{u}\bullet\nabla)\overline{u}=-\frac{\nabla p}{\rho}+\frac{4\mu}{3\rho}\nabla(\nabla\bullet\overline{u}) \qquad (3.1)$$

$$\overline{u}=-\nabla\varphi \qquad (3.2)$$

$$\nabla\bullet\overline{u}=-\frac{1}{\rho}(\frac{\partial\rho}{\partial t}+u\frac{\partial\rho}{\partial r}) \qquad (3.3)$$

where $\overline{u}$ is the vector velocity, φ is the velocity potential, p is the pressure, ρ is the density and μ is the viscosity of the liquid.

The flow field in liquid can be described by the expression of spherical sound waves provided all velocities are small compared to the sonic velocity, c_∞ :

$$\varphi=\frac{1}{r}f(t-\frac{r}{c_\infty}) \qquad (3.4)$$

where r is the distance from the centre of the bubble. Under a spherically symmetric condition and by considering the above equations, the expression describing the dynamics of cavitation bubble motion is given by

$$RU\frac{dU}{dR}(1-\frac{U}{C})+\frac{3}{2}U^2(1-\frac{U}{3C})=H(1+\frac{U}{C})+\frac{RU}{C}\frac{dH}{dR}(1-\frac{U}{C}) \qquad (3.5)$$

where R, C, H, U correspond to the same parameters r, c, h_b, u (initially at liquids) at the bubble wall and h_b is the enthalpy difference [84] . It was observed that the bubble wall velocity U varies as $R^{-1/2}$ when solved analytically. In order to derive the relations of velocity fields throughout the liquid (under quasi-acoustic approximation), the radial velocity is found by combining equations (3.2) and (3.4):

$$u=\frac{f(t-\frac{r}{c_\infty})}{r^2}c+\frac{f'(t-\frac{r}{c_\infty})}{rc_\infty}. \qquad (3.6)$$

Equation (3.6) is solved in an explicit analytical way to get the equation of velocity

fields throughout the liquid:

$$u = U\left[\frac{R^2}{r^2} + \left(\frac{r^2 - R^2}{r^2}\right)\left(\frac{U^2}{2c_\infty^2} - \frac{P - p_\infty}{\rho c_\infty^2} - \frac{R}{2\rho\rho_\infty^2}\frac{dP}{dR}\right)\right]. \qquad (3.7)$$

However, the velocity field derived above is strictly confined to the subsonic range and hence fits to our experimental results of the primary bubble velocity. In order to estimate the size of the bubble, Rayleigh's model of cavitation bubble as given below was used [85]:

$$R_{max} = \frac{1}{0.915}\left(\frac{p - p_v}{\rho}\right)^{1/2} T_c \qquad (3.8)$$

(R_{max} is the maximum bubble radius and p_v is the vapour pressure of water). The collapse time T_c equals half of the duration of the time interval between generation and first collapse of the bubble as shown in figure 3.8.

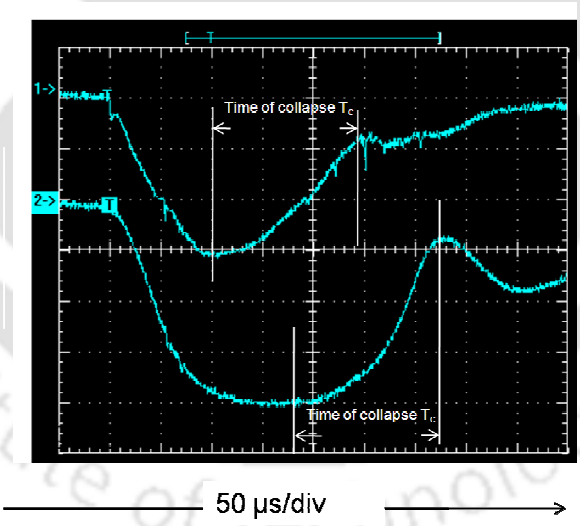

Figure 3.8 *Estimation of time of collapse*

Using equations (3.7) and (3.8) the theoretical values of the velocity fields were estimated. Since the contribution due to the first term in (3.7) is dominant, the rest of the terms were neglected. Figure 3.9, compares the plots of bubble flow velocities

from the Gilmore model discussed above and bubble expansion velocities obtained from the beam deflection set-up for different laser energies. The bubble flow velocity almost approximates the primary cavitation bubble expansion velocity but at the focus it breaks down as it has an asymptotic nature with $1/r^2$ dependence.

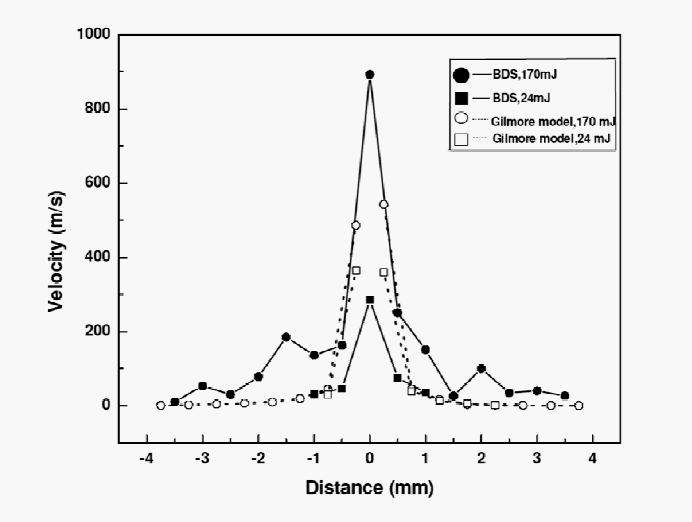

Figure 3.9 *Comparison of bubble flow velocity and bubble expansion velocity*

Table 3.1 *Cavitation bubble velocities at the focus and bubble confinement distances*

Energy (mJ)	Primary bubble velocity (m/s)	Secondary bubble velocity (m/s)	Third-order bubble velocity (m/s)	Fourth-order bubble velocity (m/s)	Fifth-order bubble velocity (m/s)	Primary bubble confinement (mm)	Secondary bubble confine-ment (mm)
170	892	546	90	30	10	7	5
83	356	244				5	2.5
24	285	124				3.5	2

3.2 Multiple Bubble Interaction via Shadowgraphic Technique

The study of cavitation bubbles during LIB of water is highly complex. The laser-produced bubble is not only confined to the focus but also extends up to the Rayleigh length of the source laser. There is formation of multiple bubbles along the direction of propagation of the laser beam within the Rayleigh length (section 1.1, chapter 1). The formation of closely spaced bubbles results in bubble–bubble interaction at larger time scales. The hydrodynamics of multiple bubble interaction is studied via shadowgraphic technique shown in figure 2.10 in section 2.1.2.

Figure 3.10 shows the geometry for capturing the bubble images. The He-Ne laser is illuminated along x direction and the source Nd:YAG laser is incident along y direction. The active area of CCD is in y-z plane and hence the cavitation bubble images in the y-z plane are recorded. The scan area of CCD is 8.6 mm X 6.9 mm and the Rayleigh length (R_L) for the Nd:YAG laser with the focusing lens of 5 cm is ~3 mm. The observed cluster of closely spaced bubbles along the direction of incident laser for different time interval w.r.t the Nd:YAG laser pulse are shown in figure 3.11.

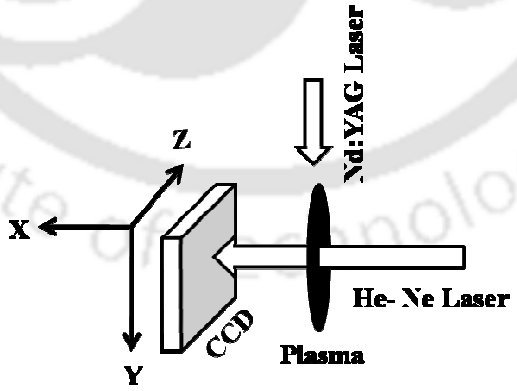

Figure 3.10 *Schematic for image plane recorded by CCD*

The approximated focus of the source laser is shown by arrow mark in Figure 3.11 (c)

at a delay of 50 µs w.r.t. laser pulse around the region of formation of B_2 and B_3. The image in figure 3.11(a) show formation of seven bubbles (B_1, B_2----B_7) numbered sequentially at a delay of 12.5µs after the laser pulse. When large no. of closely spaced bubbles are formed multiple bubble interaction becomes evident. At 30 µs, figure 3.11(b), the bubbles continue to expand and bubbles B_4 – B_5 and B_6-B_7 coalesce to B_{45} and B_{67} respectively. B_6-B_7 coalesces in-phase which involves merging of similar bubbles. When the two bubble surfaces are very close to each other, the bubbles coalesces or rebound depending upon the acting molecular and surface forces, and flow of the surrounding liquid. The liquid in the interfacial zone of two approaching bubbles flows out radially and gives an upward thrust to the trailing bubble .The remnant liquid at the interface gets trapped and compressed, and Van der Waal's forces become effective [86]. At this point a hole is formed at the rim of the bubbles and surface tension results in hole expansion and hence the two bubbles merges into one. The approaching bubbles may also bounce back if the merging bubbles introduce large distortion and enhance the surface energy during the coalescence period. The images recorded at 50 µs show collapse of B_1 and B_{67} and in phase coalescence of B_2 – B_3 to B_{23} at the approximated focus. The expansion at focus is maximum and on either side smaller bubbles are observed; therefore the out-of-phase coalesces between dissimilar bubbles becomes more probable. The CCD images taken at 60 µs show the out-of-phase coalescence between B_1 and B_{23}. B_1 strongly influences the collapse of B_{23} in addition to the pressure gradient of surrounding liquid which normally initiates the collapse phase. The out of phase bubble coalesce is accompanied with jet formation [20]. The jet pierces bubble at the focus and influences its violent collapse as depicted in figure 3.11(e) at 70 µs. It is apparent from the bubble images that the bubble moves collectively towards the

direction of incident laser. When the laser is focused inside water, laser assisted bubble replaces fluid at the vicinity of the focus and the vapor bubble propagates in the forward as well as backward front from the focus. On larger time scales the effect of source term vanishes, the fluid mechanical phenomenon overtakes and the displaced fluid exerts an upward thrust to the vapor bubbles and forces it to move towards the direction of incident laser.

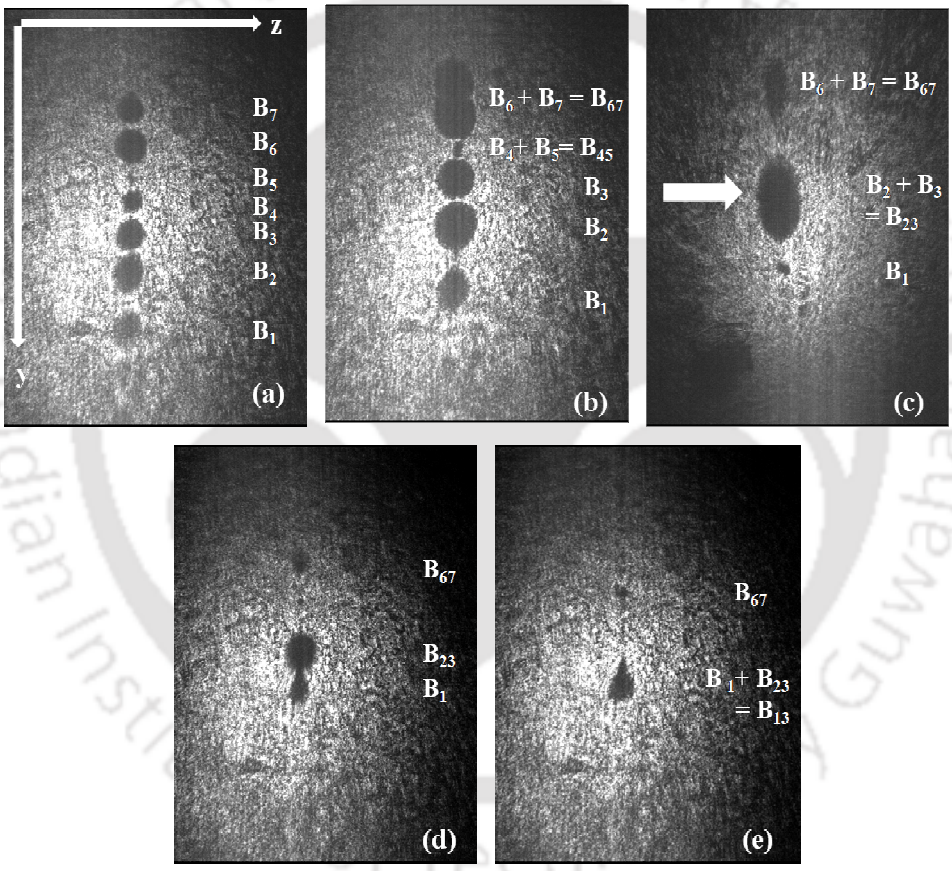

Figure 3.11 *Cavitation Bubbles Images via shadowgraphy at delay of (a) 12.5 µs (b) 30 µs (c) 50 µs (d) 60 µs (e) 70 µs w.r.t the laser pulse (arrow mark shows the approximated focal spot).*

In the laser induced cavitation, fluctuation of multiple bubble coalescences makes the study of cavitation bubble highly asymmetric and complex. In some cases, three bubble coalesces were also observed as shown in Figure 3.12. The general trend of

bubbles expansion and collapse was reproducible but some fluctuations due to shot to shot variation were observed. Hence CCD images for every data point were averaged over 40 shots. The spatial evolution of bubble radius across the focal volume at different interval of time is shown in Figure 3.13.

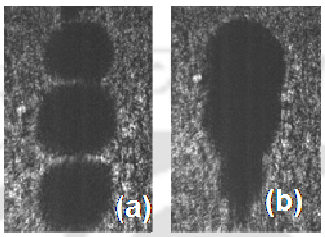

Figure 3.12 *Multiple Bubble Interaction; Bubble coalescence at a delay of (a) 20 µs and (b) 40 µs*

The location of forward and backward front of the cavitation bubbles with respect to the focus is marked as 3 mm as shown in figure 3.13(a). Hence the distance 3 mm to 6 mm is the forward front and 1 mm to 3 mm is the backward front for the cavitation bubbles. Figure 3.13(b) and 3.13(c) shows the radius and hence the growth and collapsing phase of cavitation bubbles across the focal volume. During the growing phase of bubbles as shown in figure 3.13 (b) , the expansion of bubble radius in the focal region continues till 50 µs and persists upto a distance of 2 mm w.r.t. the focus (3-5 mm) along the direction of incident laser. The calculated Rayleigh length (R_L) is 3 mm so the intensity is high enough for perseverance of maximum bubble expansion upto 2 mm distance from the focus. Beyond these regions, at the backward (positions < 3 mm) and forward front (positions > 5 mm), relatively smaller bubbles are formed which decays after 30 µs. This is due to the energy gradient inducted by the Nd: YAG laser which decays with distance from the focus. The formation of larger bubbles beyond the focal spot shown by an arrow mark is due to coalesce of smaller bubbles into larger bubbles. The collapse phase of cavitation bubbles , figure 3.13 (c) shows

slight increase in radius at 70 µs in the backward front (distance < 2.5 mm) and forward front (4.5 mm) which is probably due to the formation of secondary bubbles. It is apparent from Figure 3.13 that the spatial evolution of cavitation bubbles across the focal volume shows a damped oscillatory behavior.

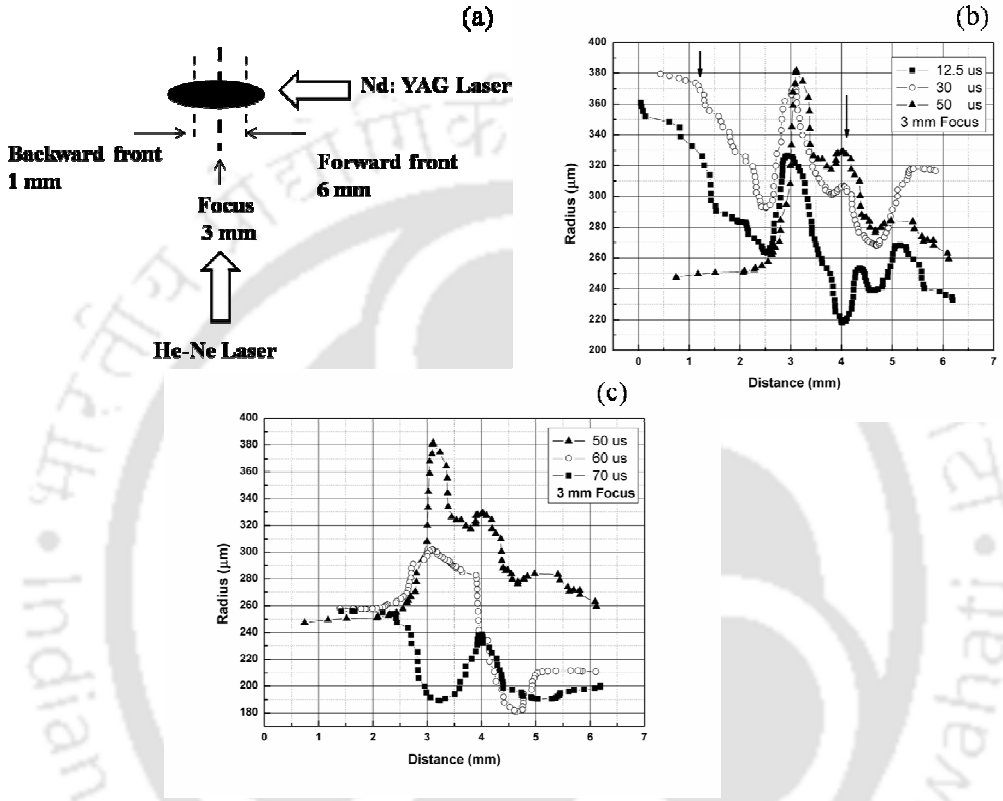

Figure 3.13 (a) *Schematic showing the forward and backward front of plasma w.r.t focus. (3mm – focus, 1- 3 mm backward front, 3 - 6 mm forward front).**(b)** Radius of cavitation bubbles after; 12.5 µs, 30 µs and 50 µs of the laser pulse.**(c)** Radius of cavitation bubbles across focal volume after; 50 µs, 60 µs and 70 µs of the laser pulse*

These results are also complemented by BDS traces at different distance from the focal region as shown in Figure 3.14. The details of the BDS trace is given in section 2.1.1. Traces 1 & 2 in the figure 3.14 corresponds to the Nd:YAG laser trigger signal and beam deflectiom signal respectively. Figure 3.14(a)&(b) represents the backward front, Figure 3.14(c) corresponds to the focal region and Figure 3.14(d)-(f) belongs to

the forward front from the focus.

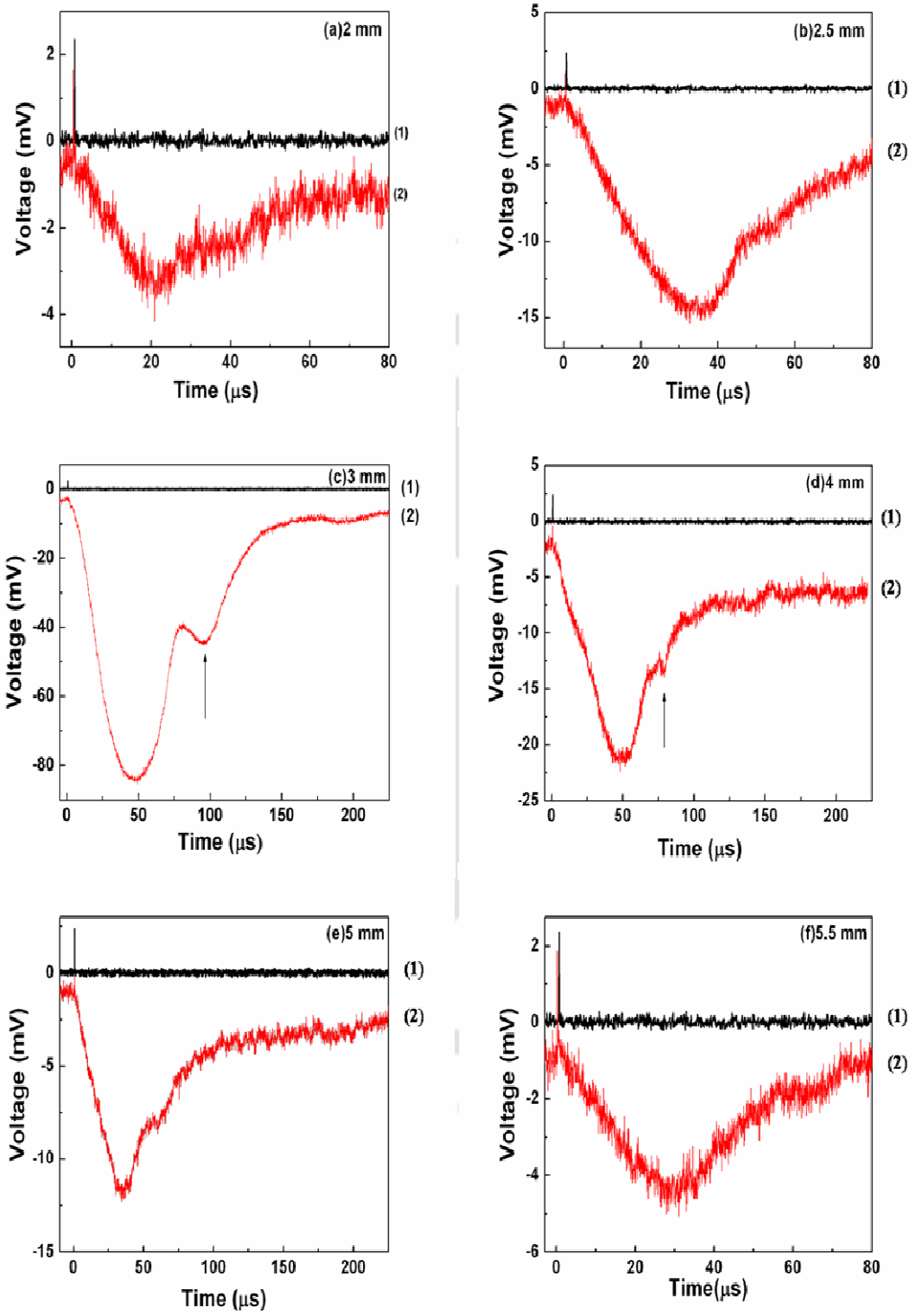

Figure 3.14 *Beam Deflection Traces across focal volume. Arrow mark shows the onset point for secondary bubbles. (- Trigger signal, - Beam Deflected Signal)*

The maximum dip of 80 mV in photodiode signal is observed at the focus (figure 3.14 (c)) which decreases gradually on either side of the focus. The first dip in the BDS Traces represents the primary bubble and the second dip represents the secondary bubble. The arrow mark in the traces show bubble rebound after the primary bubble collapse. Since the smaller bubble collapses earlier, onset of secondary bubbles is faster at distances away from the focus. The bubble rebound at focus starts at ~90 µs whereas at defocused condition, the earliest onset is at ~55µs at a distance of 0.5 mm from the focus at the backward front.

For further confirmation of damped oscillatory behavior of bubble formation across the focal volume, Rayleigh's model for an empty cavity and Khoroshev's model for a gas filled transient cavity is used to analyze the spatial variation in bubble radius in the forward as well as backward front relative to the focal spot [85,87]. Rayleigh's model , equation (3.9) for empty cavity and Khoroshev's model, equation (3.10) is given below for gas filled cavity which involves estimation of maximum bubble radius from the time of collapse of cavitation bubbles.

$$T_c \approx 0.915 R_{max} \left(\frac{\rho}{P_0} \right)^{1/2} \qquad (3.9)$$

$$T_c \approx 0.915 R_{max} \left(\frac{\rho}{P_m} \right)^{1/2} \left(1 + \frac{Q}{P_m} \right) \qquad (3.10)$$

Where T_c is the bubble collapse time and R_{max} is the corresponding maximum bubble radius. ρ is the density of water and P_0 is the hydrostatic pressure. Q is the pressure inside the bubble at maximum radius R_{max} and P_m is the ambient pressure which is assumed to be constant over the collapse period. P_m varies with the distance from focal spot of the laser. For simplicity the effect of surface tension and viscosity is not considered.

The time of collapse T_c was measured from the BDS traces of figure 3.14. The

duration between the maximum deflection of first negative peak of primary bubble (start of collapse) and the onset point of second negative dip (secondary bubble) of the BDS traces is taken as the collapse time as illustrated in figure 3.8. P_m and Q are estimated using Neppiras model for gas filled transient cavity.

The motion of a bubble wall undergoing adiabatic compression is given by Neppiras [88]:

$$R\ddot{R} + \frac{3}{2}\dot{R}^2 = \frac{1}{\rho}\left[Q\left(\frac{R_{max}}{R}\right)^{3\gamma} - P_m\right] \qquad (3.11)$$

$\dot{R}, \ddot{R}$ is the bubble wall velocity and acceleration respectively and γ is the ratio of specific heat for gas (γ is taken as 4/3). The minimum radius R_{min} reached by collapsing cavity and the corresponding maximum collapse speed are given by equations (3.12) and (3.13) respectively.

$$\frac{R_{min}}{R_{max}} \approx \left[\frac{Q}{P_m(\gamma - 1)}\right]^{1/3(\gamma-1)} \qquad (3.12)$$

$$\dot{R}^2_{max} \approx \frac{2[P_m(\gamma - 1)]}{3\rho\gamma}\left[\frac{P_m(\gamma - 1)}{Q\gamma}\right]^{1/(\gamma-1)} \qquad (3.13)$$

The maximum bubble velocity (measured from change in bubble radius at different instants of time) and minimum and maximum bubble radii are taken from shadowgraphic results (figure 3.13). The maximum and minimum bubble radius at the focal spot is found to be 380 µm and 190 µm respectively. Using equations (3.12) and (3.13) the values for P_m and Q are estimated. Figure 3.15 shows the maximum bubble radius variation across the focal volume measured using shadowgraphy and that of estimated from Rayleigh's and Khoroshev's model**.** It is apparent from figure 3.15 that the bubble radius w.r.t. focus undergoes an oscillatory behavior. The radius measured via shadowgraphy is slightly larger in size than that of estimated from

Khoroshev's and Rayleigh's model. The incident laser energy is maximum at the focus and decays radially on either side of the focus. The increase in bubble radius at focus is obvious due the maximum deposition of laser energy however on either side of focus increase in bubble radius is ascribed to bubble coalescences.

For laser generated bubbles, the cavity is not empty, it is filled with vaporized and gaseous species of water molecules and the bubbles collapse adiabatically into the surrounding liquid. Neppiras model for adiabatic compression for gas filled cavity is used to estimate maximum pressure inside the gas bubble during its collapse phase.

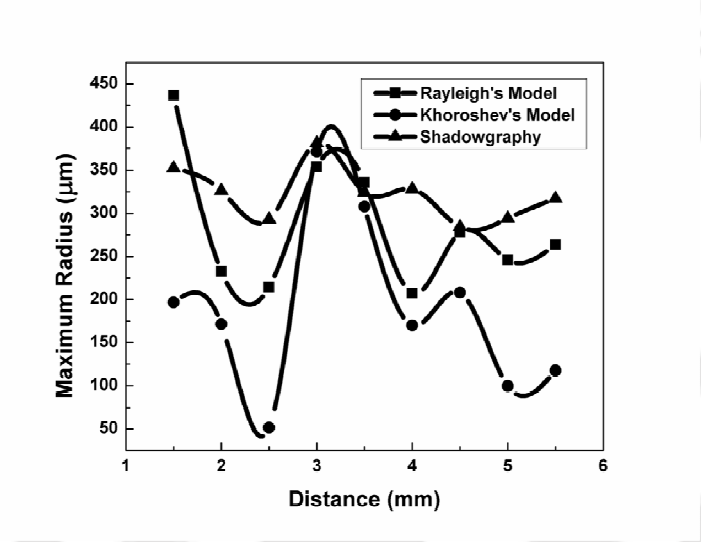

Figure 3.15 *Variation of Maximum Bubble Radius across focal volume*

For adiabatic compression, maximum pressure P_{max} reached by the gas is given by

$$P_{max} \approx Q\left[\frac{P_m(\gamma-1)}{Q}\right]^{\gamma/(\gamma-1)} \qquad (3.14)$$

Using this equation, the maximum pressure attained by the gases inside the cavity is estimated. To measure liquid pressure at highest compression approximately, Rayleigh's model for empty single cavity is used (equation 3.15).

$$P_{max} = \left(\frac{P_0}{4^{4/3}} \right) Z \qquad ; Z = \left(\frac{R_m}{R} \right)^3 \qquad (3.15)$$

Figure 3.16 shows the maximum gas pressure, liquid pressure and bubble wall velocity after 70 μs of the laser pulse as a function of distance from the focus. The calculated maximum gas pressure is 0.4 MPa and the maximum liquid pressure is 0.1 MPa. Pressures and the collapse velocity of bubbles are maximum at the focus and fall down on either side of it.

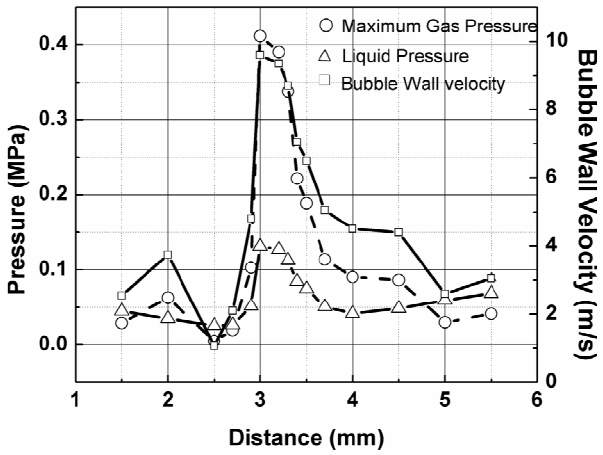

Figure 3.16 *The variation in maximum pressure gained by the gases inside the bubble, liquid compression pressure and bubble wall velocity across the focal volume after 70 μs of the laser pulse*

3.3 Transient Evolution of Plasma Charge Carriers via External Electric Probe

In laser–induced breakdown, the loss mechanisms in plasma are heat conduction, diffusion and recombination. In ns laser–induced plasma, the dominant mechanism behind energy dissipation is heat conduction. To understand the thermo-physical properties of laser–induced water plasma, the transient evolution of plasma charge carriers is studied. The flow of plasma charge carriers constitutes a transient current which can be modeled using the heat transfer equation to estimate thermal diffusivity.

The schematic of experimental set-up to study the transient conduction via electrical probes across the laser induced water plasma is depicted in section 2.1.3. The formation of localized plasma in liquid induced by pulsed high power laser leads to electrical perturbation in the focal region. Application of electric field transverse to the direction of propagation of laser beam results into the transverse current due to the flow of charge carriers. Figure 3.17 shows the transient current for an applied voltage of -10V at electrode A for incident laser energies of 24 mJ, 83 mJ and 170 mJ. The possible candidates for the source of transient current are highly energetic electrons. The recorded signal has "optogalvanic" like behavior and the onset of current is attributed to the electrical conduction accompanied by the exuberant shockwaves emanating during the water breakdown process [82, 89]. The maximum of excess charge carriers produced by laser induced plasma is received at the electrode at a delay of ~250 ns after the laser pulse as shown in the inset of figure 3.17. The background noise associated with the circuit has been filtered out for recording the time of flight of electrons to the electrodes. The velocities associated with charged particles are then found to be ~5 km/s. This is compatible to the charged particle velocities for laser induced plasma in water in the vicinity of focus (section 3.1). Further, with increase in laser energy the peak electron current within the laser pulse increases as ionization gets enhanced and it persists for larger duration after the laser pulse. Hence the area under the curve gets broadened for higher energies. The exponential decay time of the transient current at 24 mJ, 83 mJ and 170 mJ are found to be (1.2±.01) μs, (1.25±.01) μs and (1.32±.01) μs respectively. The persistence of the conduction for longer duration (~ 1.5 μs) after the laser pulse is rather intriguing as for laser induced breakdown in liquids the plasma persists for <1000 ns and the typical recombination time is found to be an order of magnitude less [90,91]. The

long range conduction is ascribed to excess conduction due to electrolysis of water (tap water) during laser induced breakdown process. The effect of electrolysis is evident as during laser induced breakdown of distilled deionized water (conductivity < $1\mu\Omega^{-1}$) such transient conduction was not observed.

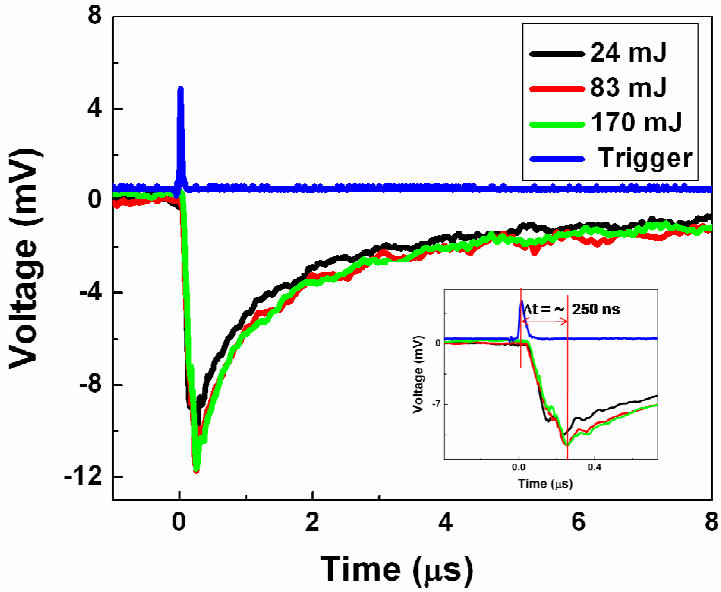

Figure 3.17 *Transient evolution of electron current with laser energy.*

To gain an insight onto the physical implications of the transient electrical conduction we assume the criteria for local thermodynamic equilibrium (LTE) in the laser produced water plasma are satisfied. For high density laser produced plasma, frequent collisions between electrons, electrons and ions produces equilibrium and collisional processes are dominant compared to the radiative processes. The assumption of LTE is also valid during shockwave emission because the detection domain for recording the charge carriers (~1.5 μs) is long compared to the shockwave wave assisted phenomena during laser induced breakdown in water (~ 10 ps) [92,93]. Under LTE, the electron density n_e can be expressed as [94-96]

$$n_e \approx \sqrt{T} \qquad (3.16)$$

Where T, represents the electron temperature during the breakdown process. The velocity of charged particles then follows the Maxwell-Boltzmann distribution. The thermal velocity, v can be expresses as $\sqrt{T}$. The application of external dc voltage induces a drift velocity which under steady state is saturated to a value similar to thermal velocity [97]. The transient electrical conduction I_{dif}, given by

$$I_{dif} = n_e A v q \qquad (3.17)$$

then can be expressed as,

$$I_{dif} \approx T \qquad (3.18)$$

where, q is the charge and A is the area under consideration. The functional form of the transient temperature at a distance r at an instant t for laser induced water plasma is taken as

$$T(r,t) = \frac{a}{(t)^{3/2}} exp\left(\frac{-b}{t}\right) \; ; a = \frac{c}{(8\pi\chi)^{3/2}}, b = \frac{r^2}{4\chi} \qquad (3.19)$$

where, a, b and c are constants and χ is the thermal diffusivity. The above expression is analogues to the dissipation of thermal conduction in a point heat source (ns laser induced plasma) concentrated at the focal spot (origin) for laser induced breakdown in liquids [98].

The distance "r" between the focal spot and collector plate is 1.5 mm. The experimentally observed transient current was fitted to (3.19). Figure 3.18 shows the fitted equation (3.19) onto the observed data points for negative charge carriers for different laser energies.

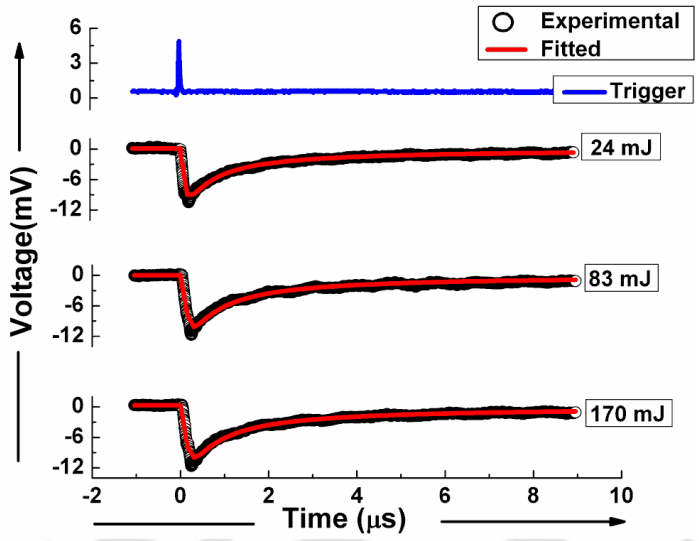

Figure 3.18 *Fitting onto the electron current distribution for various laser energies*

The calculated parameter "b" and the corresponding thermal diffusivity are tabulated in table 3.2 at different laser energies. The estimated χ is the time integrated thermal diffusivity. It is inferred from table 3.2 that increase in laser energy reduces the thermal diffusivity. This is because higher laser energy provokes more electron sites which activate more scattering centers resulting in decrease in electron mean free path and hence thermal diffusivity.

Table 3.2 *Estimation of Thermal diffusivity*

Laser Energy (mJ)	Fitted Parameters	Thermal diffusivity (χ) (m^2/s)
24	$b = (2.62 \pm .01)E-7$	$\chi = 2.2$
83	$b = (2.99 \pm .01)E-7$	$\chi = 1.9$
170	$b = (3.07 \pm .01)E-7$	$\chi = 1.8$

3.4 Laser Induced Breakdown Spectroscopy in Water

The laser–induced plasma emits the characteristic optical radiation of the corresponding excited molecular, ionic and atomic species. The collection, detection and characterization of these optical emissions are termed as laser induced breakdown spectroscopy (LIBS). LIBS is a very sensitive and potential tool for detection of constituent species of laser induced plasma of material under study [46-52]. The schematic of experimental set-up for recording LIBS is illustrated in figure 2.14 of section 2.1.4.

The observed LIBS spectrum, figure 3.19 (a), in the spectral region 230-250 nm in laser induced breakdown of water is due to hydrogen bonded OH radical. B band of molecular oxygen $b^1\Sigma_g^+(\nu'=1) \rightarrow X^3\Sigma_g^-(\nu'' = 0)$ due to electronic transition (686-688 nm) and vibrational overtones of 4ν polyads of water vapour (695-705 nm) are also observed as shown in figure 3.19(b) [99-101].

The laser induced breakdown (LIB) and resulting plasma formation leads to excitation, ionization and dissociation of water molecules. The chemical kinetics within plasma which led to the plasma emissions of various molecular species are shown in figure 3.19 can be given by the following reactions [102].

$$H_2O \rightarrow H^+ + OH^* \quad (3.20)$$

$$H_2O \rightarrow \frac{1}{2}H_2O_2 + \frac{1}{2}H_2 \quad (3.21)$$

$$OH^* + H_2O_2 \rightarrow H_2O + HO_2^* \quad (3.22)$$

$$OH^* + OH^* \rightarrow H_2O + \frac{1}{2}O_2 \quad (3.23)$$

$$2HO_2^* \rightarrow H_2O_2 + O_2 \quad (3.24)$$

$$HO_2^* + OH^* \rightarrow H_2O + O_2 \quad (3.25)$$

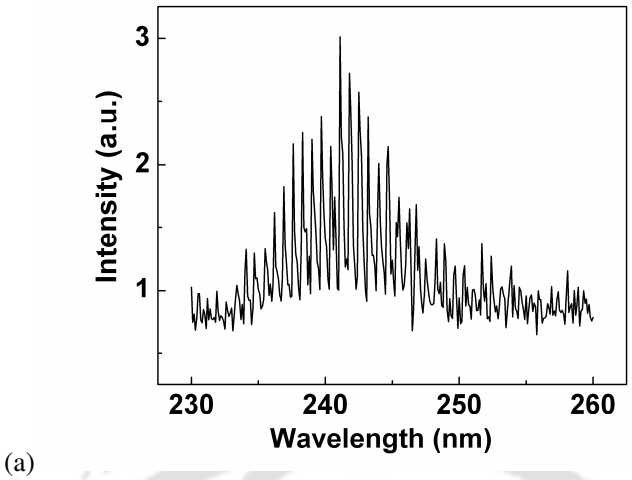

(a)

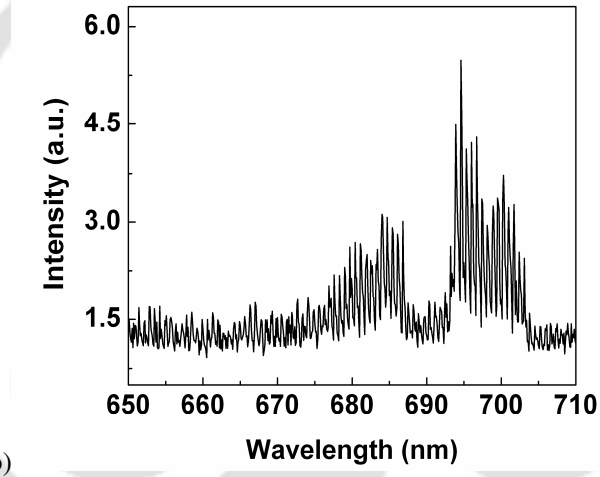

(b)

Figure 3.19 *Band spectra of* ***(a)*** *hydrogen bonded OH radical at 240 nm,* ***(b)*** *Molecular oxygen (686-688) nm and water vapour (695-705 nm)*

When the laser intensity is high and above the threshold energy for water breakdown, optical breakdown not only takes place at the focus but extends to the Rayeligh length of the incident beam on either side of the focus. The formation of plasma is observed visually in the form of an elongated spark of length ~ 5mm at 24 mJ laser energy as shown in figure 2.2. Figure 3.20 shows the band spectra of molecular oxygen, water vapour and hydroxyl peroxide radical for different region of plasma; forward front, focal region and backward front as shown in figure 3.20(a), 3.20(b) and 3.20(c)

respectively. The details of imaging is discussed in section 2.1.4. The recorded band spectra of figure 3.20(a) in the forward front indicates presence of vibrational overtones of excited HO_2* species. Its emission band is centered at 670 nm [103].

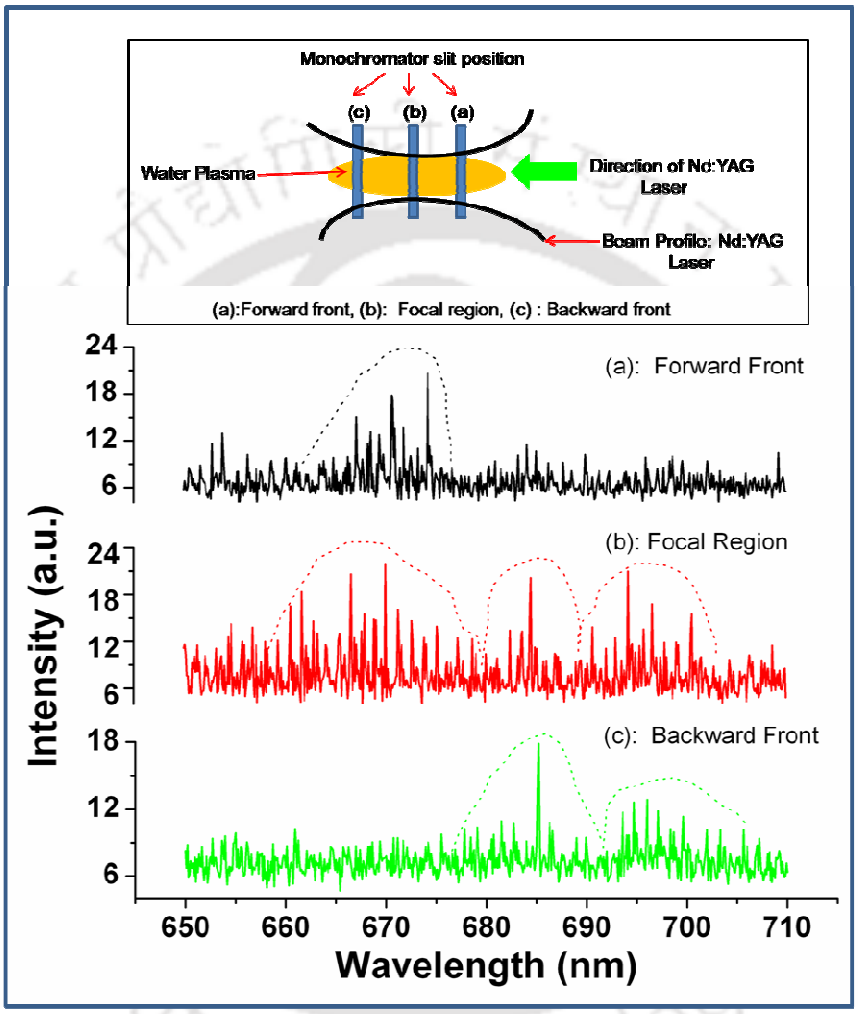

Figure 3.20 *Band spectra of water vapor, molecular oxygen and hydroxyl peroxide radical at* ***(a)*** *forward front of plasma* ***(b)*** *focal region* ***(c)*** *backward front of plasma.*

The initial plasma formed due to laser induced breakdown, absorbs the incoming laser energy and achieves high pressure and temperature thereby ionizing the surrounding liquid layer. This is mainly dominated in the forward front of plasma. The new layer of plasma further absorbs the incoming laser energy and obstructs it from reaching

regions beyond the focal volume. The rapid expansion of plasma leaves a rarefied region in the focal volume, which results in plasma cooling and favours recombination processes leading to formation of molecular oxygen at and beyond focal volume. Traces of molecular oxygen (686-688 nm) and water vapours (695-705 nm) are observed in figure 3.20(b) and figure 3.20(c). The excited hydroxyl radical, HO_2^* are formed in a three step process (reaction (3.20), (3.21) and (3.22)) and requires higher energy so HO_2^* species are confined to focal and the forward front of plasma whereas oxygen and water vapor bands are prominent in the backward front.

In summary, the spatial and temporal evolution of the shockwave and cavity dynamics was recorded for different laser energies using BDS. The shockwave propagates at supersonic speed in the range of 10^4 m/s where as the cavitation bubbles traverses at much lower speed (10^2 m/s) in the subsonic range. The laser induced plasma produces multiple bubbles whose interaction was studied by employing the SG technique. The bubble-bubble interaction led to bubble coalescence. This induced a damped oscillatory behavior to its spatial evolution of radius across the focal volume. The maximum pressures induced by these bubbles were found to be 0.4 MPa. In addition EEP is assembled to measure the time integrated thermal diffusivity in laser induced water plasma. It is found to be 1.8 m/s^2, 1.9 m/s^2 and 2.2 m/s^2 for laser energy of 170 mJ, 83 mJ and 24 mJ respectively. The decrease in diffusivity with increase in laser energy is associated to activation of scattering centers for laser produced charge carriers. LIBS spectra of water showed the formation of Hydrogen bonded OH radical (250 nm), B band of O_2 (686 nm) and vibrational overtones of H_2O (695 nm). In addition, Hydrogen peroxide HO_2*(670 nm) was observed only in the close proximity of focal point of the laser. The atomic emissions during LIB of

water were not observed. This is due to the confinement of plasma by surrounding liquids. The confinement effect induces the shortened lifetime of excited species which gets fused with bremmstrahlung emissions. The very existence of inelastic collision further reduces the signal intensity. Hence the separation of the LIB signal of atomic lines from continuous background (arising due to bremmstrahlung processes) becomes very difficult in the early plasma. The molecular species are formed relatively at the later stages hence were detectable.

Chapter 4

4. Laser Induced Breakdown at Target-liquid Interface

In the present chapter, the LIB process at solid-liquid interface is investigated. The experiment was conducted by focusing the Nd:YAG laser at Titanium target immersed in water. The BDS and LIBS technique discussed in chapter 2 were employed to estimate the high pressure high temperature (HPHT) conditions prevailing at the Titanium-Water interface. BDS is used to estimate the shockwave velocity which is applied to enumerate the pressure at the interfacial region. LIBS was employed at Titanium-water interface to detect the emission spectra of constituent species formed during the breakdown process. The emitted spectrum from laser induced titanium-water plasma was used to measure the rotational temperatures of various molecular species detected at the interfacial region. In addition, the focusing conditions during the LIB process were varied at Titanium target and its impact onto the physical processes occurring at the Titanium-water interface is elucidated. It has been documented in literature that LIB at Titanium-Water interface leads to formation of TiO_2 nanoparticles [24]. Hence, the estimated pressure and temperature at the interface is applied to unfold the nucleation process of TiO_2 nanoparticles and enumerate the nucleation time, growth velocity and size of TiO_2 nanoparticles [24]. It is observed that at low laser fluence, the nanoparticle size decreases and with narrow particle distribution [26, 77]. Hence all the diagnostics and synthesis of nanoparticles (*chapter 5*) at Titanium-water interface is carried with low power laser of energy ~4 mJ per pulse.

4.1 Estimation of Pressure at Titanium-Water Interface using BDS

The schematic of BDS at target-water interface is discussed in section 2.2.1. The BDS set-up at Titanium-Water interface was acquired for various focusing conditions (A, B, and C) shown in figure 4.1 and discussed in detail in section 2.2. The spatial profiles of BDS traces for each focusing condition were recorded at different distances relative to the target-liquid interface. The target-liquid interface is marked as 0 mm and the rest of positions of the BDS traces were with respect to the target-liquid interface. The complete beam deflection traces for laser focused condition (B, figure 4.1) at 0mm from the target-water interface is shown in figure 4.2. Trace 1 is the Nd:YAG trigger signal for reference. Trace 2 represents the complete beam deflection trace within the proximity of focus. The duration of first narrow negative peak is of the order of one microsecond and its deflected signal (~ 2 mV) is less compared to that of the cavitation bubbles (~ 50 mV). Therefore the signals were recorded separately at an expanded scale of 1µs/div as depicted in trace 3. Possible candidates for the first negative narrow peak (expanded in Trace 3) could be due to high energetic ions, electrons in plasma and as well as due to the shockwaves. For low energy of laser, the electrons are limited to the interfacial region due to the electron-ion recombination occurring immediately after the generation of the plasma [13]. With the passage of time, it is the shockwave that expands beyond the interfacial region. The other discontinuities (visible in Trace 3) are ascribed to the acoustic emissions due to the onset of cavitation bubbles [83, 104]. The broad dip (~150 µs) in the Trace 2, followed by the subsequent negative dips are attributed to primary, secondary and third order cavitation bubble oscillations respectively.

The complete BDS trace for above focus (A, figure 4.1) and focus condition (B, figure 4.1) at 0mm from the target-liquid interface is illustrated in figure 4.3 for

comparison. At focused condition (B, figure 4.1), maximum energy is deposited and hot plasma is formed. As a consequence, cavitation effects are more vigorous (Trace 2, figure 4.3) and higher order bubble oscillations are also pronounced. In contrast, for above focus (A, figure 4.1) condition (Trace 3, figure 4.3) weaker bubbles are formed with no obsevable secondary bubbles due to low laser intensity.

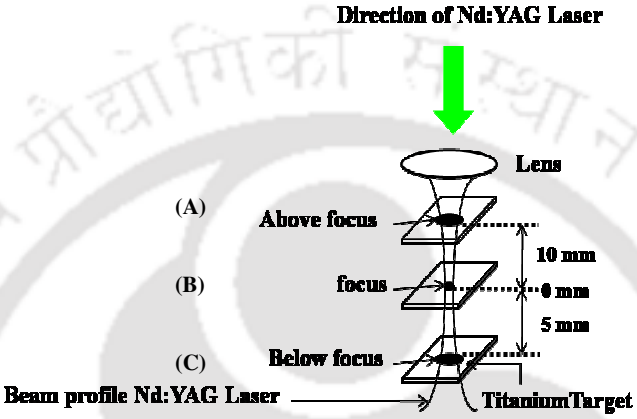

Figure 4.1 *Illustration of laser focusing condition*

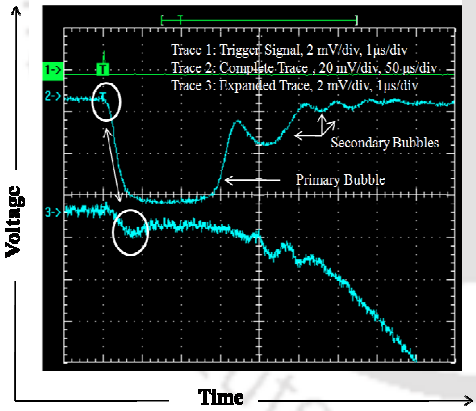

Figure 4.2 *Complete trace of Beam Deflection Set-up for tightly focused condition at 0mm from titanium-water interface*

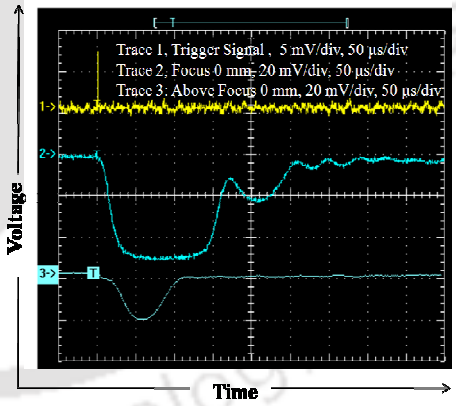

Figure 4.3 *Comparison of beam deflected signal for focusing condition (a) above focus and (b) focus*

The expanded scale of BDS traces for various focusing condition are shown in figure 4.4. Each trace was averaged over sixteen laser shots. The experiment was repeated several times for checking the reproducibility. On comparing the BDS trace for above

focus (Trace 2, figure 4.4(a)) with focus (Trace 2, figure 4.4(b)) condition at 0 mm, it appears that the first negative peak due to the shockwave is apparent but no acoustic emissions are observed for above focus condition. In addition, for above focus, the weak gradient in the photodiode signal after first negative dip reflects onset of weak cavitation bubble phenomena.

Some more interesting features are unveiled when the BDS traces for below focus condition are recorded. From figure 4.4(c), it appears that there are two shockwaves, marked as shockwaves 1 and shockwaves 2 apart from the third discontinuity before the onset of cavitation bubbles. Subsequent traces at different distances shows that the shockwave 1 (shown by red arrow, figure 4.4(c)) diverges out with increase in distance from the interfacial region. However the shockwave 2 (shown by white arrow, figure 4.4(c)) converges towards the target with increase in distance (Trace 1 to 7, 0 to 4 mm respectively) upto a distance of 5 mm (Trace 8) from the interface and beyond which it diverges out. This situation is rather alluring and can be explained from the geometry of laser ablation at below focus condition (figure 4.1). For below focus condition, the Titanium target was placed 5 mm below the focal spot of the Nd:YAG laser. The reference position for titanium-water interface is 0 mm and the focal region of Nd:YAG laser is at ~5 mm above the titanium-water interface. Hence the water breakdown predominantly takes place at 5mm from the titanium-water interface. Thus shockwaves are generated in the pure water breakdown as well as at the titanium water interface. As a result dual shockwaves are generated; one from target-water interface, shockwave 1 and the other from water breakdown, shockwave 2. It is observed that with increase in distance from the titanium-water interface, the two shockwaves approach each other and overlaps at 3mm from the titanium water interface. Trace 5, recorded at 3 mm from the titanium-water interface shows the zone

of overlap of these two shockwaves.

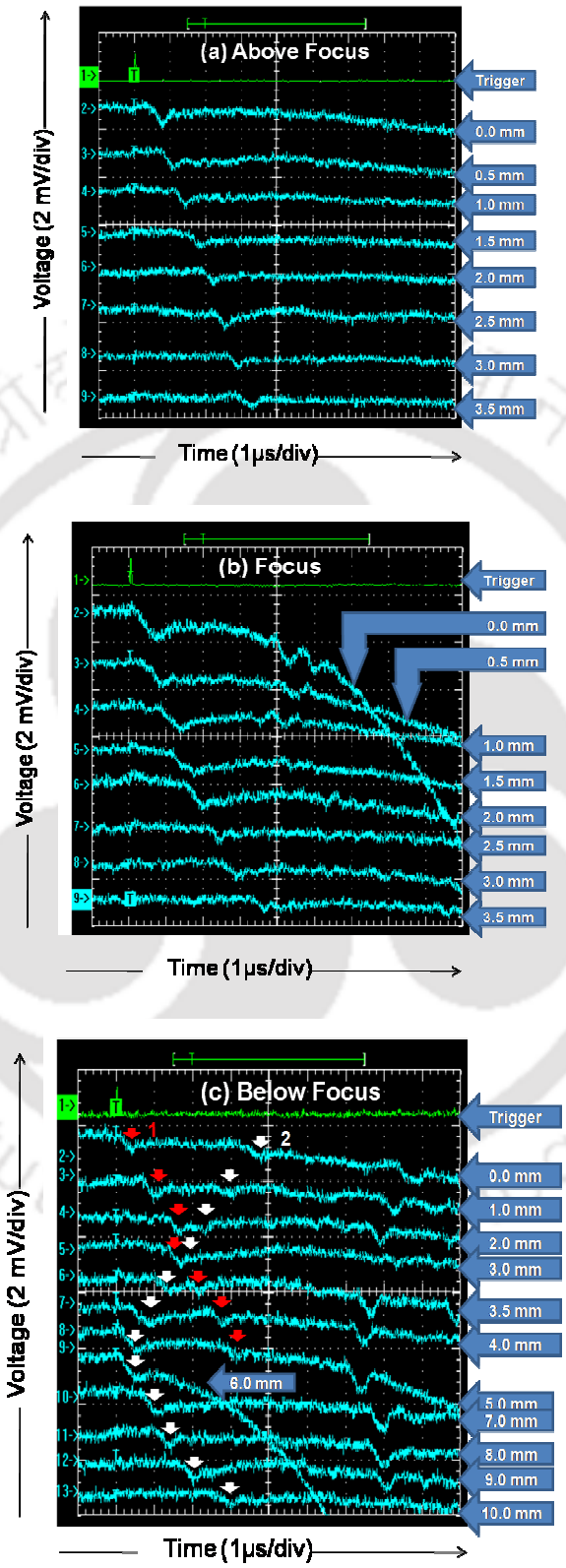

Figure 4.4 *Beam Deflection traces for (a) above focus (b) focus (c) below focus*

With further increase in distance (Trace 8, 5 mm), the probe He-Ne beam touches the area of water breakdown region where shockwaves 2 becomes prominent and shockwave 1 turns flaccid. The first peak at trace 8 is the shockwave 2 emanating from the water breakdown area and the second peak resembles the shockwave 1 evolving from titanium-water interface. Once the water breakdown area is reached, sharp fall in photodiode voltage is encountered due to exuberant cavitation bubbles and the shockwave 1 from the titanium-water interface becomes weaker and merges onto the cavitation bubbles. Hence it is not detected beyond these regions.

The spatial evolution of the shockwave velocity from the titanium-water interface for above focus, focus and below focus condition are shown in figure 4.5 (a), (b) and (c) respectively. At the vicinity of the interfacial/focal region, shockwave travels with supersonic velocity. Away from the interfacial/focal region, the velocity goes down to acoustic and subsonic speed as loss mechanisms via heat conduction, diffusion and recombination are more at these regions. The velocities at the interfacial region for above focus, focus and below focus are found to be 2.4 km/sec, 6.4 km/sec and 2 km/sec respectively. In addition, for below focus condition, the breakdown occurs in water. The shockwave velocity emanating from water breakdown is 6.5 km/sec. The shockwave pressure is estimated from the shockwave velocities using Newton's second law across a shockwave discontinuity given by [105, 106]

$$P_s - P_0 = U_S u_P \rho \qquad (4.1)$$

where P_s and P_0 are the shockwave and the hydrostatic pressure respectively, U_s is the shockwave velocity, u_p is the particle velocity and ρ is the density of water before compression. The shockwave and particle velocities are related through the equation of state and are empirically given by [107]

$$U_s = A + B u_P . \qquad (4.2)$$

where A is the sound velocity and B is a constant, these quantities are equal to 1.48 km/s and 2.07 respectively up to a pressure of 20 kbar. A higher order approximation upto 1 Mbar is given in the literature [93,108]. The estimated shockwave pressure for above focus, focus and below focus condition with the distance from the target is shown in figure 4.6 (a), (b) and (c) respectively.

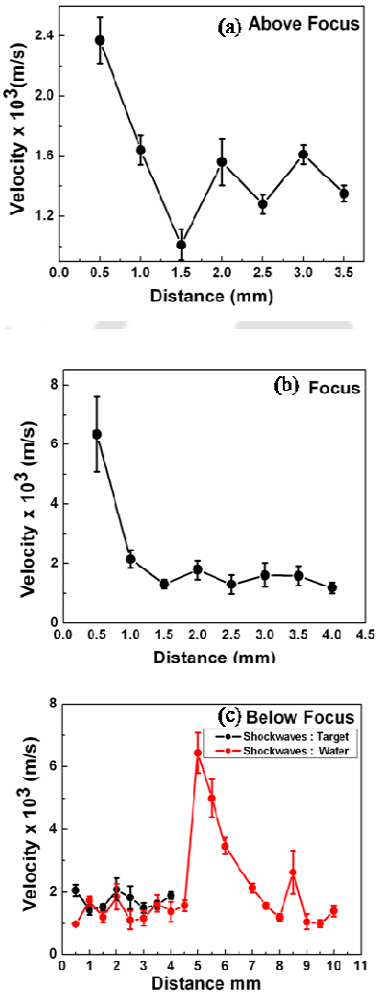

Figure 4.5 *Shockwave velocities at (a) above focus (b) focus (c) below focus*

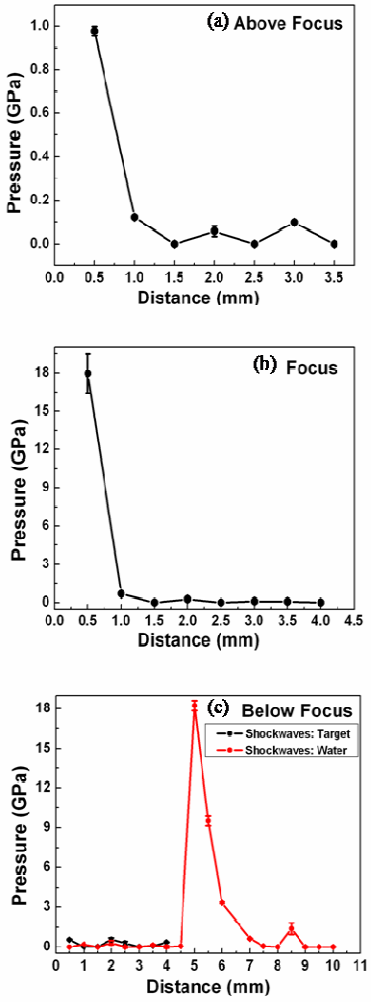

Figure 4.6 *Estimated shockwave pressure for (a) above focus (b) focus (c) below focus*

The shockwave pressure at the titanium-water interface for above focus, focus, and below focus condition using equation 4.1 and 4.2 are 1 GPa, 18 GPa and 0.6 GPa respectively. The pressure experienced at the water breakdown region for below focus condition due to shockwaves 2 (figure 4.4 (c)) is 18.3 GPa. For above focus and focus condition the maximum energy is received at the target and hence the shockwave pressure is maximum in the vicinity of the titanium target whereas for below focus condition, most of the energy is taken away by the breakdown of water. Hence the shockwave pressure is minimum on the target for below focus condition. Thus the alteration in focusing condition can modulate the pressure at titanium-water interface. This is due to the change in laser fluence and degree of liquid ionization with variation in focusing conditions.

4.2 Estimation of Temperature at Titanium-Water Interface using LIBS

LIBS was employed for various focusing condition (figure 4.1) at titanium-water interface for estimation of rotational temperature in the breakdown region. The experimental detail was described in section 2.2.1. The plasma emitted spectrum at titanium-water interface for laser focused condition (B, figure 4.1) is shown in figure 4.7. Figure 4.7(a) and 4.7(b) shows the emission spectra of OH ($A^2\Sigma^+, \upsilon = 0 \rightarrow X^2\prod, \upsilon' = 0$, centered at 306 nm) molecular band and O_2 ($b^1\Sigma_g^+, \upsilon = 0 \rightarrow X^3\Sigma_g^-, \upsilon' = 0$, centered at 762 nm), diatomic molecular oxygen. It was proclaimed in section 1.2 that the high power laser irradiation onto solid-liquid interface leads to high density target plasma with extreme pressure and temperature. The extreme physical conditions of the plasma favors further excitation, ionization and dissociation of surrounding liquid. The LIBS spectrum given in figure 4.7

validates these presumptions as emissions OH and O_2 from the molecular species of the liquid medium were observed.

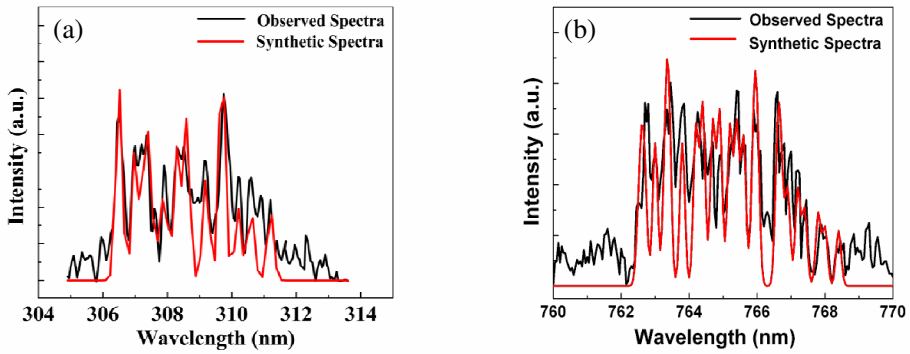

Figure 4.7 *LIBS spectra (a) OH band spectra (b) O_2 diatomic molecular spectra*

The rotational temperature of OH and O_2 band is calculated from the emission spectra. For this, the fitted spectrum of the OH and O_2 molecular band is required for comparison with the observed spectra. The fitted spectrum of OH band was produced from the theoretical diatomic molecular spectrum intensity (I_{OH}) given by.

$$I_{OH} = D_0 w^4 A_s exp\left(\frac{-E_r}{k_B T_{rot}}\right) \quad (4.3)$$

$$D_0 = \frac{C(J' + J'' + 1)}{Q_r} \quad (4.4)$$

$$E_r = B_v hc_s J'(J' + 1) \quad (4.5)$$

Where, w is the wavenumber, A_s is the oscillator strength, k_B is Boltzmann constant, T_{rot} is the rotational temperature, E_r is the rotational energy level, Q_r is the rotational partition function, J' and J'' are the lower and upper state, C is a proportionality factor , B_υ, h, c_s have the usual meaning. All the constants are taken from the available literature given by Dieke and Crosswhite [109].

The intensity (I_{O2}) of transition between the rotational levels for molecular oxygen is

given by

$$I_{O_2} = CSexp\left(\frac{-E_r}{k_B T_{rot}}\right) \quad (4.6)$$

$$S = \frac{1}{2}(J'' + Z) \quad (4.7)$$

All the parameters related to energy levels, transitions are given by Touzeau et al. [110]. Here, S is the Höln-London factors and Z = 0.75 and 1 for P and Q branches respectively. For comparison of the observed spectra with the generated spectra the instrumental broadening is taken into account. This broadening is assumed to be Gaussian. The intensity profile of the synthetic spectrum is the convolution of the equation (4.3) or (4.6) and the instrumental broadening given by [111].

$$I_{theoretical} = \frac{I_{diatomic}}{\Delta_i\sqrt{\pi/2}} exp\left(\frac{-2(\lambda-\lambda_0)^2}{\Delta_i^2}\right) \quad (4.8)$$

Where $I_{diatomic}$ is I_{OH} (equation 4.3) or I_{O2} (equation 4.6) for OH and O_2 molecular bands respectively. Δ_i is the full width at half maximum (FWHM) of the Gaussian-shaped instrumental broadening and is found to be 0.20 nm for the present experiment. The rotational temperature is obtained by comparing the synthetic spectrum with the measured spectrum using the chi-square method as shown in figure 4.7 [111]. The obtained OH rotational temperature is 2100± 200 K whereas the O_2 temperature is 965± 41 K.

LIBS spectrum could not be recorded for defocused (above focus, below focus) condition due to low fluence condition at the titanium-water interface which resulted in weak emissions.

4.3 Implication of Pressure and Temperature on Nucleation of Nanoparticles at Titanium-Water Interface.

As discussed in section 1.2, during the LIB at titanium-water interface, the extreme

physical condition of the plasma provokes excitation, ionization and dissociation of surrounding water molecules. The individual excited species of plasma then not only reacts with water at titanium-water interface but also at the plasma-water interface. For very HPHT regime, the interfacial region between plasma and water becomes the active zone for chemical reaction and facilitates non equilibrium bonding of titanium species with ionized water molecules. This situation marks as an onset of nucleation process to form titanium oxide nanoparticles. The chemical equation (4.9) gives the probable reactions taking place at the plasma-liquid interface.

$$Ti_{\text{(plasma)}} + 4OH^-_{\text{(water plasma)}} \rightarrow TiO_{2\text{ (clusters)}} + 2H_2O \Rightarrow TiO_{2\text{ (nanoparticles)}} \qquad (4.9)$$

Once the TiO_2 (clusters) are formed, it aggregates and nucleates under the HPHT conditions. This leads to decrease in volumetric driving force, Δg and increase in energy due to surface tension γ_s for an isotropic nucleus of radius r. Then the total free energy is given by [112]:

$$\Delta G = \frac{4}{3}\pi r^3 \Delta g + 4\pi r^2 \gamma_s \qquad (4.10)$$

If the nucleus contains n^{nuc} molecules and Ω is their volume then $n^{nuc}\,\Omega = \frac{4}{3}\pi r^3$. The total free energy of a nucleus containing n^{nuc} molecules becomes

$$\Delta G^{nuc} = n^{nuc}\Omega\Delta g + (6^2\pi)^{1/3}\Omega^{2/3} n^{nuc2/3}\gamma \qquad (4.11)$$

When the condition $\left.\frac{d\Delta G}{dr}\right|_{r^*} = 0$ is satisfied the clusters aggregate to form the critical nucleus of size r*. The size of the critical nucleus is given by [112]

$$r^* = \frac{2\gamma_s\left(\frac{2}{3} + \frac{V_m}{\Delta V}\right)}{[p_s(T) - p]} \qquad (4.12)$$

The time τ, taken to form the critical nucleus of size r* was given by Russell et al. and is expressed as[113]:

$$\tau = \frac{1}{2Z^2\beta *}, Z = \left[\frac{-1}{2\pi\pi_B T}\left(\frac{\partial^2 \Delta G^{nuc}}{\partial n^2}\right)\right]^{1/2}, \beta^* = \frac{p_{sat}}{\sqrt{2\pi\pi m_B T}} \quad (4.13)$$

Here Z is the Zeldovich factor and β* is the rate at which molecules are added to the nucleus. The functional form of τ deduced by Feder et al. is given by [114]

$$\tau = \sqrt{2\pi mkT}\,\frac{k_B T\gamma_s}{p_{sat}(T)(\Delta\mu)^2} \quad (4.14)$$

Δμ is the chemical potential difference given by

$$\Delta\mu = \frac{\Delta V[p - p_{sat}(T)]}{V_m N_A} \quad (4.15)$$

Here, γ_s , m, and V_m represent the surface energy (1.5 J/m^2), mass and molar volume of TiO_2 nanoparticles [115]. ΔV taken to be the molar volume difference between (Ti + O_2) and (TiO_2) molecule which is 2.3 x 10^{-6} m^3/mol. The surface energy weakly depends on the temperature, and the molar volume of (Ti + O_2) and TiO_2 are found to be approximately constant at the HPHT regime [116-118]. N_A and k_B are the Avogadro's number and Boltzmann constant respectively. T, p and p_{sat}(T) designates the temperature, pressure and saturated vapor pressure at the titanium-water interface during laser induced breakdown process. The temperature (T) in equation (4.14) is acquired from the plasma emission spectra via LIBS technique (section 4.2). Since LIBS spectrum for defocused conditions could not be detected, the investigation on nucleation dynamics of TiO_2 nanoparticles was restricted to laser focused condition (B, figure 4.1). With reference to equation 4.9, nucleation takes place between dissociated water molecules and target plasma. Assuming both of them being in thermal equilibrium, the temperature is taken to be the rotational temperature (2100 K) of OH as discussed in section 4.2. The saturated vapor pressure p_{sat}(T) at the plasma-liquid interface is procured by extrapolating the P-T diagram of the titanium at this temperature and is found to be 3.6 GPa [119]. The pressure (p) is taken to be the

shockwave pressure building at the plasma proximity measured from the BDS set-up. The estimated pressure at titanium-water interface was found to be 18 GPa for laser focused condition (B, figure 4.1, section 4.1).

By substituting the values of pressure and temperature obtained experimentally in equation 4.14, the size of TiO_2 critical nucleus (from equation 4.12) is 1.86 nm and the corresponding nucleation time τ was found to be 0.18 ns. Once the TiO_2 critical nucleus is formed it grows under HPHT conditions but the laser produced plasma is highly transient hence the rapid plasma quenching ceases the nanoparticle growth down to few nanometers. The tentative estimate of the size of the nanoparticles d, is given as [78]

$$d = V(2\tau_d - \tau) + 2r^* \qquad (4.16)$$

Here, V is the growth velocity and τ_d is the laser pulse duration. The factor of 2 is chosen since it is experimentally observed that the growth continues for twice the laser pulse duration. The growth velocity V is determined by the rate at which the number of clusters enters the nucleus and the rate of material lost into the liquid [120]. The number of clusters entering the nucleus J_{LN} and the liquid J_{NL} per unit time is represented by

$$J_{LN} = \frac{k_B T}{h} exp\left(\frac{-E_b}{k_B T}\right),\ J_{NL} = \frac{k_B T}{h} exp\left(\frac{-E_b + \Delta\Phi}{k_B T}\right) \qquad (4.17)$$

E_b is the activation energy and $\Delta\Phi$ is the free energy difference. The net no. of molecules adding to the critical nucleus per unit time is

$$V = \varsigma(J_{LN} - J_{NL}) \qquad (4.18)$$

$$\therefore V = \varsigma v exp\left(\frac{-E_b}{k_B T}\right)\left[1 - exp\left(\frac{-\Delta\Phi}{k_B T}\right)\right] \qquad (4.19)$$

As in molar units $\Delta\Phi = \frac{\Delta G}{N_A}, E_a = \frac{E_b}{N_A}, v = \frac{kT}{h}$ where ς is lattice constant in growth

direction and h is Planck's constant . The equation 4.19 is represented as

$$V = \varsigma \nu_{vib} exp(\frac{-E_a}{RT})[1 - exp(-\frac{|\Delta g_m|}{RT})] \quad , |\Delta g_m| = -RT \ln \frac{p}{p_s} \qquad (4.20)$$

where ς, υ_{vib} and E_a are the lattice constant (0.32 nm), thermal vibration frequency (4.4 x 10^{13} Hz) and activation energy respectively. Since the laser fluence (80 J/ cm^2) at tightly focused condition is very high, there is a possibility of formation of rutile phase of TiO_2 (chapter 5). Hence the activation energy is taken for rutile TiO_2 nucleation (165 kJ/mol) [121]. From equation (4.16) and (4.20), the TiO_2 nanoparticle size is found to be 21 nm with a growth velocity of 0.88 nm/ns. These results are compared with experimentally observed results described in chapter 5.

In summary, the HPHT conditions at titanium-water interface were studied using BDS and LIBS technique for various focusing conditions. BDS measurement showed formation of high pressure zone ~ 18 GPa for tightly focused condition whereas the defocusing condition experiences pressure ≤ 1GPa. The LIBS spectrum under tightly focused condition depicted OH and O_2 molecular bands due to dissociation of H_2O. The estimated rotational temperatures for these species were ~2100 K and ~1000 K respectively. However due to low fluence, at defocused condition, the LIBS spectrum at defocused conditions could not be recorded. The physical conditions (pressure, temperature) at titanium-water interface employed to study the nucleation mechanism of formation of TiO_2 nanoparticles were confined to tightly focused condition. The estimated nucleation time was 0.18 ns, growth velocity observed was 0.88 nm/ns and the estimated size of the TiO_2 nanoparticles was 21 nm.

Chapter 5

5. Synthesis of Nanoparticles via LIB at Target-Liquid Interface

One of the potential applications of target-water interaction is towards the generation of metal oxide nanoparticles. Metal oxide nanoparticles have drawn considerable attention due to its significant implementation as gas sensors, antibacterial agents, semiconductor, field emission materials etc.[8, 24-25]. Taking into account the commercial applicability of metal oxide nanoparticles, the present chapter focuses on the synthesis of copper and titanium oxide nanoparticles via laser ablation at metal-water interface. The laser focusing conditions during the LIB process were varied to control the size and structural properties of these synthesized nanoparticles. In addition, the effect of fluence and physical conditions (pressure, temperature, deduced in chapter 4) onto the size and structure of nanoparticles was investigated. Further, the estimated size of nanoparticles enumerated in section 4.3 is compared with experimentally synthesized nanoparticle size. For laser ablation at titanium-water interface, the laser energy was 4 mJ whereas the ablation at copper-water interface was performed at laser energy of 25 mJ keeping in context with the energies used for LIB in water.

5.1 Synthesis of TiO_2 Nanoparticle via Laser Ablation at Titanium-Water Interface

The schematic of experimental set-up for laser ablation of titanium target immersed in water has been discussed in section 2.2. Titanium target was ablated for various focusing conditions as shown in figure 5.1 (detail section 2.2). Figure 5.2 shows the

TEM images of Titanium Oxide nanoparticles for various focusing conditions and the corresponding particle size distribution are given in figure 5.3. To obtain the particle size distribution and average size of TiO_2 nanoparticles, TEM images were taken in different regions of the copper grid. The average particle sizes at focus, above and below focus are 13 nm, 12 nm and 9 nm respectively and the shape of the particles are perfectly spherical.

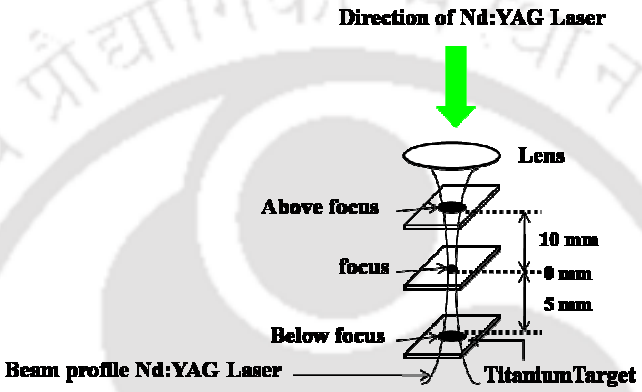

Figure 5.1 *The schematic of the various focusing conditions*

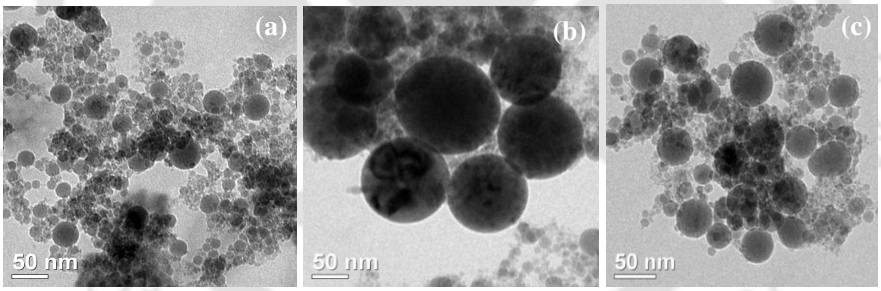

Figure 5.2 *TEM images of nanoparticles for (a) above focus (b) focus (c) below focus*

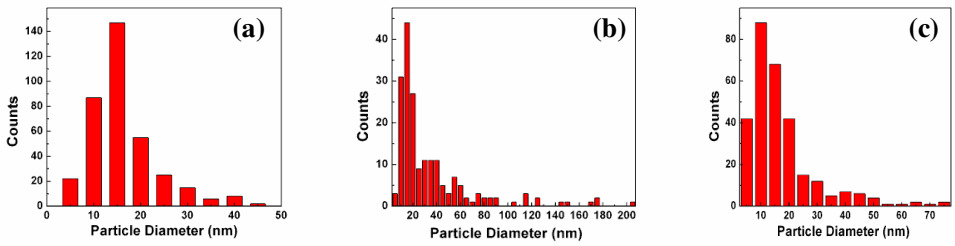

Figure 5.3 *Particle size distribution for (a) above focus (b) focus (c) below focus*

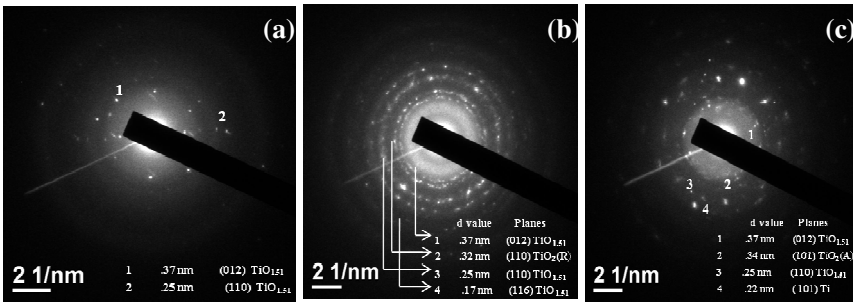

Figure 5.4 *SAD pattern for (a) above focus (b) focus (c) below focus (A:Anatase, R:Rutile)*

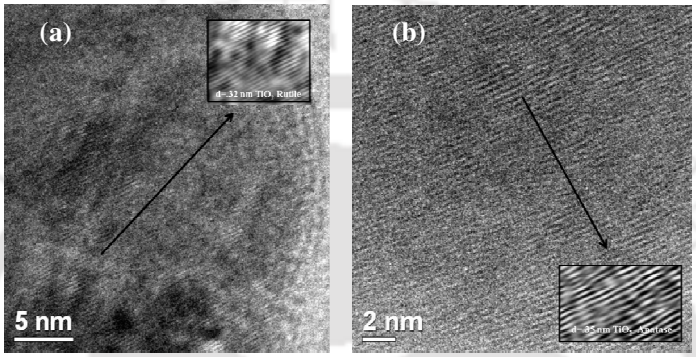

Figure 5.5 *HRTEM images for (a) focus (b) below focus condition*

Table 5.1 *Observed laser and nanoparticle parameters for various focusing condition*

Target position	Fluence (J/cm^2)	Average Particle sizes (nm)	Particle size distribution (nm)	Phases			Crystal plane (UHRTEM images) (nm)
				d_{obs} (nm)	Error ±	plane	
Above focus	1.4	12	2-45	0.377 0.256	1.0 % 0.4 %	(012) (110) $TiO_{1.5}$	--------
Focus	80	13	4-205	0.382 0.255 0.178 0.322	2.4 % 0.9 % 4.5 % 0.9 %	(012) (110) (116) $TiO_{1.5}$ (110) TiO_2 (Rutile)	0.32 nm TiO_2 (Rutile)
Below focus	0.2	9	3-75	0.382 0.256 0.344 0.221	2.5 % 0.3% 1.9% 1.6 %	(012) (110) $TiO_{1.5}$ (101) TiO_2 (Anatase) (101) Titanium	0.35 nm TiO_2 (Anatase)

To gain an insight onto the various phases of Titanium Oxide formed during ablation process SAD pattern and HRTEM images were recorded. Figure 5.4 and figure 5.5 shows the SAD and HRTEM images respectively. The observed crystal planes are mentioned in the inset of figure 5.4. The SAD pattern shows formation of TiO_x (x = 1.5) for all the focusing conditions. In addition TiO_2 (rutile) at focus; TiO_2 (anatase) and Ti nanoparticles for below focus conditions were observed. HRTEM images taken for focus and below focus condition also resembles TiO_2 (110) rutile and TiO_2 (101) anatase planes respectively. These results are summarized in table 5.1.

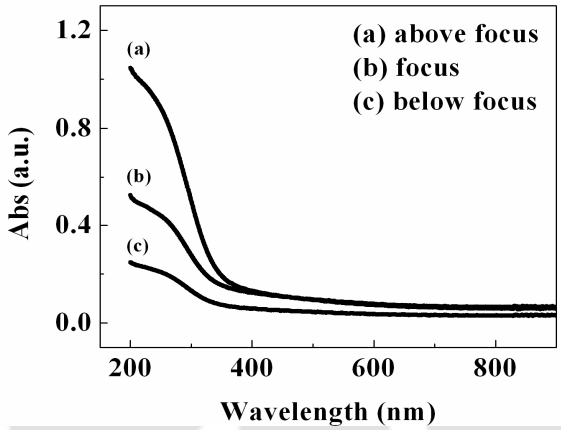

Figure 5.6 *UV-Vis spectra for various focusing condition*

Figure 5.6 shows the UV-Vis absorption spectra of TiO_2 nanoparticles synthesized via laser ablation at titanium-water interface. The absorption peak is at 235 nm. It is observed from figure 5.6 that the absorbance and yield for above focus condition (plot a) is more in comparison with tightly focused condition (plot b). These findings are ascribed to plasma shielding effect. As discussed in section 1.1., the laser ablation followed by plasma formation takes place only during the leading edge of the pulse. The plasma blocks the trailing edge and absorbs laser energy .The absorption of laser energy by plasma is termed as shielding effect which is dominant under tight focusing

conditions. Plasma shielding reduces the ablation rate and the particle concentration; hence the absorbance for synthesized nanocolloids for focus condition is relatively lower than the above focus condition. The absorbance spectrum shows that the concentration of nanocolloids is minimum at below focus condition (plot c). For below focus condition, the energy reaching target placed below focus is only 0.3 mJ. As a result the ablation rate and the collection yield for this condition is minimum.

Figure 5.7(a) shows the Photo Luminescence (PL) spectra for different focusing conditions. Lorentzian fitting onto the PL spectra for above/below focus condition is shown in figure 5.7(b). The peak at 3.19 eV corresponds to $X_{1b} \rightarrow \Gamma_3$ transition for anatase phase of TiO_2 based on the theoretically assigned nomenclature of Daude et al. [122-123]. Observed peaks at 3.6 eV/3.5 eV resembles degenerate transitions $X_{1b} \rightarrow X_{2b}/X_{1a}$ and the highest energy transition at 3.8 eV corresponds to $\Gamma_{1b} \rightarrow \Gamma_{5'a}$ of anatase TiO_2 respectively.

Figure 5.7(c) shows the lorentzian fitting onto the PL spectra for focused condition. The observed transition at 3.1 eV represents $\Gamma_{3v^+} \rightarrow R_{1c^+}$ transition for TiO_2 in rutile phase [124]. The PL spectrum at focus gives signature of TiO_2 rutile phase whereas above as well as below focus resembles TiO_2 anatase. The PL spectra for focus condition when compared with defocused conditions show a slight red shift. This further ensures formation of TiO_2 anatase phase at defocused condition and TiO_2 rutile at focus respectively. The possible formation of shallow traps due to oxygen vacancies are also observed in PL spectra. The PL at focus shows a superimposed peak at 2.7 eV whereas below focus shows small peaks at 2.8, 2.7 and 2.5 eV which are due to oxygen deficiency. Similar differences in high energy bands of rutile and anatase as well as assigned peaks for oxygen vacancies have been reported for TiO_2 nanoparticles prepared via chemical methods [125].

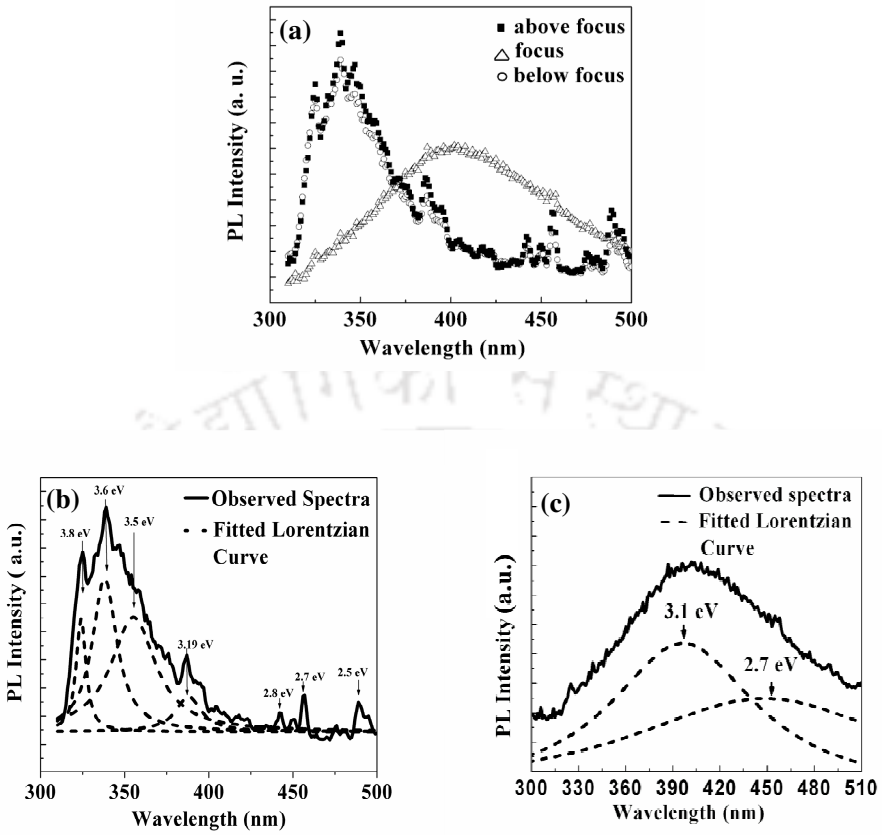

Figure 5.7 *PL spectra for (a) different focusing condition. Lorentzian Fitting for (b) defocused (c) focused condition*

The PL spectra complement the TEM results for focus and below focus conditions. But for above focus condition, TEM shows formation of $TiO_{1.5}$ whereas PL spectra ensures formation of anatase TiO_2.

Since, the PL spectra in contrast to TEM gives the collective behavior of nanocolloidal solution, it is speculated that anatase phase is also formed at above focus condition. To validate this conjecture, Raman spectra were recorded. Figure 5.8 shows the Raman peaks of synthesized TiO_2 colloidal solution dried onto a Si substrate. Figure 5.8 (a) shows Raman peaks at 155 cm^{-1}, 208 cm^{-1}, 418 cm^{-1}, 510 cm^{-1} and 633 cm^{-1} for the above focus condition which is ascertained to the E_g, E_g, B_{1g}, A_{1g} and E_g modes of anatase TiO_2 respectively [126-127]. The additional peak at 274

cm^{-1} is due to $TiO_{1.5}$. The Raman peaks in the range 200–450 cm^{-1} resembles Ti-O bending and in the domain of 610–635 cm^{-1} is Ti-O stretching [128]. Hence the Raman and PL spectrum complements each other. Thus, the nanoparticles at the above focus condition show signature of TiO_2 anatase phase alongwith $TiO_{1.5}$.

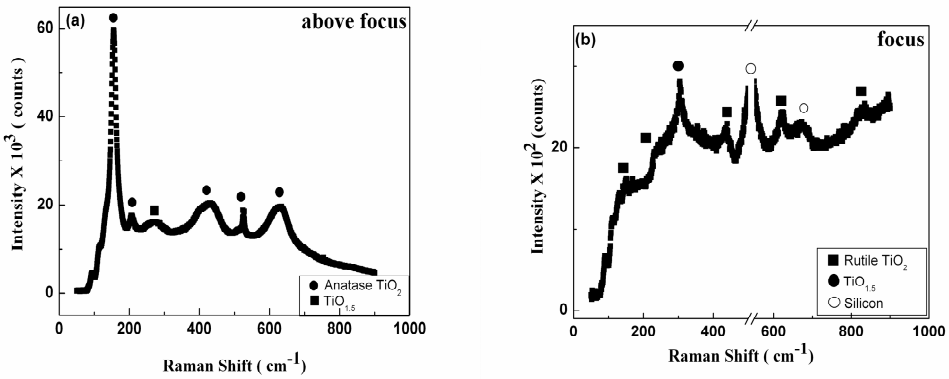

Figure 5.8 *The Raman spectra: (a) above focus and (b) focus*

The Raman spectrum for focused condition is shown in figure 5.8 (b). The concentration of the colloidal solution is less due to poor yield of TiO_2 at focus; hence, the contribution of the Si substrate at 521 cm^{-1} is enormous, so the spectral region 500–550 cm^{-1} was avoided to minimize CCD saturation. The Raman peaks were observed at 150 cm^{-1}, 231 cm^{-1}, 302 cm^{-1}, 438 cm^{-1} , 623 cm^{-1} , 673 cm^{-1} and 832 cm^{-1}. The peaks at 150 cm^{-1}, 438 cm^{-1}, 623 cm^{-1} and 832 cm^{-1} are attributed to the B_{1g}, E_g, A_{1g} and B_{2g} modes of rutile TiO_2 respectively. The additional peaks at 302 cm^{-1} and 673 cm^{-1} are due to $TiO_{1.5}$ and SiO stretching respectively[129, 130]. The extra peak at 231 cm^{-1} is cited as a rutile phase in the literature [131]. Thus it is concluded that anatase TiO_2 is formed at laser defocusing conditions whereas rutile TiO_2 is dominant under tightly focused condition.

5.1.1 Effect of Pressure and Fluence on Synthesized TiO_2 Nanoparticles.

The TiO_x (x=1.5) nanoparticles were observed for focussed as well as defocused condition. The information regarding formation of different sizes and phases of TiO_x under different focusing conditions can be sought from the reaction dynamics of pulsed laser ablation (PLA) at titanium-water interface. The surrounding water layer in PLA restricts the laser produced plasma expansion and enhances the plasma temperature and pressure. High pressure plasma (few GPa) leads to forceful impingement of ablated species into the surrounding water, so chemical reaction between target species and water molecules becomes probable. This situation may result in insufficiently oxidized ($TiO_{1.5}$) nanoparticles of Titanium. The PLA when performed at focus shows formation of TiO_2 (110) rutile in addition to TiO_x (x=1.5) nanoparticles. When ablation takes place at focus, the plasma pressure, temperature and density is much higher than the defocused conditions. The pressure and fluence at the titanium-water interface for various focusing condition are exhibited in Table 5.2. The shockwave pressure induced by laser produced plasma at titanium-water interface enumerated in chapter 4 is taken as the maximum pressure experienced at the interfacial region. For tightly focused condition, the very HPHT plasma ensures nucleation process directly at plasma-water interface and formation of high temperature phase (rutile) becomes feasible as evident from Table 5.2. The high plasma density also enhances the molecular interaction and particle growth increases and large particle sizes are observed. For the tight focusing condition, wide nanoparticle size distribution in the range of 4-205 nm is observed. The reason may be attributed to initial ablation conditions in which high fluence (80 J/cm^2) at focus results in expulsion of molten species in addition to vaporized target species. This condition is unlike defocused conditions where lower fluence (1.4 J/cm^2, 0.2 J/cm^2)

results in melting followed by vaporization of target species. This phenomena leads to narrowing down of particle size distribution [132]. The low fluence induces low pressure (1, 0.6 GPa) and low temperature plasma which favours growth of TiO_2 in anatase phase. In addition, for below focus condition, most of the physical phenomenon takes place at the interfacial zone of target plasma and water plasma, the very core of the Titanium plasma having lower energy remains inert. As a result the Ti (101) was also observed for below focus condition.

Once the nanocolloidal solution is synthesized, the stability of the nanoparticles depends upon the attractive Van der Waal's force which promotes growth of nanoparticles by aggregation and repulsive electric double layers which obstructs particle growth and thereby contributes in variation of particle sizes for all the focusing conditions [133].

Table 5.2 *Effect of fluence and pressure on particle statistics*

Focusing condition	Fluence (J/cm^2)	Pressure (GPa)	Nanoparticle size (nm)		TiO_2 Phase
			Range	Average	
Above focus	1.4	1	2-45	12	Anatase
Focus	80	18	4-205	13	Rutile
Below Focus	0.2	0.6	3-75	9	Anatase

5.1.2 Comparision of Estimated and Experimentally derived size of TiO_2 Nanoparticles.

In section 4.3, chapter 4, the experimentally derived pressure and temperature at titanium water interface was used to understand the nucleation of TiO_2 nanoparticles. Since the LIBS spectra and hence the estimated temperature were limited to tightly focused condition, the size of nanoparticles were enumerated only for this condition

of figure 5.1. Using equation 4.16, estimated pressure of 18 GPa and temperature of 2100 K, the TiO_2 nanoparticle size was found to be ~21 nm with a growth velocity of 0.88 nm/ns. The corresponding experimentally derived nanoparticle size from TEM image for tightly focused condition (B) is shown in figure 5.2 (b). The particle sizes are in the range of 4-205 nm and the average particle size is 13 nm as shown in figure 5.3(b). The deviation in the observed and estimated particle size is attributed to lack of consideration in the transient behavior of laser induced high pressure and temperature during the breakdown process. During the breakdown process, the temperature varies from 1000-5000 K and pressure goes from 2-20 GPa for a given fluence [8]. Hence it is necessary to account for the transient evolution of laser induce plasma and deduce the transient HPHT condition for elucidating the nucleation process. There are other factors which needs consideration for estimating the size of nanoparticles. At high fluence (80 J/cm^2) in the present case, the leading edge of the pulse creates direct ejection of molten globules along with the vaporized species which leads to widening of particle size distribution. However the trailing edge of the laser pulse gets absorbed by the plasma and the ejected material in the beam path from the pre-pulse. The laser absorption nay also case cause photofragementation of nanoparticles and reduction in the particle size. In addition, the molecular forces – attractive Van der Waal's force and repulsive electrostatic double layers will also influence the nanoparticle growth, immediately after the laser pulse. Hence all these factors are required to be assimilated to get compatible results for the nucleation process.

5.2 Synthesis of Copper Oxide Nanoparticle via Laser Ablation at Copper-Water Interface

Laser ablation at copper-water interface has been applied to synthesize

nanoparticulates of copper oxide. The schematic of the experimental set-up for laser ablation of copper target is given in section 2.2 and the corresponding experimental conditions are listed in Table 2.2. To tailor the size and structural properties of the synthesized nanoparticles, the copper target was ablated for various focusing conditions (T_1, T_2 and T_3) as shown in figure 5.9. After the laser exposure a colloidal solution is formed which is characterized via TEM, UV-VIS and Raman spectroscopy. The TEM images of the synthesized copper oxide nanocolloids under different focusing condition are shown in figure 5.10. Ellipsoidal shaped particles in the range of 25-200 nm are formed under tightly focused condition T_1, whereas smaller particles in the range of 2-25 nm and of size less than 10 nm are observed for defocused condition T_2 and T_3 respectively. The structural features of the nanoparticles were unveiled using SAD and HRTEM images, depicted in figure 5.11 and 5.12 respectively. The observed interplanar spacings are listed in Table 5.3. The nanoparticle obtained for T_1 (figure 5.9) appears to be in single phase and represents CuO (111), (020), ($\bar{3}$ 11), ($\bar{3}$ 13),($\bar{1}$31) planes. For defocused condition, T_2, the observed d values belongs to Cu_2O (110),(311); CuO(111); Cu(111). At T_3 , the diffraction ring resembles Cu_2O (110), (111), (311) orientations. In addition, Cu diffraction rings oriented along (111) plane is also spotted for T_3. The lattice fringes from HRTEM images correlate the SAD patterns. For tightly focused condition, T_1, the spacing of the lattice fringes, 0.23 nm and 0.18 nm, were ascribed to the d values of CuO (111) and CuO ($\bar{2}$02) plane respectively. For defocused condition, T_2 and T_3 , the lattice spacing, 0.23 nm and 0.22 nm were found to be close to the "d_{obs}" value of CuO(111) and Cu_2O (200) plane respectively. The TEM results offers a bird's-eye view and shows, while moving from T_1 to T_3 the particle size decreases and Cu_2O phase becomes more probable. But the lattice spacings of CuO and Cu_2O are fairly

close, hence to further validate the presumptions, the UV-Vis and Raman spectra were recorded.

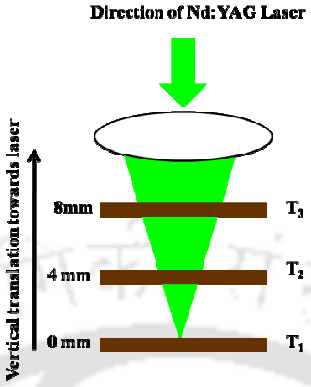

Figure 5.9 *The schematic of the various focusing conditions*

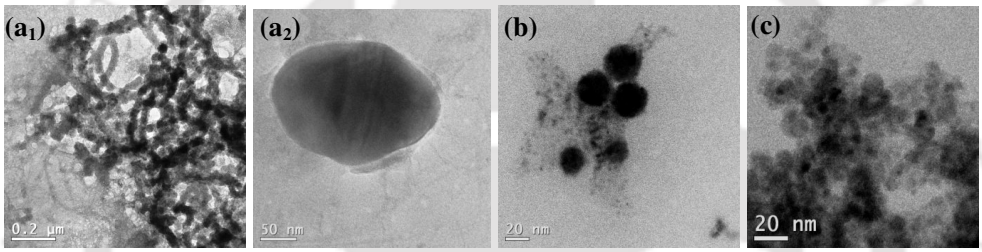

Figure 5.10 *TEM image of synthesized nanocolloids at focusing condition; (a1) & (a2) T_1 (b) T_2 (c) T_3*

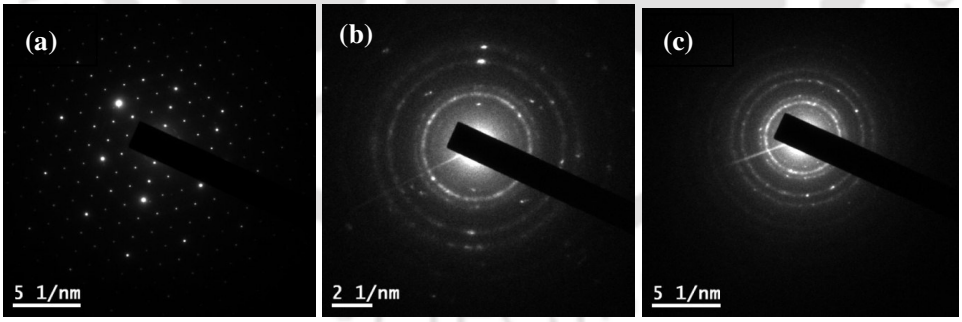

Figure 5.11 *SAD pattern of copper oxide nanocolloids at (a) T_1 (b) T_2 (c) T_3*

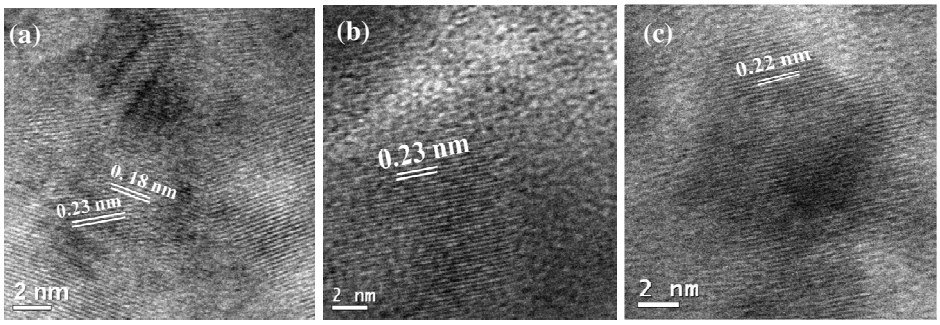

Figure 5.12 *HRTEM Images showing lattice fringes for focusing condition (a) T_1 (b) T_2 (c) T_3*

Table 5.3 *Interplanar spacings for various focusing conditions*

Position T_1		Position T_2		Position T_3	
d_{obs} values (nm)	(hkl) planes	d_{obs} values (nm)	(hkl) planes	d_{obs} values (nm)	(hkl) planes
0.23	CuO(111)	0.29	Cu_2O(110)	0.24	Cu_2O(111)
0.18	CuO($\bar{2}$02)	0.23	CuO(111)	0.20	Cu (111)
0.14	CuO($\bar{3}$11)	0.20	Cu (111)	0.17	Cu_2O(211)
0.11	CuO($\bar{3}$13)	0.13	Cu_2O(311)		
0.10	CuO($\bar{1}$31)				

The UV-Vis spectra of the in-situ prepared colloidal solution revealed some interesting features as shown in figure 5.13. The synthesized nanocolloids at the proximity of laser focus (T_1) are deconvoluted in the inset of figure 5.13. The synthesized nanocolloids at the proximity of laser focus (T_1) shows a sharp peak at 260 nm superimposed onto a broad weak peak at 350 nm, the latter being identified as charge transfer transitions ($O^{2-} \rightarrow Cu^{2+}$) in low symmetry CuO [134, 135]. The anomalous peak at 260 nm is due to the shape induced charge transfers between 2p oxygen orbitals and 4s bands Cu^{2+} ions [136,137]. The peak at 350 nm is blue

shifted when compared to those of Chen et al. [136] but are found to be in concurrence with theoretically identified transitions of Ito et al. and that of Pedersen et al [135, 138]. For defocused condition T_3, absorption peaks at 334 nm and 273 nm are attributed to the characteristics $X_3 \rightarrow X_1$ and $M_1 \rightarrow M_1$ Brillouin transitions of Cu_2O [139-141]. Further, the onset of sharp peak at 216 nm and broad absorption peak at 650 nm for defocused condition is rather alluring. The sharp absorption peak at 216 nm ascribes interband transition by Cu^0 electrons near its Fermi level [142,143]. The surface plasmon peak (SPR) of Cu lies in the 570-590 nm range. But the oxidation of copper leads to gradual shift in this absorbance peak in the range of 600-800 nm [144, 145]. The broad absorption at 650 nm is attributed to $Cu@Cu_2O$ nanoparticles formed during ablation in water [135, 146-147]. The colloids at T_2 however exhibits mixed phase and shows the onset of Cu absorption at 216 nm.

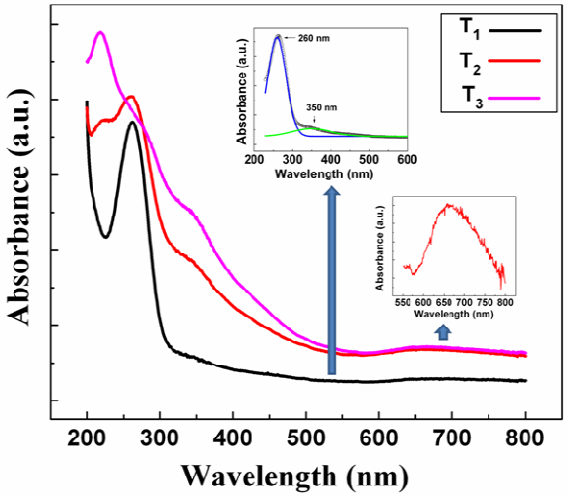

Figure 5.13 *Absorption spectra of copper oxide nanoparticles for various focusing conditions. Inset shows the absorbance at 650 nm*

The Raman spectrums for colloids synthesized under various focusing conditions at an excitation wavelength of 488 nm are shown in figure 5.14. At T_1, (figure 5.14 a) the Raman peaks were observed at 108 cm^{-1}, 292 cm^{-1} and 340 cm^{-1}. The peaks at 292

cm^{-1} and 340 cm^{-1} are ascertained to Ag and Bg $^{(1)}$ modes of CuO respectively [148-149]. CuO represents C^6_{2h} space group with two molecules per primitive cell. It has twelve zone-centre optical phonon modes 4Au+5Bu+Ag+2Bg, Au+2Bu acoustic modes, 3 Au+ 3Bu infrared active modes and Ag + 2 Bg Raman active modes. In addition, a weak impurity peak observed at 108 cm^{-1} is probably due to the Γ^-_{12} mode of Cu_2O.

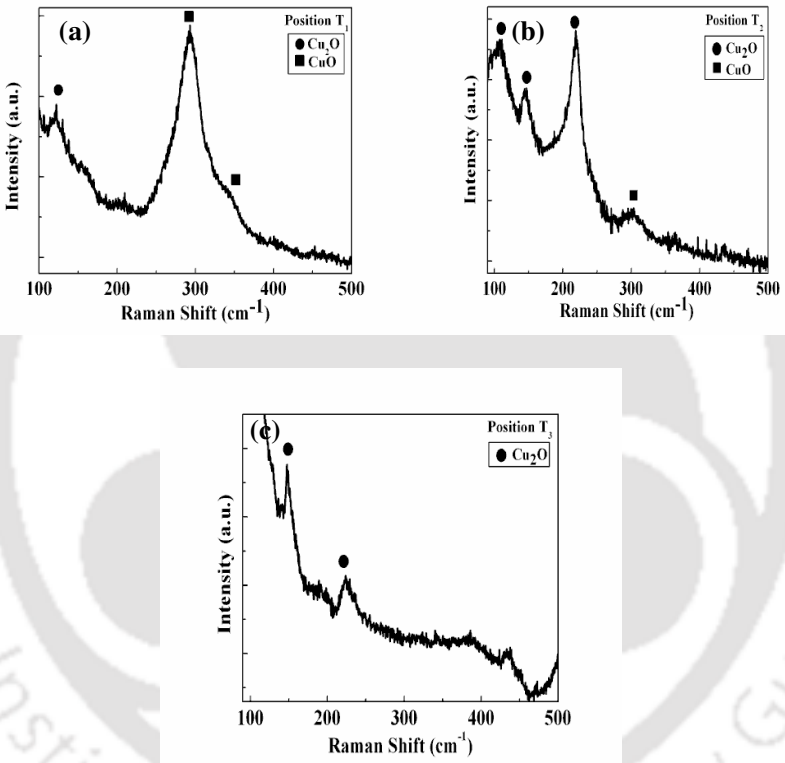

Figure 5.14 *Raman spectra of copper oxide nanocolloids at position (a) T_1 (b) T_2 (c) T_3*

For defocused condition T_2 (figure 5.14 b), prominent peaks are at 108 cm^{-1}, 146 cm^{-1}, 218 cm^{-1} and 297 cm^{-1}. The salient features at 108 cm^{-1}, 146 cm^{-1} and 218 cm^{-1} are due to Γ^-_{12}, $\Gamma^{(1)}_{15}$ and $2\Gamma^-_{12}$ modes of Cu_2O nanoparticles respectively [150-151]. Cu_2O has cuprite structure and belongs to O^4_h or P*n3m* group (point symmetry O_h or *m3m*) having inversion symmetry. The other peak at 297 cm^{-1} corresponds to the Ag

modes of CuO. At T_3 (figure 5.14 c), two peaks at 147cm^{-1} and 222 cm^{-1} were the fingerprints of the Cu_2O nanoparticles. Thus the presumptions from TEM results complement the UV-Vis and Raman spectra. To further understand the effect of focusing condition on preferred growth of specific oxides at different focusing conditions, the effect of laser fluence on the physical condition at target-liquid interface were analyzed.

The pressure is correlated to covalency for transition metal oxides. It has been proclaimed that at higher pressure the covalency of metal oxide increases [152]. Besides, covalent CuO is considered to be thermodynamically stable. Thus the plasma induced high temperature and high pressure zone at very high fluence (500 J/cm^2) at copper-water interface elucidates formation of covalent CuO at T_1. Under laser defocusing condition, low temperature and low pressure transient plasma due to relatively low fluence (10 J/cm^2) induces insufficient oxidation and rapidly ceases the particle growth. Hence smaller particle sizes are observed. The decrease in particle size activates unit cell expansion. This expansion being anisotropic makes the lattice lose its directionality. As a result the lattice preferably attains a symmetric crystal structure [153]. The choice of higher symmetry and insufficient oxidation causes Cu/Cu_2O nanoparticles of sizes < 10 nm at defocused condition.

In summary, LIB at target-liquid interface was employed to synthesize titanium oxide and copper oxide nanoparticles. The focusing conditions during the LIB process were also varied to tailor the size and structural properties of the nanoparticles. It was observed that tightly focused condition leads to larger nanoparticles whereas defocused conditions form smaller sized nanoparticles. The ablation of titanium nanoparticles showed formation of high temperature rutile phase under tightly focused

condition. The low temperature plasma at defocused condition led to preferential growth of anatase phase of TiO_2. The experimentally derived size of TiO_2 nanoparticles formed under tightly focused condition was compared to that of estimated size of nanoparticles discussed in section 4.3. The synthesized (average) and estimated size of TiO_2 nanoparticle were found to be 13 nm and 21 nm respectively. This deviation was attributed to lack of consideration in the transient behavior of laser induced high pressure and temperature during the breakdown process and inconsideration of effect of initial ablation dynamics occurring during the LIB process. The ablation at copper-water interface showed formation of copper oxide nanoparticles. The defocusing condition showed formation of smaller nanoparticles (<10 nm) with higher probability of formation of kinetically stable copper oxides (Cu_2O). For tightly focused condition thermodynamically stable copper oxides (CuO) of size $\leq$ 200 nm was formed. The synthesis of nanoparticles from laser ablation of titanium showed formation of stable nanoparticles. In contrast copper oxide nanoparticles are found to be agglomerated probably due to their high surface energies.

Chapter 6

6. Application of Synthesized Nanoparticles

In chapter 5, effect of focusing conditions of laser onto the size and structural properties of titanium oxide and copper oxide nanoparticles synthesized via LIB at titanium/copper immersed in water was discussed. In this chapter the applicability of these synthesized copper oxide nanoparticles as antibacterial agent and titanium oxide nanoparticles as photocatalyst is discussed.

6.1 Cu@Cu_2O Nanoparticles as Antibacterial Agent

In this section, Cu@Cu_2O nanoparticles synthesized at focusing condition T3 (figure 5.9, section 5.2) were used to test the antibacterial properties. A great deal of research is going on to study the biological implication of various nanoparticles [154-155]. To study the bacterial inhibition, Cu@Cu_2O nanoparticles were exposed to both gram negative and gram positive bacterial culture. Gram-positive bacteria are those whose cell wall lacks the outer membrane found in Gram-negative bacteria. In the present analysis, gram positive bacteria was – *Listeria* and gram negative bacterial cultures used were – *E. coli* and *S. paratyphi* and

Cu@Cu_2O nanoparticles synthesized via laser ablation at T3 (section 5.2) were exposed to three different bacterial stains- *Lysteria*, *E. Coli* and *S. paratyphi* at various concentrations. The synthesized nanocolloidal solutions were mixed to bacterial stains to monitor their inhibition properties using UV-Vis, Raman and cell viability assay. The experimental details were discussed in section 2.3.

6.1.1 Bacterial Inhibition of Gram positive *Listeria*

The nanoparticle treated (concentration 1.32 mg/ml) and untreated bacterial cultures of *Listeria* were grown on agar plates for cell viability assay. Bacterial viability was observed visually and numbers of bacterial colonies on agar plates were counted after 12 hrs of incubation. The agar plates showed a drastic reduction in number of colonies with nanoparticle treatment as the number of bacterial colonies reduced effectively from 992 x 10^7 to 2 x 10^7 CFU/ml. The corresponding images of the agar plate under visible light in gel documentation system (Bio Rad, USA) are shown in figure 6.1.

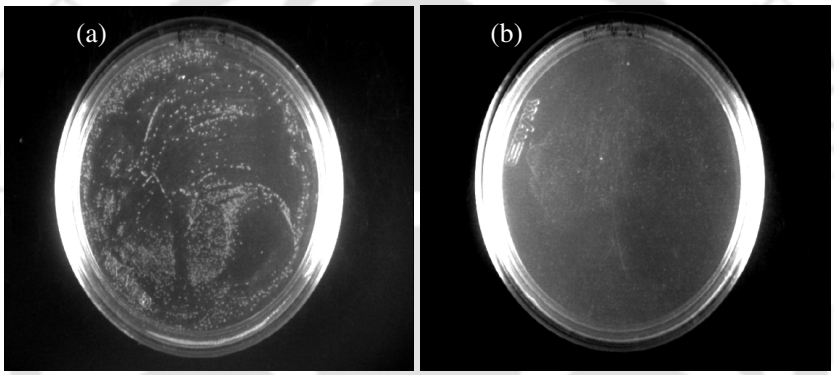

Figure 6.1 *(a) Untreated (b) Treated Listeria*

Since Cu@Cu_2O nanoparticles showed positive results in controlling the growth of gram positive bacteria, in the following sections their effect on more pathogenic gram negative bacteria (*E.coli*, *S. paratyphi*) are described.

6.1.2 Bacterial Inhibition of Gram negative *E. coli*

The effect of Cu@Cu_2O nanoparticles on gram negative-*E.coli* were investigated using UV-Vis, Raman and Cell viability assay. Bacterial viability results for *E. coli* was affirmative as the number of bacterial colonies reduced from 1450 x 10^7 to 18 x 10^7 CFU/ml upon nanoparticle treatment (concentration 1.32 mg/ml) after 12 hrs of incubation. The corresponding images of the gel documentation system are shown in

figure 6.2

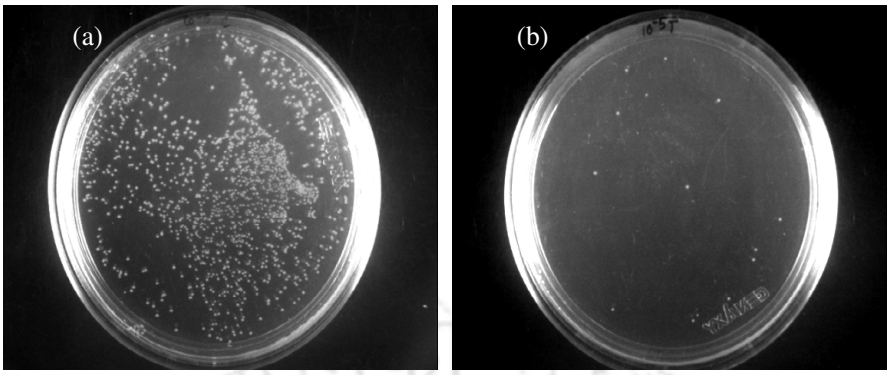

Figure 6.2 *(a) Untreated (b) Treated E. coli*

The bacterial growth index was monitored from UV-Vis spectra for *E. coli* cultures mixed to nanocolloids at various nanoparticle concentration. Figure 6.3 exhibits the scattered radiation (optical density) by the *Escherchia coli* ETEC (enterotoxic) upon nanoparticle treatment after growth of 8 hrs at 600 nm. The decrease in optical density with increase in nanoparticle concentration ensures bactericidal effect induced by the $Cu@Cu_2O$ nanoparticles.

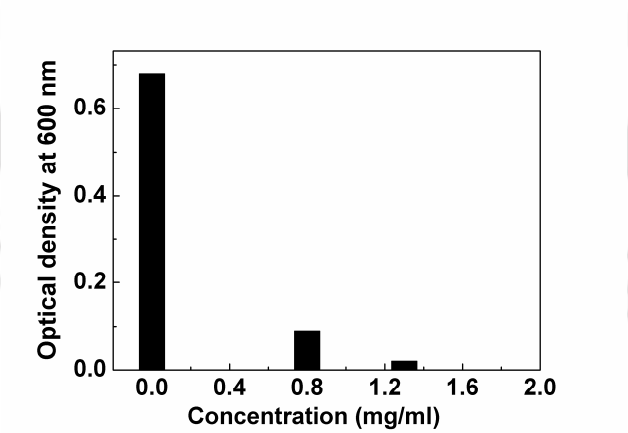

Figure 6.3 *Optical density of E. coli at 600 nm*

The Raman spectrum of the nanoparticle treated and untreated *E. coli* is shown in figure 6.4. The peak observed at 1002 cm^{-1} is assigned to Phenylalanine of *E. coli.* [156]. Phenylalanine are essential amino acids found in protein of bacterial cultures.

The structure of protein-Phenylalanine is shown in figure 6.5. It is clear from the figure 6.4 that the intensity from the characteristic Raman scattered radiation of E.coli has drastically reduced after treating with Cu@Cu_2O nanoparticles. This further confirms that the nanoparticulates are effective in inhibiting the growth of the bacterial culture.

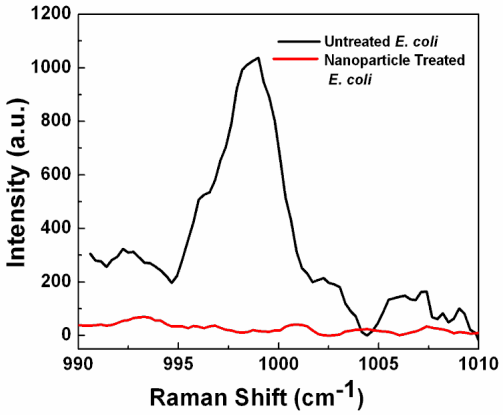

Figure 6.4 *Raman spectra of E. coli*

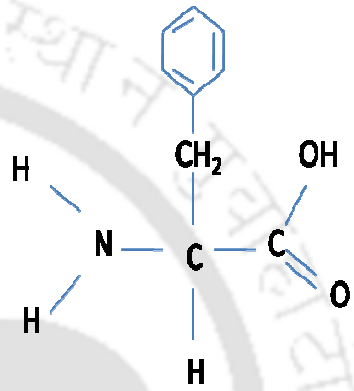

Figure 6.5 *Structure of protein-Phenylalanine*

6.1.3 Bacterial Inhibition of Gramnegative *S. paratyphi*

Paratyphoid fevers are a group of intestinal illnesses caused by strains of the bacterium *S. paratyphi*. The bacterial restraint of pathogenic *S.paratyphi* was studied by exposing it to Cu@Cu_2O nanoparticles.

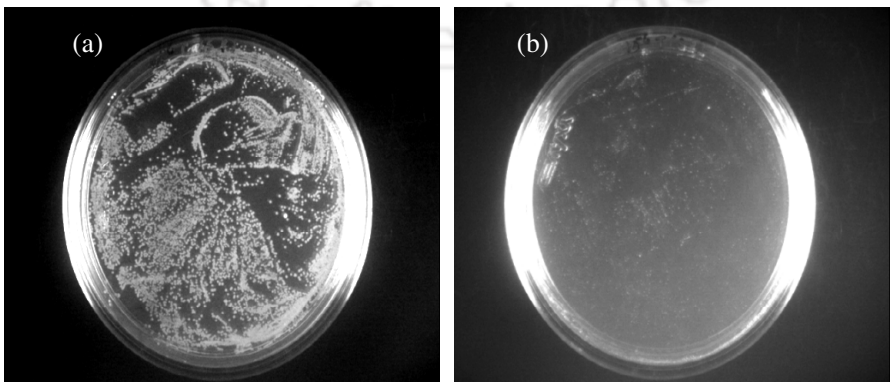

Figure 6.6 *(a) Untreated (b) Treated S. paratyphi*

Bacterial viability is clearly visible from the bacterial colonies grown on agar plates as shown in figure 6.6. The number of bacterial colonies reduced effectively from 2460 x 10^7 to 10 x 10^7 CFU/ml.

Bacterial growth index was also monitored for *S. paratyphi*. The optical density at 600 nm was recorded to study the bacterial growth curve. Figure 6.7 exhibits the scattered radiation by the *S. paratyphi* upon nanoparticle treatment as a function of time. The bactericidal effect induced by the Cu@Cu_2O nanoparticles is evident from the figure 6.7. The bacterial growth curve can be split into 4 different phases: lag phase, exponential phase, stationary phase and death phase. In the lag phase the bacterial stain adapt themselves to growth conditions. The exponential phase resembles growth of bacteria as the bacterial cells start dividing and thereby increases its population. The stationary phase signifies exhaustion of nutrients and stagnation of growth phase. At death phase, bacteria run out of nutrient and thus die out. The sudden drop in optical density of figure 6.7 after 10 hrs of incubation is attributed to the death phase of bacterial stains.

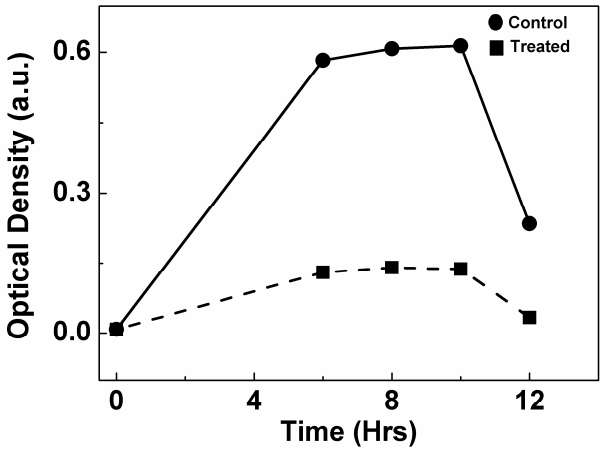

Figure 6.7 *Variation in Optical Density at 600 nm with time.*

6.1.4 Physical Mechanism behind Antibacterial Properties of Nanoparticles

The underlying physical mechanism behind bactericidal effect of Cu@Copper Oxide nanoparticles is rather elusive. Size induced larger surface area enables the nanoparticulate to migrate and penetrate the bacterial cells. The schematic of physical mechanism behind anti-bacterial activity of nanoparticles is illustrated in figure 6.8. The ability of nanoparticles to adhere to the bacterial cell wall incites biochemical reactions and leads to toxicity to the bacterial cells. The copper nanoparticles being strong reducing agents imparts damage by reacting with deoxyribonucleic acids (DNA) and oxidizes the cell nucleus by extracting electrons and rupturing the cell wall. Further, the presence of copper oxides also instigates redox reactions to generate hydrogen peroxide which thereby destructs the cytoplasmic membrane of *E. coli.* Further denaturation and solidification of protein by copper ions may also hamper the bacterial cell wall [157-158]. This observation has already been confirmed from the Raman spectra of *E.coli* discussed in section 6.1.2.

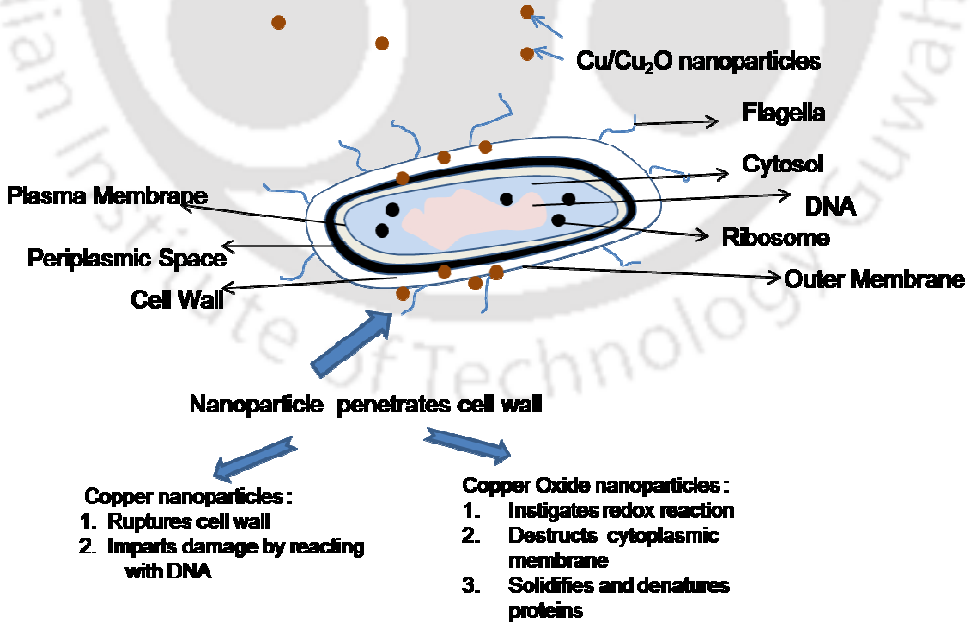

Figure 6.8 *Illustration of physical mechanism behind antibacterial activity of synthesized nanoparticles.*

6.2 TiO_2 Nanoparticles as Photocatalyst

TiO_2 is known to be a good photocatalyst [159]. In this section, the photocatalytic activity of TiO_2 nanoparticles synthesized via LIB at titanium-water interface is described. In the previous chapter (section 5.1), it was shown that at defocused condition, anatase TiO_2 is formed whereas rutile phase is observed under tightly focused condition. The photocatalytic degradation of Methylene Blue (environmental pollutant) exposed to both rutile and anatase phase of TiO_2 nanoparticles are discussed in this section.

6.2.1 Photodegradation of Methylene Blue

To study the TiO_2 photocatalytic activity, the colloidal solution containing the TiO_2 nanocolloids obtained via LIB at titanium-water interface were added to Methylene blue (organic dye) and the mixture was exposed to UV radiation. Methylene blue is a model for environmental pollutant. The photodegradation of Methylene blue (Molarity : 0.03 M) with prolonged exposure to TiO_2 nanoparticles under UV radiation was analyzed by studying its characteristic absorption spectra. The TiO_2 nanocolloids were synthesized at tightly focused and defocused conditions, in accordance to the condition depicted in figure 4.1 and resembles condition B and C respectively. From chapter 5, section 5.1, it was concluded that at defocused condition anatase TiO_2 is formed whereas rutile form of TiO_2 is observed under tightly focused condition. Figure 6.9(a) and (b) shows the absorption spectra of Methylene Blue under UV exposure at different irradiation time treated with TiO_2 nanoparticles at concentration 0.05 mg/ml (tightly focused) and 0.02 mg/ml (defocused) respectively. Figure 6.9 (a) and (b) shows 50% and 70% degradation of Methylene Blue after 4 hrs of UV exposure for focused and defocused condition respectively. The observed photodegradation of Methylene Blue is solely ascribed to synthesized TiO_2

nanocolloids since no such degradation of absorbance peak was observed when pure Methylene Blue solution (without nanoparticles) was exposed to UV radiation.

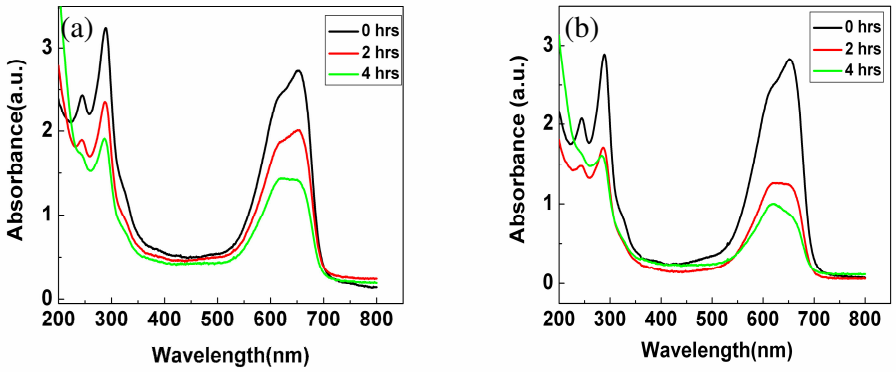

Figure 6.9 *Photodegradation of Methylene Blue treated to TiO_2 nanoparticles formed under (a) focused (rutile) (b) defocused (anatase) conditions.*

6.2.2 Physical Mechanism behind Photocatalytic Activity

The physical interpretation behind photodegradation of Methylene Blue by anatase TiO_2 nanocolloids formed under defocused condition can be understood from its band structure. The schematic of photocalytic activity is shown in figure 6.10. The band gap of anatase titanium oxide is around 3.2 eV, which corresponds to a wavelength of 388 nm. Thus absorption of radiation from UV lamp promotes reaction and generates two carriers electrons (e-) and positive holes (h+). The surface of anatase TiO_2 has a tendency to adsorb water after UV irradiation [160, 161]. Thus the water present in the synthesized nanocolloidal solution gets adsorbed onto TiO_2 surface upon UV irradiation. As a result, when this water is oxidized by positive holes, highly reactive hydroxy radicals (• OH) are formed. The hydroxyl radical then react with organic (hazardous) matter and eventually decomposes to carbon dioxide and water. Rutile TiO_2 formed under tightly focused condition also showed photodegradation. The Rutile structure of TiO_2 restraints photocatalytic activity. The photodegradation observed for tightly focused condition (rutile TiO_2 + $TiO_{1.5}$, section 5.1) is attributed

to the activity of defect states formed during laser ablation process [24]. In photodegradation of Methylene Blue, these surface defect states acts as electron pool to improve the photocatalytic activity of water-splitting reaction similar to that of shown in figure 6.10 [162].

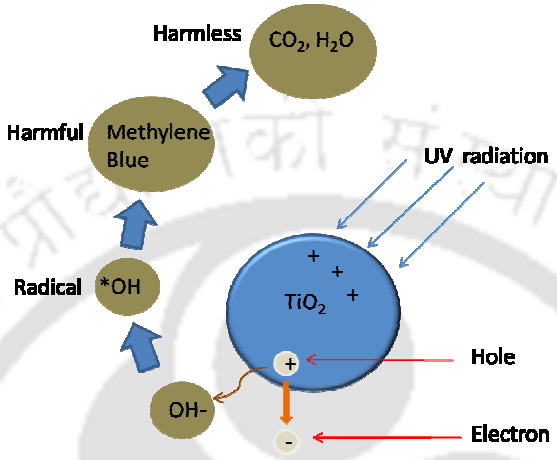

Figure 6.10 *The photocatalytic mechanism*

In summary, the antibacterial properties of Cu@Cu_2O nanoparticles were affirmative both for gram positive and gram negative bacteria. The UV-Vis, Raman and cell viability in concurrence showed bacterial restraint upon nanoparticle treatment. The size induced nanoparticle adhesion to bacterial cell wall and thereby destruction of cell wall, proteins, and cytoplasm is the possible mechanism behind antibacterial behavior of these nanoparticulates. The photocatalytic activity of TiO_2 nanoparticles were recorded for various focusing condition. For tightly focused and defocused condition the photodegradation of organic compound was found to be 50% and 70% respectively. The possible mechanism behind photocatalytic activity for anatase TiO_2 formed under defocused condition is formation of electron and hole pairs upon UV irradiation which decomposed organic matter to carbon dioxide and water. The photocatalytic activity shown at focused condition for rutile phase is attributed to the additional defect states formed during the synthesis of nanoparticles.

Chapter 7

7. Conclusion

In the present thesis, the transient evolution of pulsed laser induced breakdown process in liquid and solid-liquid interface was studied by developing various diagnostics such as beam deflection set-up, shadowgraphy, external electric probes and plasma spectroscopy across the breakdown region. The second harmonic of Nd:YAG laser was focused inside the water to study the laser plasma in liquids. The dynamics of shockwaves and cavitation bubbles associated with the laser produced plasma were analyzed using beam deflection set-up (BDS).

In BDS, a cw He-Ne laser was passed through the LIB region and was detected by photodiode connected to DSO. The photodiode was aligned to detect the maximum signal corresponding to the centre of the Gaussian beam from the output of the He-Ne laser initially. The formation of laser produced plasma and shockwaves, followed by cavitation bubbles resulted in change in refractive index with time, which in turn deflected the He-Ne beam. The deflection was registered in the form of a dip (modulation) in photodiode signal. As the plasma and bubbles were over, the He-Ne beam comes back to its original path and the corresponding photodiode signal to its initial maximum level. To record the spatial evolution of shockwaves and cavitation bubbles at different location w.r.t. the breakdown region, He-Ne laser and Photodiode were moved simultaneously along the direction of expansion of plasma. The time

delay between deflections incurred at different distances was used to measure the velocities. The shockwave was found to be propagating at supersonic speed in the range of 10^4 m/s. Its velocity was found to be increasing with increase in laser energy. The cavitation bubbles traverse at much lower speed (10^2 m/s) in the subsonic range and becomes more vigorous with increase in laser energy.

The formation of multiple bubbles in the laser induced water plasma and the subsequent bubble interaction was studied by employing the shadow graphic (SG) technique. To record the SG images, a He-Ne beam was expanded using Microscopic objective (10X) and was made to pass through the LIB region to illuminate the cavitation bubbles in the focal region. The He-Ne beam after passing through the bubbles was imaged by 15 cm lens with 1:1 correspondence onto the charge-coupled device (CCD) to record the bubble images. The sizes of the bubbles were in range of 360-230 µm after delay of 12.5 µs w.r.t the Nd:YAG laser pulse. After 30 µs, the bubble-bubble interaction led to bubble coalescence. At 50 µs, the maximum bubble coalescence of radius 380µm was observed. However, beyond the focal region bubble growth persisted for shorter duration. Bubble collapse at the focal region was observed at 60 µs and formation of liquid jet was visible after 70 µs of the laser pulse. The radius measured using SG results were used in Neppiras model to estimate the maximum gas pressure inside the bubble which was found to be 0.4 MPa.

To monitor the transient electrical perturbation in laser produced water plasma, the external electric probe (EEP) probe was used. It consists of two electrodes (diameter 16 mm, thickness 1 mm) separated by 3 mm and were placed inside water such that the plasma was formed in the centre of the two electrodes. The external electric field (~ 33 V/ cm) was applied across the electrodes placed transverse to the direction of propagation of laser beam to collect the charge carriers formed in LIB.

The transient currents due to the formation of plasma was recorded by measuring the voltage drop across 100 Ω resistance connected in series towards the grounded electrode of the probe and displayed onto the DSO. With the onset of laser pulse, a sharp increase in transient current was observed which decays exponentially after the laser pulse. With the increase in laser energy, the electron current within the laser pulse increases as ionization gets enhanced. The exponential decay time of the transient current at 24 mJ, 83 mJ and 170 mJ were found to be 1.2 μs, 1.25 μs and 1.32 μs respectively. The flow of plasma charge carriers was modeled using the heat transfer equation to estimate the thermal diffusivity of charge carriers during laser induced breakdown process. It was found to be 1.8 m/s^2, 1.9 m/s^2 and 2.2 m/s^2 for laser energy of 170 mJ, 83 mJ and 24 mJ respectively. The decrease in diffusivity with the increase in laser energy was associated to activation of scattering centers for laser produced charge carriers at higher energies.

The laser induced plasma emits the characteristic line and band spectra of its constituent species. To record the laser induced breakdown spectra (LIBS), the laser induced plasma radiation was imaged onto the entrance slit of monochromator interfaced with computer. From LIBS data, the prominent bands identified during LIB of water were Hydrogen bonded OH radical (centered at 250 nm), Hydrogen peroxide HO_2*(670 nm) , B band of O_2 (686 nm) and vibrational overtones of H_2O (695 nm).

To study the LIB at target-liquid interface, a pulsed high power laser was focused by lens onto a metal target (copper/titanium) immersed inside the distilled water of column height of 18 mm from the target surface. Irradiation of high power laser onto target leads to plasma formation of the target which interacts with surrounding water molecules to form metal oxide (copperoxide/titanium oxide) nanoparticles. The laser

focusing conditions during the LIB process were varied to tailor the size and structural properties of these nanoparticles. For this, the target was ablated under tightly focused and defocused condition. The laser ablation of titanium target immersed in water showed formation of high temperature rutile phase of TiO_2 nanoparticles under tightly focused condition. At defocused condition, growth in anatase phase of TiO_2 was observed. To understand the nucleation mechanism for the formation of nanoparticles, the pressure of the shockwave (using BDS) and temperature (using LIBS) at the titanium-water interface was measured in the LIB region for various focusing conditions of the Nd: YAG laser. The measurement of shockwave velocity via BDS was used to estimate the pressure at the interfacial region. BDS measurement showed formation of high pressure zone ~ 18 GPa for tightly focused condition on the target whereas that of the defocusing condition the pressures were ≤ 1GPa. The LIBS spectrum under tightly focused condition depicted OH band (centered at 306 nm) and O_2 (762 nm) bands. From the band structure, the estimated rotational temperatures were ~2100 K and ~1000 K respectively. From above, the nucleation time was found to be 0.18 ns, growth velocity 0.88 nm/ns and corresponding estimated size of the nanoparticles was 21 nm . The experimentally observed average nanoparticle size was 13 nm for laser focused condition. This deviation was attributed to lack of consideration in the transient behavior of laser induced high pressure and temperature during the breakdown process in the model.

For copper oxide nanoparticles, the tightly focused condition showed formation of thermodynamically stable copper oxides (CuO) of size ≤ 200 nm. The defocusing condition showed formation of smaller nanoparticles (<10 nm) with higher probability of formation of kinetically stable copper oxides (Cu_2O). In addition,

insufficient oxidation due to low fluence at defocused condition also led to formation of copper nanoparticles.

To test the practical application of these synthesized nanoparticles, antibacterial properties of copper oxide nanoparticles were analyzed. For this, the copper oxide nanoparticles (concentration 1.32 mg/ml, 0.8 mg/ml) were exposed to bacterial cultures of both gram positive and gram negative bacteria. The optical density measurement, Raman spectra and cell viability in concurrence showed bacterial restraint (~ 100 times) upon nanoparticle treatment.

The applicability of TiO_2 nanoparticles as photocatalyst was tested. For this, titanium oxide nanoparticles were mixed with Methylene Blue (environmental pollutant) and exposed to UV radiation. The photodegradation of Methylene Blue at different UV irradiation time was then recorded. For rutile TiO_2 (concentration .05 mg/ml) and anatase TiO_2 (concentration .02 mg/ml,) the photodegradation of methylene blue (molarity .03 M) was found to be 50% and 70% respectively after 4 hrs of UV exposure. Anatase TiO_2 is widely known as a good photocatalyst. The observed photodegradation for rutile phase is probably due to the defect states formed during the synthesis of nanoparticles.

Future Scope

In the laser induced breakdown in liquids, the emission of multiple secondary shockwaves were observed during onset and collapse of cavitation bubble. The estimation of this secondary shockwave pressure is relevant in context with its effect onto the particle statistics and phase transformation of synthesized nanoparticles during laser induced breakdown at target-liquid interface. In the present thesis, size of the synthesized TiO_2 nanoparticles are in the range of 4-205 nm with average size

of 13 nm whereas the estimated size of nanoparticles from the measurement of pressure and temperature is 21 nm. This deviation is attributed to lack of incorporation of transient evolution of temperature during laser induced breakdown at titanium-water interface. The temporal profile of plasma temperature is estimated from the atomic emissions which could not be detected in the present study of plasma spectroscopy due to the confinement of plasma by surrounding liquids. The confinement effect induces the shortened lifetime of excited species which gets fused with bremmstrahlung emissions. The very existence of inelastic collision further reduces the signal intensity. Hence the distinction of the LIB signal from background (arising due to bremmstrahlung processes and other noises) becomes very difficult. The limit of detection in LIBS can be enhanced by the use of dual pulse LIBS (DP-LIBS). The first pulse creates plasma and cavitation bubbles. The vaporized mass inside the gaseous bubble is then excited by the second laser pulse. Initial excitation of gases inside the cavitation bubble can be described in a manner similar to that of laser–induced breakdown in gases to some extent. This helps in improving the resolution and sensitivity for recording the atomic emissions. The estimation of temporal profile of temperature may yield results within the domain of experimentally synthesized size of nanoparticles.

Pulsed laser induced breakdown at titanium-water and copper-water interface has been used for synthesis of TiO_x and Cu_xO nanoparticles respectively. Considering the commercial applicability of various nanocomposites, this technique can be further extended for fabrication of nanocomposites of TiO_x-Cu_xO via laser ablation of copper target immersed in liquid solution containing TiO_x nanoparticles or vice versa. In addition metal-metal oxide composite can be fabricated by nanosoldering. In this technique, the colloidal solution of metal and metal oxide

nanoparticles can be synthesized via pulsed laser ablation separately. The synthesized metal and metal oxide nanocolloids can be mixed and exposed to a visible laser source (typically at $\lambda = 532$ nm). Since the Surface Plasmon Resonance (SPR) peak of metal nanoparticle lies in the visible range, the irradiation of visible laser source would lead to surface plasmon induced absorption and melting of metal nanoparticles which gets adhered to metal oxide nanoparticles.

The nanocomposite of metal and metal oxide nanoparticles are of recent interest as they have bright future prospects for their unique physical, optical, mechanical, magnetic and electrical properties which are different from that of component materials for wide range of device and sensing applications.

Bibliography

1. Einstein, A. (1917) Zur Quantentheorie der Strahlung (On the quantum theory of radiation), *Physika Zeitschrift*., **18**, pp. 121.
2. Schawlow, A. L. and Townes, C. H. (1958) Infrared and optical masers, *Physical Review.* , **112** , pp. 1940.
3. Maiman, T. H. (1960) Optical and microwave-optical experiments in ruby, *Physical Review Letters.*, **4**, pp. 564.
4. Smith, H. M. and Turner, A. F. (1965) Vacuum deposited thin films using a ruby laser, *Applied Optics*., **4**, pp. 147.
5. Bell, C. E. and Landt, J. A. (1967) Laser-induced high-pressure shock waves in water, *Applied Physics Letters.*, **10**, pp. 46.
6. Barnes, P. A. and Rieckhoff, K. E. (1968) Laser–induced underwater sparks, *Applied Physics Letters*., **13**, pp. 282.
7. Patil, P. P., Phase, D. M., Kulkarni, S. A., Ghaisas, S. V., Kulkarni S. K., Kanetkar S. M., Ogale S. B. and Bhide, V.G. (1987) Pulsed-laser–induced reactive quenching at a liquid-solid interface: Aqueous oxidation of Iron, *Physical Review Letters.*, **58**, pp. 238.
8. Yang, G. W. (2007) Laser ablation in liquids: Applications in the synthesis of nanocrystals, *Progress in Material Science.*, **52**, pp. 648.
9. Wang, C. X., Yang, Y. H., and Yang, G. W. (2005) Thermodynamical predictions of nanodiamonds synthesized by pulsed-laser ablation in liquid, *Journal of Applied Physics.*, **97**, pp. 066104.
10. Vogel, A., Nahen, K., Theisen, D., and Noack, J. (1996) Plasma formation in water by picoseconds and nanosecond Nd:YAG laser pulses – Part I: Optical breakdown at threshold and superthreshold irradiance, *IEEE Journal of Quantum Electronics*., **2**, pp. 847.

11. Noack, J., and Vogel, A. (1999) Laser–induced plasma formation in water at nanosecond to femtosecond time scales: Calculation of thresholds, absorption coeffecients, and energy denstity, *IEEE Journal of Quantum Electronics*., 35, pp. 1156.

12. Berthe, L., Fabbro, R., Peyre, P., Tollier, L. and Bartnicki, E. (1997) Shock waves from a water-confined laser-generated plasma, *Journal of Applied Physics*., **82**, pp. 2826.

13. Docchio, F., Regondi, P., Capon, M. R. C. and Mellerio, J. (1988) Study of the temporal and spatial dynamics of plasmas induced in liquids by nanosecond Nd:YAG laser pulses. 2: Plasma luminescence and shielding, *Applied Optics*., **27** , pp. 3669.

14. Kodama, T. and Tomita, Y. (2000) Cavitation bubble behavior and bubble-shock wave interaction near a gelatin surface as a study of in vivo bubble dynamics, *Applied Physics B*., **70**, pp. 139.

15. Philipp, A. and Lauterborn, W. (1998) Cavitation erosion by single laser-produced bubbles, *Journal of Fluid Mechanics*., **361** , pp. 75.

16. Vogel, A., Lauterborn, W. and Timm, R. (1989) Optical and acoustic investigations of the dynamics of laser-produced cavitation bubbles near a solid boundary, *Journal of Fluid Mechanics* ., **206** , pp. 299.

17. Zhao, R., Xu, R-Q., Shen, Z-H., Lu, J. and Ni, X-W. (2007) Experimental investigation of the collapse of laser-generated cavitation bubbles near a solid boundary, *Optics & Laser Technology*., **39** , pp. 968.

18. Isselin, J-C., Alloncle, A-P. and Autric, M. (1998) On laser induced single bubble near a solid boundary: Contribution to the understanding of erosion phenomena, *Journal of Applied Physics*., **84**, pp. 5766.

19. Nath., A. and Khare, A. (2011) Transient Evolution of multiple bubbles in laser induced breakdown in water, *Laser and Particle Beams*., **29**, pp. 1.

20. Lauterborn, W. and Hentschel, W. (1985) Cavitation bubble dynamics studied by high speed photography and holography: part one, *Ultrasonics*., **23**, pp. 260.

21. Wang, J. B., Zhang, C. Y., Zhong, X. L. and Yang, G. W. (2002) Cubic and hexagonal structures of diamond nanocrystals formed upon pulsed laser–induced liquid-solid interfacial reaction, *Chemical Physics Letters*., **361** , pp. 86.

22. Yang, G. W., Wang, J. B. and Liu, Q. X. (1998) Preparation of nano-crystalline diamonds using pulsed laser–induced reactive quenching, *Journal of Physics: Condensed Matter*., **10**, pp. 7923.

23. Yang, G. W. and Wang, J. B. (2000) Carbon nitride nanocrystals having cubic structure using pulsed laser–induced solid-liquid interfacial reaction, *Applied Physics A.*, **71**, pp. 343.

24. Liu, P., Cai, W., Fang, M., Li, Z., Zeng, H., Hu, J., Luo, X. and Jing, W. (2009) Room temperature synthesized rutile TiO_2 nanoparticles induced by laser ablation in liquid and their photocatalytic activity, *Nanotechnology*. , **20** , pp. 285707.

25. Nath, A., Laha, S. S. and Khare, A. (2011) Effect of focusing conditions on synthesis of Titanium Oxide nanoparticles via laser ablation in Titanium-Water interface , *Applied Surface Science.*, **257**, pp. 3118.

26. Mafuné, F., Kohno, J-Y, Takeda, Y., Kondow, T. and Sawabe, H. (2001) Formation of gold nanoparticles by laser ablation in aqueous solution of surfactant, *Journal of Physical Chemistry B*., **105**, pp. 5114.

27. Mafuné, F., Kohno, J., Takeda, Y., Kondow, T. and Sawabe, H. (2000) Formation and size control of silver nanoparticles by laser ablation in aqueous solution, *Journal of Physical Chemistry B.*, **104**, pp. 9111.

28. Nagy, Z., Takacs, A., Filkorn, T., Sarayba, M. (2009) Initial clinical evaluation of an intraocular femtosecond laser in cataract surgery, *Journal of Refractive Surgery*., **25** , pp 1053.

29. Weber, G. and Greulich, K. O. (1992) Manipulation of cells, organelles, and genomes by laser microbeam and optical trap, *International Review of Cytology*., **133**, pp.1.

30. Mak , G. Y., Lam, E. Y. and Choi, H. W. (2011) Laser-immersion laser micromachining of GaN grown on sapphire, *Applied Physics A*., **102**, pp. 441.

31. Ramanathan, D. and Molian, P. A. (2001) Laser micromachining using liquid optics, *Applied Physics Letters*., **78**, pp. 1484.

32. Chen, W., Chen, Y., Zou, J., Fu, X., Yang, H., Ruan, X. and Gong, G. (2009) Effect of liquid dispensing on flow field for immersion lithography, *Journal of Vaccum Science and Technology B*., **27**, pp. 2192.

33. Clarke, M. E., Xia, A., Smith, J. and Parekh, B. (2006) Point-of-use ultra-pure water for immersion lithography, *Proc. 2006 IEEE/SEMI Advanced Semiconductor Manufacturing Conference*., pp. 238.

34. Li, Y., Zhang, Y., Kuang, Y., Liu, W., Zhang, X., Qiu, Y., Xu, Y., Chen, M. and Liu, J. (2010) Study of uranium isotope separation using CO_2 laser and CO laser, *Optics Communications*., **283**, pp. 2575.

35. Makide, Y., Kato, S., and Tominaga, T. (1983) Laser isotope separation of tritium from deuterium: CO_2-laser–induced multiphoton dissociation of C_2TF_5 in C_2DF_5, *Applied Physics B*, **32**, pp. 33.

36. Feng, Y., Yang, J., Fan,J.,Yao, G., Ji, X., Zhang, X., Zheng, X. and Cui, Z. (2010) Investigation of laser-induced breakdown spectroscopy of a liquid jet, *Applied Optics*., **49**, pp. C70.

37. Sakka, T., Iwanaga, S., and Ogata, Y. H., Matsunawa, A., and Takemoto, T., (2000) Laser ablation at solid-liquid interfaces: An approach from optical emission spectra, *Journal of Chemical Physics*., **112** , pp. 8645.

38. Ledoux, G., Amans, D., Dujardin, C. and Masenelli-Varlot, K. (2009) Facile and rapid synthesis of highly luminescent nanoparticles via pulsed laser ablation in liquid, *Nanotechnology.*, **20** , pp. 445605.

39. Dolgaev, S . I., Simakin, A. V., Voronov, V. V., Shafeev, G. A. and Bozon-Verduraz, F. (2002) Nanoparticles produced by laser ablation of solids in liquid environment, *Applied Surface Science*., **186** , pp. 546.

40. Berns, M. W., Wright, W. H. and Steubing, R. W. (1991) Laser microbeam as a tool in cell biology, *International Review of Cytology*., **129** , pp. 1.

41. Shangguan, H. and Casperson, L. W. and Prahl, S. A. (1996) Microsecond laser ablation of thrombus and gelatin under clear liquids: Contact versus noncontact, *IEEE Journal of Selected Topics in Quantum Electronics*., **2** , pp. 818.

42. Zhong, P., Cocks, F., Cioanta, I. and Preminger, G. (1997) Controlled, forced collapse of cavitation bubbles for improved stone fragmentation during shockwave lithotripsy, *The Journal of Urology*, **158**, pp. 2323.

43. Matsuoka, K., Iida, S., Inoue, M., Yoshii, S., Arai, K., Tomiyasu, K. and Noda, S. (1999) Endoscopic lithotripsy with the holonium: YAG laser, *Lasers in Surgery and Medicine.*, **25**, pp. 389.

44. Vogel, A., Schweiger, P., Frieser, A., Asiyo, M. N. and Birngruber, R. (1990) Intraocular Nd:YAG laser surgery: Light-tissue interaction, damage range, and reduction of collateral effects, *IEEE Journal of Quantum Electronics,* **26**, pp. 2240.

45. Vogel, A., Engelhardt, R., Behnle, U. and Parlitz, U. (1996) Minimization of cavitation effects in pulsed laser ablation illustrated on laser angioplasty, *Applied Physics B*, **62**, pp. 173.

46. Arca, G., Ciucci, A., Palleschi, V., Rastelli, S. and Tognoni, E. (1997) Detection of environmental contaminants by time resolved laser–induced breakdown spectroscopy technique, *Applied Spectroscopy*., **51**, pp. 1102.

47. Singh, J. P., Zhang, H., Yueh, F-Y. and Carney, K. P. (1996) Investigation of the effects of atmospheric conditions on the quantification of metal hydrides using laser-induced breakdown spectroscopy, *Applied Spectroscopy*., **50**, pp. 764.

48. De Giacomo, A., Dell'Agilo, M., Casavola, A., Colonna, G., De Pascale, O. and Capitelli, M. (2006) Elemental chemical analysis of submerged targets by double-pulse laser–induced breakdown spectroscopy, *Analytical Bioanalytical Chemsitry*., **385**, pp. 303.

49. Michel, A. P. M., Farr, N. E. and Chave, A. D. (2006) Evaluation of laser–induced breakdown spectroscopy (LIBS) as a new in situ chemical sensing technique for the deep ocean, *MTS/ IEEE Conf. Proc. OCEANS-2006*., pp.1.

50. Whitehouse, A. I., Young, J. and Evans, C. P. (2002) Extreme LIBS, *OSA Trends in Optics and Photonic Series,* **81**, paper WA1.

51. Noda, M., Deguchi, Y., Iwasaki S. and Yoshikawa, N. (2002) Detection of carbon content in a high-temperature and high-pressure environment using laser–induced breakdown spectroscopy, *Spectrochimica Acta Part B*., **57**, pp. 701.

52. Singh, V. K., Singh, V., Rai, A. K., Thakur, S. N., Rai, P. K. and Singh, J. P. (2008) Quantitative analysis of gallstone using laser-induced breakdown spectroscopy, *Applied Optics.*, **47** , pp. G38.

53. Kumar, A., Yueh, F-Y., Singh, J. P. and Burgess, S. (2004) Characterization of malignant tissue cells by laser-induced breakdown spectroscopy, *Applied Optics*., **43,** pp. 5399.

54. Singh, J. P. and Thakur, S. N. (2007) "*Laser Induced Breakdown Spectroscopy",* Elsevier, UK.

55. Forget, P. and Jeandin, M. (1995) Déformation à l'échelle cristallographique d'alliages à base de nickel mono- et polycristallins par choc laser en mode confine, *J. Phys. III France*., **5**, pp. 1133.

56. Banaś, G., Elsayed-Ali, H. E., Jr Lawrence, F. V. and Rigsbee, J. M. (1990) Laser shock-induced mechanical and microstructural modification of welded maraging steel, *Journal of Applied Physics*., **67**, pp. 2380.

57. Fairand, B. P., Wilcox, B. A., Gallagher, W. J. and Williams, D. N. (1972) Laser shock-induced microstructural and mechanical property changes in 7075 aluminium, *Journal of Applied Physics*., **43**, pp. 3893.

58. Fabbro, R., Peyre, P., Berthe, L. and Scherpereel, X. (1998) Physics and applications of laser-shock processing, *Journal of Laser Applications*., **10** , pp. 265.

59. Sano, Y., Kimura, M., Mukai, N., Yoda, M., Minoru, O. and Ogisu, T. (2000) Process and application of shock compression by nanosecond pulses of frequency-doubled Nd:YAG laser, *Proc. SPIE*, **3888**, pp. 294.

60. Zhang, Y. K., Hu, C. L., Cai, L., Yang, J. C. and Zhang, X. R. (2001) Mechanism of improvement on fatigue life of metal by laser-excited shock waves, *Applied Physics A*., **72**, pp. 113.

61. Kruusing, A. (2004) Underwater and water-assisted laser processing: Part 1- general features, steam cleaning and shock processing, *Optics and Lasers in Engineering*., 41, pp. 307.

62. Yavas, O., Schilling, A., Bischof, J., Boneberg, J. and Leiderer, P. (1997) Bubble nucleation and pressure generation during laser cleaning of surfaces, *Applied Physics A*., **64**, pp. 331.

63. Hong, M. H., Huang, S. M., Luk'yanchuk, B. S. and Chong, T. C. (2003) Laser assisted surface nanopatterning, *Sensors and Actuators A*., **108**, pp. 69.

64. Lim, C. S., Hong, M. H., Lin, Y., Xie, Q., Luk'yanchuk, B. S., Kumar, A. S., and Rahman, M., (2006) Microlens array fabrication by laser interference lithography for super-resolution surface nanopatterning, *Applied Physics Letters*., **89** , pp. 191125.

65. Rothschild, M., Bloomstein, T. M., Kunz, R. R., Liberman, V., Switkes, M., Palmacci, S. T., Sedlacek, J. H. C., Hardy, D. and Grenville, A. (2004) Liquid immersion lithography: Why, how, and when?, *Journal of Vacuum Science and Technology B*. , **22** , pp. 2877.

66. Chen, W., Fu, X., Zou, J., Yang, H., Ruan, X. and Gong, G. (2010) Investigation on the critical velocity for liquid loss in immersion lithography, *Microelectronic Engineering.,***87**, pp.1070.

67. Jun, I., Takashi, O., Takeshi, E., Osamu, Y. and Takashi, N. (2005) The Modelling of ArF immersion lithography liquid, *Reports of the Research Laboratory, Asahi Glass Co., Ltd*., **55**, pp. 53.

68. Ishikawa, Y., Shimizu, Y., Sasaki, T. and Koshizaki, N. (2006) Preparation of zinc oxide nanorods using pulsed laser ablation in water media at high temperature, *Journal of Colloid and Interface Science*., **300** , pp. 612-615.

69. Tilaki, R. M., Iraji zad, A. and Mahdavi, S. M. (2006) Stability, size and optical properties of silver nanoparticles prepared by laser ablation in different carrier media, *Applied Physics A*., **84**, pp. 215.

70. Khan, S. Z., Yuan, Y., Abdolvand, A., Schmidt, M., Crouse, P., Li, L., Liu, Z., Sharp, M. and Watkins, K. G. (2009) Generation and characterization of NiO nanoparticles by continuous wave fiber laser ablation in liquid, *Journal of Nanoparticle Research.*, **11**, pp. 1421.

71. Subramanian, R., Denney, P. E., Singh, J. and Otooni, M. (1998) A novel technique for synthesis of silver nanoparticles by laser-liquid interaction, *Journal of Materials Science*., **33**, pp. 3471.

72. Link, S., Burda, C., Mohamed, M. B., Nikoobakht, B. and El-Sayed, M. A. (1999) Laser photothermal melting and fragmentation of gold nanorods: Energy and laser pulse-width dependence, *The Journal of Physical Chemsitry A*., **103**, pp. 1165.

73. Sun, J., Hu, S-L., Du, X-W., Lei, Y-W. and Jiang, L. (2006) Ultrafine diamond synthesized by long-pulse-width laser, *Applied Physics Letters*., **89**, pp. 183115.

74. Stratakis, E., Barberoglou, M., Fotakis, C., Viau, G., Garcia, C. and Shafeev, G. A. (2009) Generation of Al nanoparticles via ablation of bulk Al in liquids with short laser pulses, *Optics Express*., 2009, **17** , pp. 12650.

75. Tsuji, T., Iryo, K., Nisimura, Y. and Tsuji, M. (2001) Preparation of metal colloids by a laser ablation technique in solution: influence of laser wavelength on the ablation efficiency (II), *Journal of Photochemistry and Photobiology A : Chemistry*., **145** , pp. 201.

76. Yeh, M-S., Yang, Y-S., Lee, Y-P., Lee, H-S., Yeh, Y-H. and Yeh, C-S. (1999) Formation and characteristics of Cu colloids from CuO powder by laser irradiation in 2-propanol, *Journal of Physical Chemistry B*., **103**, pp. 6851.

77. Nichols, W. T., Sasaki, T. and Koshizaki, N. (2006) Laser ablation of a platimun target in water. II. Ablation rate and nanoparticle size distributions, *Journal of Applied Physics*., **100**, pp. 114912.

78. Wang, C. X., Liu, P., Cui, H. and Yang, G. W. (2005) Nucleation and growth kinetics of nanocrystals formed upon pulsed-laser ablation in liquid, *Applied Physics Letters.*, **87**, pp. 201913.

79. Park, H. K., Zhang, X., Grigoropoulos, C. P., Poon, C. C., and Tam, A. C. (1996) Transient temperature during the vaporization of liquid on a pulsed laser-heated solid surface, *Journal of Heat Transfer*., **118**, pp. 702.

80. Fabbro, R., Fournier J., Ballard, P., Devaux, D. and Virmont, J. (1990) Physical study of laser-produced plasma in confined geometry, *Journal of Applied Physics*., **68**, pp. 775.

81. Brujan, E. A. and Williams, G. A. (2005) Luminescence spectra of laser-induced cavitation bubbles near rigid boundaries, *Physical Review E.*, **72**, pp. 016304.

82. Celliers, P. M., Collins, G. W., Hicks, D. G., Koeing, M., Henry, E., Benuzzi- Mounaix, A., Batani, D., Bradley, D. K., Da Silva,L . B., Wallace, R. J., Moon, S. J., Eggert, J. H., Lee, K. K.M., Benedetti,L. R., Jeanloz, R., Masclet, I., Dague, N., Marchet, B., Rabec Le Gloahec, M., Reverdin,C., Pasley, J., Willi, O., Neely, D., and Danson, C. (2004) Electronic conduction in shock-compressed water, *Physics of Plasma.,* **11**, pp. L41.

83. Zhong,P., Cioanta, I.,Cocks, F.H., and Preminger G. M. (1997) Inertial cavitation and associated acoustic emission produced during electrohydraulic shock wave lithotripsy *Journal of Acoustical Society of America.*, **101**, pp. 2940.

84. Gilmore, F. R. (1952) The growth or collapse of a spherical bubble in a viscous compressible liquid, *California Institute of Technology.*, **Report no. 26-4**, pp. 1.

85. Rayliegh, L. (1917) On the pressure developed during the collapse of a spherical cavity, *Philosophical Magazine.*, **34**, pp. 94.

86. Chesters, A. K. and Hofman, G. (1982) Bubble coalescence in pure liquids, *Applied Scientific Research.*, **38**, pp. 353.

87. Khoroshev, G. A. (1963) Collapse of Vapor-Air Cavitation Bubbles, *Soviet Physics-Acoustics*., **9**, pp. 275.

88. Neppiras, E. A. (1980). Acoustic Cavitation, *Physics Reports*., **61** , pp. 159.

89. Espejo, V., Bertuccelli, D. and Ranea-Sandoval, H. F. (2010) Laser-induced plasma in

liquid conduction cell : Alterations in current-to-voltage characteristics, *IEEE Transactions on Plasma Science.*, **38**, pp. 86.

90. Kumar, B. and Thareja, R. K. (2010) Synthesis of nanoparticles in laser ablation of aluminum in liquid , *Journal of Applied Physics.,***108**, pp. 064906.
91. Ng, C. W., Ho, W. F. and Cheung, N. H. (1997) Spectrochemical analysis of liquids using laser-induced plasma emissions : effects of laser wavelength on plasma properties, *Applied Spectroscopy.,* **51**, pp. 976.
92. Evans, J. R., Badger, A. D., Falliès, F., Mahdieh, M., Hall, T. A., Audebert,P. , Geindre, J-P, Gauthier, J-C., Mysyrowicz,A., Grillon,G. and Antonetti, A. (1996) Time- and Space-resolved optical probing of femtosecond-laser-driven shock waves in aluminum, *Physical Review Letters.,* **77**, pp. 3359.
93. Mitchell, A. C. and Nellis ,W. J. (1982) Equation of state and electrical conductivity of water and ammonia shocked to the 100 GPa (1 Mbar) pressure range, *Journal of Chemical Physics.*, **76**, pp. 6273.
94. Fujimoto, T. and McWhirter, R. W. P. (1990) Validity criteria for local thermodynamic equilibrium in plasma spectroscopy, *Physics Review A.*, **42**, pp. 6588.
95. Griem, H. R. (1964) *Plasma Spectroscopy.*, New York: McGraw-Hill.
96. Eliezer, S., Krumbein, A. D. and Salzmann, D. (1978) A generalized validity condition for local thermodynamic equilibrium in a laser-produced plasma, *Journal of Physics D : Applied Physics.*, **11**, pp. 1693.
97. Sah, C-T. (1991) *Fundamentals of solid-state electronics*, World Scientific Publishing Company, pp. 236.
98. Landau, L. D. and Lifshitz, E. M. (1987) *Fluid Mechanics* , 2nd ed., Oxford : Butterworth-Heinemann, pp. 192.
99. Janik, I., Bartels, D. M. and Jonah, C. D. (2007) Hydroxyl radical self- recombination reaction and absorption spectrum in water up to 350˚C, *Journal of Physical Chemistry A*, **111**, pp. 1835.
100. Ball, S. M., Langridge, J. M. and Jones, R. L. (2004) Broadband cavity enhanced

absorption spectroscopy using light emitting diodes, *Chemical Physics Letters*., **398** , pp. 68.

101. Jenniskens, P. and Mandell, A. M. (2004) Hydrogen emission in meteors as a potential marker for the exogenous delivery of organics and water, *Astrobiology*., **4** , pp. 123.

102. Joshi, A. A., Locke, B. R., Arce, P. and Finney, W. C. (1995) *Journal of Hazardous Materials.*, **41**, pp. 3.

103. Rubtsov N. M., Tsvetkov, G. I., Chernysh, V. I. and Azatyan, V. V. (2007) Effects of reactive admixtures on the near-IR emission spectra of hydrogen and deuterium oxidation flames, *Kinetics and Catalysis*., **48**, pp. 183.

104. Zhong, P., Cioanta, I., Zhu, S., Cocks, F. H. and Preminger, G. M. (1998) Effects of tissue constraint on shock wave-induced bubble expansion *in vivo*, *Journal of Acoustical Society of America.*, **104**, pp. 3126.

105. Fujimoto, J. G., Lin, W. Z., Ipper, E. P., Puliafito, C. A. and Steinert, R. F. (1985) Time-resolved studies of Nd:YAG laser–induced breakdown, *Investigative Ophthalmology & Visual Science*., **26** , pp. 1771.

106. Doukas, A. G. , Zweig, A. D., Frisoli, J. K., Birngruber, R. and Deutsch, T. F. (1991) Non-invasive determination of shock wave pressure generated by optical breakdown, *Applied Physics B.*, **53**, pp. 237.

107. Harris, P. and Presles, H. N. (1981) Reflectivity of 5.8 kbar shock front in water, *Journal of Chemical Physics.*, **74**, pp. 6864.

108. Rice, M. H. and Walsh, J. M. (1957) Equation of state of water to 250 kilobars, *Journal of Chemical Physics.*, **26** , pp. 824.

109. Dieke, G. H. and Crosswhite, H. M. (1961) The ultraviolet bands of OH Fundamental data, *Journal of Quantum Spectroscopy and Radiation Transfer*., **2**, pp. 97.

110. Touzeau, M., Vialle, M., Zellagui, A., Gousset, G., Lefebvre, M. and Pealat, M. (1991) Spectroscopic temperature measurements in oxygen discharge, *Journal of Physics D: Applied Physics.*, **24**, pp. 41.

111. Moon, S. Y., and Choe, W. (2003*)* A comparative study of rotational temperatures using

diatomic OH, O_2 and N_2^+ molecular spectra emitted from atmospheric plasmas, *Spectrochimica Acta Part B*., **58**, pp. 249.

112. Wang, C. X., Yang, Y. H., Xu, N. S. and Yang, G. W. (2004) Thermodynamics of Diamond Nucleation on the Nanoscale, *Journal of American Chemical Society.,* **126**, pp. 11303.

113. Russell, K. C. (1980) Nucleation in solids: The induction and steady state effects *Advances in Colloid and Interface Science*., **13**, pp. 205.

114. Feder, J., Russel, K. C., Lothe, J. and Pound, G. M. (1966) Homogeneous Nucleation and Growth of Droplets in Vapour, *Advance Physics.*, **15**, pp. 111.

115. Oskam, G., Nellore, A., Penn, R. L. and Searson, P. C. (2003) The Growth Kinetics of TiO_2 Nanoparticles from Titanium(IV) Alkoxide at High Water/Titanium Ratio, *Journal of Physical Chemistry B*., **107**, pp. 1734.

116. Errandoneaa, D., Meng, Y., Somayazulu, M. and Ha¨usermann, B. (2005) Pressure-induced α→ω transition in titanium metal: a systematic study of the effects of uniaxial stress, *Physica B*., **355**, pp. 116.

117. Akahama, Y., Kwamura, H., Häusermann, D., Hanfland, M. and Shimomura, O. (1995) New High-Pressure Structural Transition of Oxygen at 96 GPa Associated with Metallization in a Molecular Solid, *Physical Review Letters.* , **74**, pp. 4690.

118. Afir, A., Achour, M. and Saoula, N. (1999) X-ray diffraction study of Ti-O-C system at high temperature and in a continuous vacuum, *Journal of Alloys Compounds.,* **288**, pp. 124.

119. Young, D. A. (1991) *Phase diagrams of the elements* (University of California Press).

120. Sangwal, K. (2007) *Additives and Crystallization process: From Fundamentals to Applications* (John Wiley & Sons, Ltd.) pp. 74.

121. Zhang, H. and Banfield , J. F. (1999) A new kinetic model for the anatase-to-rutile phase transformation in nanocrystalline material revealing a second order dependence on the number of particles*, American Mineralogist.,* **84**, pp. 528.

122. Daude, N., Gout, C., Jouanin, C. (1977) Electronic band structure of titanium dioxide.,

Physical Review B., **15**, pp. 3229.

123. Serpone , N., Lawless, D. and Khairutdinov, R., (1995) Size effects on the photophysical properties of colloidal anatase TiO_2 particles: Size quantization or direct transitions in this indirect semiconductor? , *Journal of Physical Chemistry.*, **99**, pp. 16646.

124. Madelung, O. , Rössler, U. and Schulz,M. (2006) Landolt-Börnstein - Group III Condensed Matter : Numerical Data and Functional Relationships in Science and Technology, 41, Non-Tetrahedrally Bonded Binary Compounds II, D, Chapter "Titanium oxide (TiO2): energy gap, further interband transitions in rutile," , (Springer Verlag , New York).

125. Abazović, N. D., Čomor, M. I., Dramićanin, M. D., Jovanović, D. J. , Ahrenkiel, S. P., Nedeljković, J. M. (2006) Photoluminescence of anatase and rutile TiO_2 particles, *Journal of Physical Chemistry B.*, **110** , pp. 25366.

126. Qian, L., Du, Z., Yang, S. and Jin, Z. (2005) Raman study of titania nanotube by soft chemical process, *Journal of Molecular Structure.*, **749**, pp. 103.

127. Porto, S. P.S., Fleury, P. A. and Damen, T. C. (1967) Raman spectra of TiO_2, MgF_2, ZnF_2,FeF_2 and MnF_2, *Physical Review.*, **154**, pp. 522.

128. Fernández-García, M., Wang, X., Belver, C., Hanson, J.C. and Rodriguez, JA. (2007) Anatase-TiO_2 Nanomaterials : Morphological/Size Dependence of the Crystallization and Phase Behavior Phenomena, *Journal of Physical Chemistry C.*, **111**, pp. 674.

129. Shin, S. H., Aggarwal, R. L., Lax, B. and Honig, J. M. (1974) Raman scattering in Ti_2O_3-V_2O_3 alloys, *Physical Review B.*, **9** , pp. 583.

130. Gucsik, A., Koeberl, C., Brandstätter, F. , Libowitzky, E. and Zhang, M. (2004) Infrared, Raman, and cathodoluminescence studies of impact glasses, *Meteoritics & Planetary Science* ., **39**, pp. 1273.

131. Barborini, E., Kholmanov, I. N., Piseri, P., Ducati, C., Bottani, C. E. and Milani, P. (2002) Engineering the nanocrystalline structure in TiO_2 films by aerodynamically filtered cluster deposition, *Applied Physics Letters.*, **81**, pp. 3052.

132. Nichols, W. T., Sasaki, T. and Koshizaki, N. (2006) Laser ablation of a platinum target in water. I. Ablation mechanisms , *Journal of Applied Physics.*, **100** , pp. 114911.

133. Israelachvili, J. (1995) *Intermolecular and Surface Forces*, (Academic Press, London).

134. Chary, K. V. R., Sagar, G. V., Srikanth, C. S. and Rao, V. V. (2007) Characterization and Reactivity of Copper Oxide Catalysts Supported on TiO_2–ZrO_2 , *Journal of Physical Chemistry* B., **111**, pp. 543.

135. Pedersen, D. B., Wang, S. and Liang, S. H. (2008) Charge-Transfer-Driven Diffusion Processes in Cu@Cu-Oxide Core–Shell Nanoparticles: Oxidation of 3.0 ± 0.3 nm Diameter Copper Nanoparticles, *Journal of Physical Chemistry C.*, **112**, pp. 8819.

136. Chen, X. Y., Cui, H., Liu, P. and Yang, G. W. (2007) Shape-induced ultraviolet absorption of CuO shuttlelike nanoparticles, *Applied Physics Letters*., **90**, pp. 183118.

137. Nestour, A. L., Gaudon M,Villeneuve, G., Andriessen, R. and Demourgues, A., (2007) Steric and Electronic Effects Relating to the Cu^{2+} Jahn–Teller Distortion in $Zn_{1-x}Cu_xAl_2O_4$ Spinels, *Inorganic Chemistry*., **46**, pp. 2645.

138. Ito. T., Yamaguchi, H., Masumi, T. and Adachi, S., (1998) Optical Properties of CuO Studied by Spectroscopic Ellipsometry, *Journal of Physical Society of Japan.*, **67** , pp. 3304.

139. Ching, W. Y., Xu, Y-N. and Wong, K. W. (1989) Ground-state and optical properties of Cu_2O and CuO crystals, *Physical Review B*, **40** , pp. 7684.

140. Ito, T., Kawashima, T., Yamaguchi, H., Masumi, T. and Adachi, S. (1998) Optical Properties of Cu_2O Studied by Spectroscopic Ellipsometry, *Journal of Physical Society of Japan*., **67** , pp. 2125.

141. Kleinman, L. and Mednick, K. (1980) Self-consistent energy bands of Cu_2O, *Physical Review B.*, **21** , pp. 1549.

142. Oliver, A, Cheang-Wong, J. C., Roiz, J., Hernández, J. M., Rodríguez-Fernández, L. and Crespos, A. (2001) Optical absorption and emission studies of 2 MeV Cu-implanted silica glass, *Nuclear Instrument and Methods* in Physics Research *B.*, **175-177**, pp. 495.

143. Ehrenreich, H. and Philipp, H. R. (1962) Optical properties of Ag and Cu, *Physical Review*., **128** , pp. 1622.

144. Stepanov, A. L., Kreibig, U., Hole, D. E., Khaibullin, R. I., Khaibullin, I. B. and Popok, V. N. (2001) Laser annealing of sapphire with implanted copper nanoparticles, *Nuclear Instrument and Method in Physics Research* B., **178** , pp. 120.

145. Zamkovets, A. D., Kachan, S. M. and Ponyavina, A. N. (2003) Optical properties of thin-film metal-dielectric nanocomposites, *Physical Chemistry Solid State.*, **4** , pp. 627.

146. Kazakevich, P. V., Voronov, V. V., Simakin, A. V. and Shafeev, G. A. (2004) Production of copper and brass nanoparticles upon laser ablation in liquids , *Quantum Electronics.,* **34**, pp. 951.

147. Kazakevich, P. V., Simakin, A. V., Voronov, V.V. and Shafeev, G. A. (2006) Laser induced synthesis of nanoparticles in liquids, *Applied Surface Science.*, **252**, pp. 4373.

148. Goldstein, H. F., Kim, D-S., Yu, P. Y., Bourne, L. C., Chaminade, J-P. and Nganga, L., (1990) Raman study of CuO single crystals, *Physical Review B*., **41** , pp. 7192.

149. Wang, X., Xi, G., Xiong, S., Liu, Y., Xi, B., Yu, W. and Qian, Y. (2007) Solution-Phase Synthesis of Single-Crystal CuO Nanoribbons and Nanorings, *Crystal Growth and Design*., **7** , pp. 930.

150. Powell, D., Compaan, A., Macdonald, J. R. and Forman, R. A. (1975) Raman-scattering study of ion-implantation-produced damage in Cu_2O, *Physical Review B*., **12** , pp. 20.

151. Balkanski, M., Nusimovici, M. A. and Reydellet, J. (1969) First order Raman spectrum of Cu_2O, *Solid State Communication.*, **7** , pp. 815.

152. Drickamer, H. G. (1965) *Solid State Physics: Advances in Research and Applications* ,ed F Seitz , D Turnbull and H Ehrenfest,(New York Academic Press).

153. Ayyub, P., Palkar, V. R., Chattopadhyay, S. and Multani, M. S. (1995) Effect of crystal size reduction on lattice symmetry and cooperative properties , *Physical Review B.*, **51** , pp. 6135.

154. Raffi, M., Mehrwan, S., Bhatti, T. M., Akhter, J. I., Hameed, A., Yawar, W. and

Masood ul Hasan, M. (2010) Investigations into the antibacterial behavior of copper nanoparticles against *Escherichia coli* ,A*nnals of Microbiology.*, **60**, pp. 75**.**

155. Lok, C., Ho C. and Chen, R. (2006) Proteomic Analysis of the Mode of Antibacterial Action of Silver Nanoparticles, *Journal of Proteome Research*., **5**, pp. 916.

156. Xie, C. and Li, Y-G. (2003) Confocal micro-Raman spectroscopy of single biological cells using optical trapping and shifted excitation difference techniques, *Journal of Applied Physics.*, **93**, pp. 2982.

157. Tong , G., Yulongb, M., Peng, G. and Zirong , X. (2005) Antibacterial effects of the Cu(II)-exchanged montmorillonite on Escherichia coli K88 and Salmonella choleraesuis, *Veterinary Microbiology.*, **105**, pp. 113.

158. Hoshino, N., Kimura, T., Yamaji, A. and Ando, T.(1999) Damage to the cytoplasmic membrane of Escherichia coli by catechin-copper (II) complexes, *Free Radical Biology and Medicine.*, **27**, pp. 1245.

159. Linsebigler, A.L., Lu, G. and Jr., Yates, J. T. (1995) Photocatalysis on TiO_n Surfaces: Principles, Mechanisms, and Selected Results, *Chemical Review.,* **95**, pp. 735.

160. Hashimoto, K., Irie, H. and Fujishima, A. (2007) TiO_2 photocatalysis: a historical overview and future prospects, *AAPPS Bulletin*., **17**, pp. 12.

161. Kaneko, M. and Okura, I. (2002) *Photocatalysis: science and technology* (Springer-Verlag, Heidelberg)

162. Shi, J., Cui, H., Liang, Z., Lu, X., Tong, Y., Su, C. and Liu, H. (2011) The roles of defect states in photoelectric and photocatalytic processes for $Zn_xCd_{1-x}S$, *Energy and Environmental Science*., **4** , pp. 466.

List of Publications

- **Book Chapters**

1. Laser–Induced Breakdown in Liquid and at Solid–Liquid Interface, **Arpita Nath** and Alika Khare, Publisher : Pan Stanford Publications,(In Press)

- **Journal Papers (Accepted/Published)**

1. Antibacterial activity of copper oxide nanoparticles synthesized via laser ablation in liquids, **Arpita Nath**, Archana Das, Latha Rangan and Alika Khare, Science on Advance Materials (accepted).
2. Antibacterial Activity of Cu@Cu_2O Nanoparticles Synthesized via Laser Ablation in Liquids, **Arpita Nath**, Archana Das, Latha Rangan and Alika Khare, Proc. SPIE (accepted)
3. Effect of Focusing Conditions on Laser Induced Shockwaves at Titanium-Water Interface , **Arpita Nath** and Alika Khare , Applied Optics, **50**, pp. 3275-3281 (2011).
4. Transient Evolution of multiple bubbles in laser induced breakdown in water, **Arpita Nath** and Alika Khare, Laser and Particle Beams, **29**, pp 1-9, (2011).
5. Effect of focusing conditions on synthesis of Titanium Oxide nanoparticles via laser ablation in Titanium-Water interface**, Arpita Nath**, Suvra Santa Laha and Alika Khare, Applied Surface Science , **257**, pp 3118-3122, (2011).
6. Synthesis of TiO_2 nanoparticles via laser ablation at Titanium-water interface, **Arpita Nath**, Suvra Santa Laha and Alika .Khare , Integrated Ferroelectrics, **118** , pp 1-7, (2010).

7. Studies on Laser Induced Breakdown in Water, **Arpita Nath** and Aika Khare , Journal of Physics : Conference Series, **2008**, pp 012090, (2010).
8. Measurement of charged particles and cavitation bubble expansion velocities in laser induced breakdown in water, **Arpita Nath** and Alika Khare**,** Laser and Particle Beams, **26**, pp 425-432, (2008).
9. Laser induced breakdown in liquid and solid-liquid interface, Alika Khare and **Arpita** Nath ,Kiran – A Bulletin of Indian Laser Association , **19** , pp 01-06 ,(2008).

- **Journal Papers (Under review/Communicated/Preparation)**

1. Size induced structural modifications in copper oxide nanoparticles synthesized via laser ablation in liquids, **Arpita Nath** and Alika Khare (Under Review).
2. Laser Induced High Pressure and High Temperature conditions at titanium-water interface and its implication on TiO_2 nanoparticles, **Arpita Nath** and Alika Khare (Under Review).
3. Transient evolution of charge carriers in laser induced plasma in liquids, **Arpita Nath** and Alika Khare (communicated).
4. Bacterial Inhibition by $Cu@Cu_2O$ nanocomposities, **Arpita Nath**, Archana Das, Latha Rangan and Alika Khare (Under preparation).
5. Photocatalytic activity of TiO_2 nanoparticles synthesized via laser ablation in liquids **Arpita Nath** and Alika Khare (Under preparation).

- **Conference Papers**

1. "Estimation of OH and O_2 Rotational Temperature during Laser Induced Breakdown at Titanium Water Interface", **Arpita Nath** and Alika Khare, MMISLIBS-10, Allahabad, December 2010
2. "Bacterial Inhibition by Cu/Cu_2O Nanocomposites Prepared via Laser Ablation in Liquids", **Arpita Nath**, Archana Das, Latha Rangan and Alika Khare, Photonics-10, IIT Guwahati, December 2010
3. "Antibacterial activity of copper oxide nanoparticles synthesized via laser ablation in liquids", **Arpita Nath**, Archana Das, Latha Rangan and Alika Khare, IISC-10, Jamia Millia Islamia , Delhi, December 2010
4. "Photocatalytic Activity of TiO_2 Nanocolloids Formed via Laser Ablation of Ti in Water", **Arpita Nath** and Alika Khare, "PEFM 2010 – Physics of Emerging Functional Materials", BARC Mumbai, September 2010.
5. "Synthesis of TiO_2 nanoparticles via laser ablation at Titanium-water interface", **Arpita Nath** and Alika Khare, "ICE-2009 – International conference on Electroceramics", University of Delhi, December 2009
6. "Synthesis of Metal Oxide Nanoparticles Using Laser Induced Breakdown at Solid-liquid Interface", **Arpita Nath** and Alika Khare, "MR 08 – Material Research Symposium", IIT Bombay, May 2008.
7. "Spectroscopic investigations on Laser Induced Breakdown in Water", **Arpita Nath** and Alika Khare, Plasma 2008 – National symposium in Plasma Physics, December 2008, BARC Mumbai.
8. "Sculpting of optical fibre tip for microlens formation", Prahlad Kumar Baruah, **Arpita Nath**, Alika Khare ,Rodney Bernard and Kamlesh Alti

Photonics 2008 – International conference on Fiber Optics and Photonics, December 2008, IIT Delhi.

9. "Band gap vaiation in CuO generated via pulsed laser ablation at solid-liquid interface ", **Arpita Nath** and Alika Khare , Photonics 2008 – International conference on Fiber Optics and Photonics, December 2008, IIT Delhi
10. Studies on Laser Induced Breakdown in Water" **Arpita Nath** and Alika Khare, "PLASMA 2007 – National Symposium on Plasma Physics", IPR Gandhinagar, December 2007.

- **Workshops Attended**

1. DST-SERC Preparatory School on Modern Optics, November 2010, IIT Guwahati
2. DST-SERC School on Plasma Diagnostics, July 2009, IPR Gandhinagar
3. Workshop on Coherent Control of Optical Phenomena" July 2007, Indian Institute of Technology Kanpur.